

---

Theses and Dissertations

---

Spring 2015

## Low velocity impact damage assessment in IM7/977-3 cross-ply composites using 3D computed tomography

Brandon Michael Demerath  
*University of Iowa*

Follow this and additional works at: <https://ir.uiowa.edu/etd>



Part of the [Mechanical Engineering Commons](#)

Copyright 2015 Brandon Michael Demerath

This thesis is available at Iowa Research Online: <https://ir.uiowa.edu/etd/1583>

---

### Recommended Citation

Demerath, Brandon Michael. "Low velocity impact damage assessment in IM7/977-3 cross-ply composites using 3D computed tomography." MS (Master of Science) thesis, University of Iowa, 2015.  
<https://doi.org/10.17077/etd.dnw9iiqs>

---

Follow this and additional works at: <https://ir.uiowa.edu/etd>



Part of the [Mechanical Engineering Commons](#)

LOW VELOCITY IMPACT DAMAGE ASSESSMENT IN IM7/977-3 CROSS-PLY  
COMPOSITES USING 3D COMPUTED TOMOGRAPHY

by

Brandon Michael Demerath

A thesis submitted in partial fulfillment  
of the requirements for the Master of  
Science degree in Mechanical Engineering  
in the Graduate College of  
The University of Iowa

May 2015

Thesis Supervisor: Associate Professor Olesya I. Zhupanska

Graduate College  
The University of Iowa  
Iowa City, Iowa

CERTIFICATE OF APPROVAL

---

MASTER'S THESIS

---

This is to certify that the Master's thesis of

Brandon Michael Demerath

has been approved by the Examining Committee  
for the thesis requirement for the Master of Science  
degree in Mechanical Engineering at the May 2015 graduation.

Thesis Committee: \_\_\_\_\_  
Olesya I. Zhupanska, Thesis Supervisor

\_\_\_\_\_  
Albert Ratner

\_\_\_\_\_  
Hiroyuki Sugiyama

To My Family

## ACKNOWLEDGMENTS

I would like to express my appreciation to Professor Oleysa I. Zhupanska for her support and guidance throughout the research process and my education at the University of Iowa. The skills I have developed will continue to benefit me throughout my career in engineering. I would also like to thank Professors Albert Ratner and Hiroyuki Sugiyama for serving on my thesis defense committee. In addition, I would like to express my gratitude towards Bryne Berry, Robert Hart, and Yeqing Wang for their assistance with laboratory experimentation and methods. Further, I would particularly like to express my gratitude towards Dan Hollinger, CT Analyst for Schneider Electric, for his assistance and expertise with CT imaging. I would also like to express my appreciation for all sources of funding for my research, and specifically like to acknowledge that this work was partially supported by NASA EPSCoR Grant S5937M: “Sensing and Imaging of Impact Damage in Composites.” Finally, I would like to thank my family for their support throughout my college education.

## ABSTRACT

Low-velocity impact damage in IM7/977-3 carbon fiber reinforced polymer (CFRP) composites was investigated using 3D computed tomography (CT). 32-ply IM7/977-3 symmetric cross-ply composites were impacted at different impact energy levels and with different impactors (DELTRIN® resin flat-ended cylindrical and tool steel hemispherical strikers) using an Instron 8200 Dynatup drop-weight impact machine. The impact energies were chosen to produce slightly visible damage, characterized by short cracks on the impacted surface and little delamination on the non-impacted surface (29.27 J), and barely visible damage, characterized by indentation on the impacted surface but no visible delamination on the back surface of the specimens (20.77 J). Internal damage was assessed using the Zeiss METROTOM 1500 industrial CT scanning system, and CT images were reconstructed using VGStudio MAX and the MyVGL 2.2 viewer. To determine the extent of the damage zone, impacted 152.4 mm square composite plates were initially scanned. As the relatively large specimen size did not allow for evaluation of internal cracks and isolation of delamination at ply interfaces, smaller specimens that enclosed the damaged region (45 mm square plates) were cut out and imaged. The CT scan results showed that volume of the impact damage zone had a generally positive correlation with impact energy, maximum load, and maximum deflection, but that the relationship was generally weak. Absence of a definite correlation between damage volume and impact energy was unexpected, as the difference in the impact energy was up to 30%.

## PUBLIC ABSTRACT

As composite materials become more common in sporting goods, automotive applications, and aerospace structures, reliable methods of damage assessment will become increasingly important. Composite structures, unlike metals, tend to develop internal damage and fail in different ways. In the present work low-velocity impact damage, like that which could be produced from a dropped tool, was investigated for aerospace-grade carbon fiber reinforced polymer composite plates. Each plate was composed of 32 alternating-direction layers (plies) and was symmetric about the center plies. Each plate was impacted using a drop-weight test machine, and the impact force, deflection, and energy were measured. Two impact energies were investigated: One that produced slightly visible damage (in the form of cracks and back surface damage) and one that produced barely visible damage (in the form of a small front surface indent). To determine the extent of the internal damage the plates were scanned using an industrial CT imaging system, which produced a 3D x-ray image. As the scan of the original specimens (152.4 mm square plates) had too low of a resolution to uniquely identify all internal damage features, the plates were cut to a smaller size (45 mm square plates) and scanned again. The images produced from the smaller plates had a resolution approximately 2.5 times smaller than the thickness of the individual plies, which allowed for a more accurate internal damage assessment. Results showed that the amount of internal damage increased as the impact energy increased, but that the relationship was generally weak.

## TABLE OF CONTENTS

LIST OF TABLES .....	viii
LIST OF FIGURES .....	ix
CHAPTER 1 INTRODUCTION .....	1
1.1 Background Information .....	1
1.2 Literature Review .....	7
1.2.1 Review of Impact on Laminated Composites .....	7
1.2.2 Review of Damage Evaluation Techniques .....	11
1.3 Thesis Objectives .....	14
CHAPTER 2 EXPERIMENTAL SET-UP AND EXPERIMENTAL PROCEDURES...	16
2.1 Experimental Considerations .....	16
2.2 Experimental Setup .....	17
2.2.1 Low Velocity Impact Setup.....	17
2.2.2 Computed Tomography Imaging Setup .....	19
2.3 Summary of Experimental Setup .....	21
CHAPTER 3 LOW VELOCITY IMPACT EXPERIMENTAL RESULTS .....	22
3.1 Material Characterization .....	22
3.2 Impact Characterization .....	23
3.2.1 Preliminary Impact Testing .....	23
3.2.2 “Low” Energy (20.77 J) Impact .....	27
3.2.3 “Intermediate” Energy (29.27 J) Impact .....	36
3.2.4 “Intermediate” Energy (29.25 J) DELRIN Impact.....	45
3.2.5 Impact Characterization Results.....	53
3.3 Comparison to Previous Work .....	55
3.4 Theoretical Contact Analysis .....	61
3.5 Summary of Low Velocity Impact Experimental Results .....	66
CHAPTER 4 COMPUTED TOMOGRAPHY IMAGE PROCESSING.....	68
4.1 Image Processing Methodology .....	68
4.2 Specimen Cut Sizing .....	73
4.3 CT Image Processing Results.....	75
4.3.1 Specimen 3 .....	75
4.3.2 Specimen 4 .....	87
4.3.3 Specimen 5 .....	92

4.3.4 Specimen 6 .....	101
4.3.5 Specimen 7 .....	109
4.3.6 Specimen 8 .....	120
4.3.7 Specimens 9, 10, and 11 .....	125
4.4 Analysis of Image Processing Results .....	128
4.4.1 Overall Results .....	128
4.4.2 Comparison to Visual Inspection .....	139
4.4.3 Delamination from Specimen Cutting .....	140
4.5 Comparison to Previous Work .....	143
4.6 Summary of Image Processing .....	152
<b>CHAPTER 5 SUMMARY AND RECOMMENDATIONS .....</b>	<b>155</b>
5.1 Summary .....	155
5.2 Recommendations .....	156
<b>APPENDIX IMAGE PROCESSING MATLAB CODE .....</b>	<b>159</b>
A.1 Multi-Image Segmentation Code .....	160
A.2 Single-Image Segmentation Code .....	162
<b>REFERENCES .....</b>	<b>165</b>

## LIST OF TABLES

Table 3.1: Summary of Materials Tested.....	23
Table 3.2: Impact Characterization Data for 32-ply Symmetric Cross-Ply Specimens .....	54
Table 3.3: Impact Characterization Data for 16-ply Cross-Ply Specimens (Hart 2011) .....	57
Table 3.4: Comparison to Previous Impact Conditions and Results .....	59
Table 3.5: Material Properties for Contact Analysis .....	63
Table 4.1: Full Specimen Damage Measurements .....	129
Table 4.2: Specimen Impact and Imaging Results.....	130
Table 4.3: Cut Specimen Damage Measurements .....	133
Table 4.4: Visual Damage and Internal Damage Measurements.....	140
Table 4.5: Cutting-Induced Damage Measurement Results .....	142
Table 4.6: CT Imaging Results of Song's Specimen .....	151

## LIST OF FIGURES

Figure 1.1: Materials Used in Construction of the Boeing 787 Dreamliner Airplane (Boeing 2014) .....	2
Figure 1.2: Types of Composite Reinforcement (Sierakowski and Newaz 1995) .....	3
Figure 1.3: Expanded Example of a Laminated Composite (Jones 1999).....	5
Figure 1.4: Cracking Pattern in Thick Laminates (a) and Thin Laminates (b) (Abrate 1998) .....	9
Figure 1.5: Delamination in a Laminated Composite (Abrate 1998) .....	10
Figure 2.1: Impact Testing Fixture .....	18
Figure 2.2: Metallic Tup Insert .....	19
Figure 2.3: Zeiss METROTOM 1500 Industrial CT System (Zeiss 2015) .....	21
Figure 3.1: Impact Damage on the Top Surface of Specimen 1 .....	24
Figure 3.2: Impact Damage on the Bottom Surface of Specimen 1 .....	25
Figure 3.3: Side View of Impact Damage on the Bottom Surface of Specimen 1 .....	25
Figure 3.4: Impact Damage on the Top Surface of Specimen 2 .....	26
Figure 3.5: Impact Damage on the Bottom Surface of Specimen 2 .....	27
Figure 3.6: Side View of Impact Damage on the Bottom Surface of Specimen 2 .....	27
Figure 3.7: Impact Damage on the Top Surface of Specimen 3 .....	29
Figure 3.8: Impact Damage on the Bottom Surface of Specimen 3 .....	29
Figure 3.9: Impact Damage on the Top Surface of Specimen 4 .....	30
Figure 3.10: Impact Damage on the Bottom Surface of Specimen 4 .....	30
Figure 3.11: Impact Damage on the Top Surface of Specimen 5 .....	31
Figure 3.12: Impact Damage on the Bottom Surface of Specimen 5 .....	31
Figure 3.13: Force versus Time for Impact Characterization of Specimens 1 – 5 .....	32

Figure 3.14: Force versus Deflection for Impact Characterization of Specimens 1 – 5.....	33
Figure 3.15: Force versus Time for Impact Characterization of Specimen 3, 4, & 5.....	34
Figure 3.16: Force versus Deflection for Impact Characterization of Specimens 3, 4, & 5.....	35
Figure 3.17: Impact Damage on the Top Surface of Specimen 6.....	37
Figure 3.18: Impact Damage on the Bottom Surface of Specimen 6.....	37
Figure 3.19: Side View of Impact Damage on the Bottom Surface of Specimen 6.....	38
Figure 3.20: Impact Damage on the Top Surface of Specimen 7.....	38
Figure 3.21: Impact Damage on the Bottom Surface of Specimen 7.....	39
Figure 3.22: Side View of Impact Damage on the Bottom Surface of Specimen 7.....	39
Figure 3.23: Impact Damage on the Top Surface of Specimen 8.....	40
Figure 3.24: Impact Damage on the Bottom Surface of Specimen 8.....	40
Figure 3.25: Side View of Impact Damage on the Bottom Surface of Specimen 8.....	41
Figure 3.26: Force versus Time for Impact Characterization of Specimens 6, 7, & 8....	41
Figure 3.27: Force versus Deflection for Impact Characterization of Specimens 6, 7, & 8.....	42
Figure 3.28: Force versus Time for Impact Characterization of Specimens 3 – 8.....	43
Figure 3.29: Force versus Deflection for Impact Characterization of Specimens 3 – 8.....	44
Figure 3.30: Impact Damage on the Top Surface of Specimen 9.....	46
Figure 3.31: Impact Damage on the Bottom Surface of Specimen 9.....	46
Figure 3.32: Impact Damage on the Top Surface of Specimen 10.....	47
Figure 3.33: Impact Damage on the Bottom Surface of Specimen 10.....	47
Figure 3.34: Impact Damage on the Top Surface of Specimen 11.....	48
Figure 3.35: Impact Damage on the Bottom Surface of Specimen 11.....	48

Figure 3.36: Force versus Time for Impact Characterization of Specimens 9, 10, & 11 ....	49
Figure 3.37: Force versus Deflection for Impact Characterization of Specimens 9, 10, & 11.....	50
Figure 3.38: Force versus Time for Impact Characterization of Specimens 6 – 11 .....	51
Figure 3.39: Force versus Deflection for Impact Characterization of Specimens 6 – 11.....	52
Figure 3.40: Visible Damage on the Back Side of Sample 48 (Hart 2011).....	57
Figure 3.41: Tool Steel (left) and DELRIN® (right) Tup Insert (Zantout 2009) .....	58
Figure 3.42: Test Fixture 3D Model (left) and Fabricated Assembly (right) (Zantout 2009) .....	58
Figure 3.43: Contact Stress for Rigid Steel Hemisphere on 977-3 Half-Space.....	65
Figure 3.44: Contact Stress for Flat-Ended DELRIN® Cylinder on 977-3 Half-Space .....	66
Figure 4.1: Example Gray-Values Setting for Isolating Damage in MyVGL .....	69
Figure 4.2: Example of Gradient Line in Image 7 (Depth of 1.08 mm) of Specimen 3.....	72
Figure 4.3: Cut Specimen 3 within Original Plate.....	74
Figure 4.4: Corner Delamination in Side View of Cut Specimen 3 .....	75
Figure 4.5: Length of Largest Internal Damage for Specimen 3 (Depth of 2.58 mm) ....	76
Figure 4.6: Segment with Largest Damaged Area for Specimen 3 (Depth of 2.48 mm) ....	77
Figure 4.7: Segment with Largest Damaged Area for Cut Specimen 3 (Depth of 1.80 mm, Within Ply 16).....	79
Figure 4.8: Maximum Damage Length in the 0° Direction for Specimen 3 .....	80
Figure 4.9: Maximum Damage Length in the 90° Direction for Specimen 3 .....	81
Figure 4.10: Cracks on Impacted Surface for Cut Specimen 3.....	82
Figure 4.11: Annotated Max Damage Length in the 0° Direction for Specimen 3 .....	83

Figure 4.12: Annotated Max Damage Length in the 90° Direction for Specimen 3 .....	83
Figure 4.13: Ply Interfaces from Specimen 3 .....	85
Figure 4.14: Length of Largest Internal Damage for Specimen 4 (Depth of 2.67 mm) .....	88
Figure 4.15: Segment with Largest Damaged Area for Specimen 4 (Depth of 2.40 mm) .....	89
Figure 4.16: Segment with Largest Damaged Area for Cut Specimen 4 (Depth of 2.29 mm) .....	91
Figure 4.17: Length of Largest Internal Damage for Specimen 5 (Depth of 2.49 mm) ..	93
Figure 4.18: Segment with Largest Damaged Area for Specimen 5 (Depth of 2.32 mm) .....	94
Figure 4.19: Segment with Largest Damaged Area for Cut Specimen 5 (Depth of 3.02 mm, Between Plies 24 and 25) .....	96
Figure 4.20: Maximum Damage Length in the 0° Direction for Specimen 5 .....	98
Figure 4.21: Maximum Damage Length in the 90° Direction for Specimen 5 .....	98
Figure 4.22: Ply Interfaces from Specimen 5 .....	100
Figure 4.23: Length of Largest Internal Damage for Specimen 6 (Depth of 2.17 mm) .....	102
Figure 4.24: Segment with Largest Damaged Area for Specimen 6 (Depth of 2.17 mm) .....	103
Figure 4.25: Segment with Largest Damaged Area for Cut Specimen 6 (Depth of 1.76 mm, Between Plies 14 and 15) .....	105
Figure 4.26: Maximum Damage Length in the 0° Direction for Specimen 6 .....	106
Figure 4.27: Maximum Damage Length in the 90° Direction for Specimen 6 .....	107
Figure 4.28: Ply Interfaces from Specimen 6 .....	108
Figure 4.29: Length of Largest Internal Damage for Specimen 7 (Depth of 2.17 mm) .....	111
Figure 4.30: Segment with Largest Damaged Area for Specimen 7 (Depth of 2.17 mm) .....	112

Figure 4.31: Segment with Largest Damaged Area for Cut Specimen 7 (Depth of 3.01 mm, Between Plies 23 and 24) .....	114
Figure 4.32: Maximum Damage Length in the 0° Direction for Specimen 7 .....	116
Figure 4.33: Maximum Damage Length in the 90° Direction for Specimen 7 .....	116
Figure 4.34: Ply Interfaces from Specimen 7 .....	118
Figure 4.35: Length of Largest Internal Damage for Specimen 8 (Depth of 2.32 mm) .....	121
Figure 4.36: Segment with Largest Damaged Area for Specimen 8 (Depth of 2.55 mm) .....	122
Figure 4.37: Segment with Largest Damaged Area for Cut Specimen 8 (Depth of 3.57 mm) .....	124
Figure 4.38: Internal Segment from Specimen 9 (Depth of 4.17 mm) .....	126
Figure 4.39: Internal Segment from Cut Specimen 9 .....	128
Figure 4.40: Damaged Volume versus Impact Energy for All Specimens .....	131
Figure 4.41: Damaged Volume versus Maximum Impact Force for All Specimens .....	131
Figure 4.42: Damaged Volume versus Maximum Displacement for All Specimens .....	132
Figure 4.43: Damaged Volume versus Impact Energy for Cut Specimens .....	134
Figure 4.44: Damaged Volume versus Maximum Impact Force for Cut Specimens .....	135
Figure 4.45: Damaged Volume versus Maximum Displacement for Cut Specimens .....	135
Figure 4.46: Damaged Volume versus Impact Energy for Both Sets of Specimens .....	136
Figure 4.47: Damaged Volume versus Maximum Impact Force for Both Sets of Specimens .....	137
Figure 4.48: Damaged Volume versus Maximum Displacement for Both Sets of Specimens .....	138
Figure 4.49: Side View of Corner Delamination for Cut Specimen 3 .....	141
Figure 4.50: Front (Left) and Back (Right) Damage to Specimen 2-1, Impacted at 16 J (Song 2014) .....	144

Figure 4.51: Front (Left) and Back (Right) Damage to Specimen 1-6, Impacted at 22.5 J (Song 2014).....	145
Figure 4.52: Front (Left) and Back (Right) Damage to Specimen 2-4, Impacted at 26 J (Song 2014).....	145
Figure 4.53: Length of Largest Internal Damage Measured by Song for Specimen 1-6 (Depth of 2.22 mm) (Song 2014).....	147
Figure 4.54: Length of Largest Internal Damage for Specimen 1-6 (Depth of 2.64 mm) .....	148
Figure 4.55: Side View of the Center of Cut Specimen 3 .....	153

## CHAPTER 1

### INTRODUCTION

#### 1.1 Background Information

In recent decades, composite materials have become much more prevalent in many different areas. As manufacturing costs have decreased, composite materials have seen greater use in aerospace, automotive, and high-end sporting equipment applications. For example, the Boeing 787 Dreamliner airplane, shown in Figure 1.1, is comprised of 50 % composite materials, which is an increased use from the Boeing 777 (Boeing 2014). Boeing chose to make increased use of composite materials as they can be made lighter than aluminum components without decreasing the load-bearing capacity. While this does increase the cost of components, the fuel savings that accompany decreased weight made composites a cost-competitive material choice. As these materials become more widespread, it is particularly important that engineers understand the physical properties and behaviors of advanced composite materials.

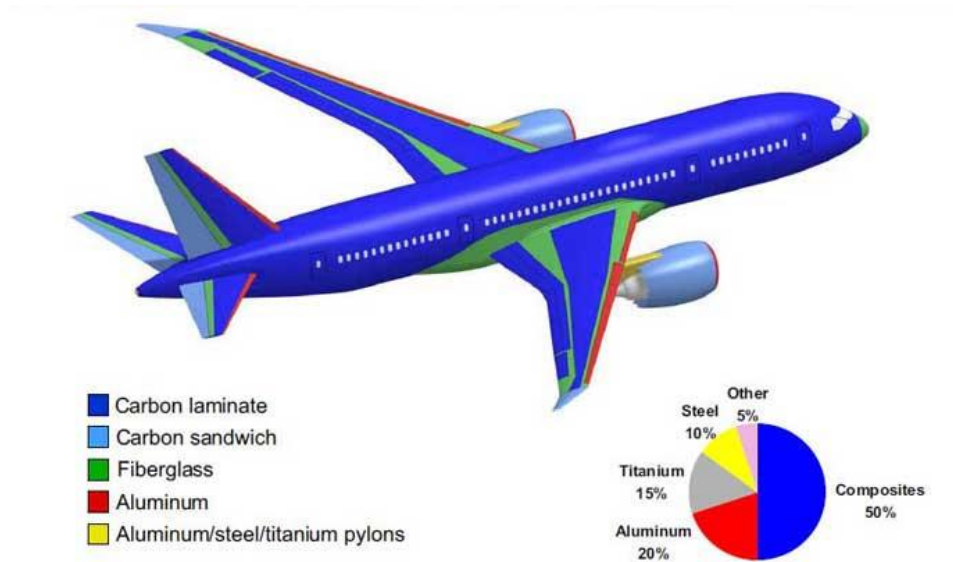


Figure 1.1: Materials Used in Construction of the Boeing 787 Dreamliner Airplane (Boeing 2014)

Composite materials are created by combining two or more constituent materials on a macroscopic level. A composite material can be designed and manufactured to improve specific properties over the base materials (Jones 1999). This includes properties such as strength, stiffness, corrosion resistance, fatigue life, and weight. Because their properties can be tailored to specific applications and the weight savings composite materials have over traditional materials (such as metals), composites can be desirable as modern structural materials.

Common types of composite reinforcement include fibrous, laminated, and particulate composites, or combinations of the three (Jones 1999). The role of the reinforcement is to bear the majority of the load. Fiber reinforcement is often used, and

may be implemented as long continuous fibers or short chopped fibers. Continuous fibers can also be woven into fabrics or textile geometries, which can have more advantageous stiffness and damage tolerance properties over simple aligned fibers. Other types of reinforcements include particulate and flake reinforcement, and they are often used for specialized applications (Sierakowski and Newaz 1995). Examples of different types of reinforcement can be seen in Figure 1.2.

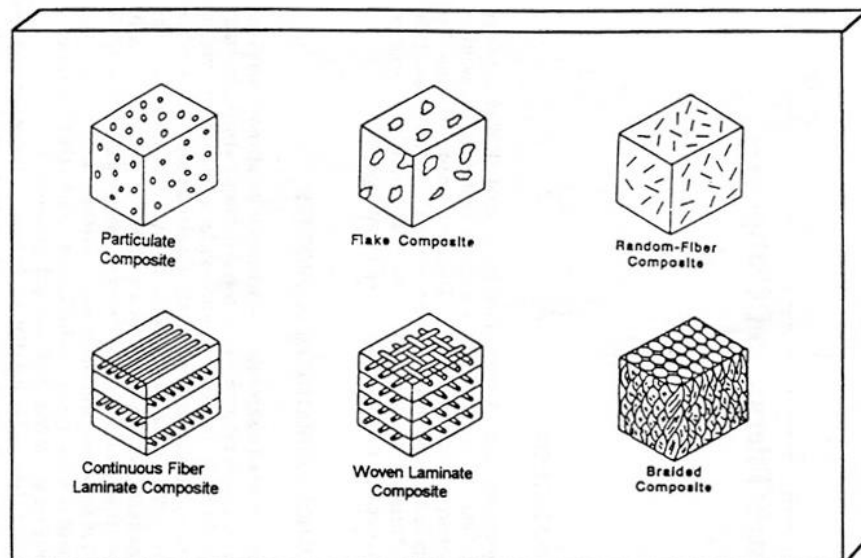


Figure 1.2: Types of Composite Reinforcement (Sierakowski and Newaz 1995)

Composite matrices are often composed of polymers/epoxies, and they can also be made from metals or ceramics. The main role of the matrix is to transfer load to and maintain the structure of the reinforcement material. The matrix material is chosen to give the desired structural characteristics and should be compatible with the reinforcement material.

Individual layers of unidirectional fibers or woven sheets, called lamina, can be combined into laminated composites. An expanded view of an angle-ply laminated composite is shown in Figure 1.3. Laminated composites can have improved in-plane properties compared to unidirectional composites, since the load-bearing fibers run in multiple directions.

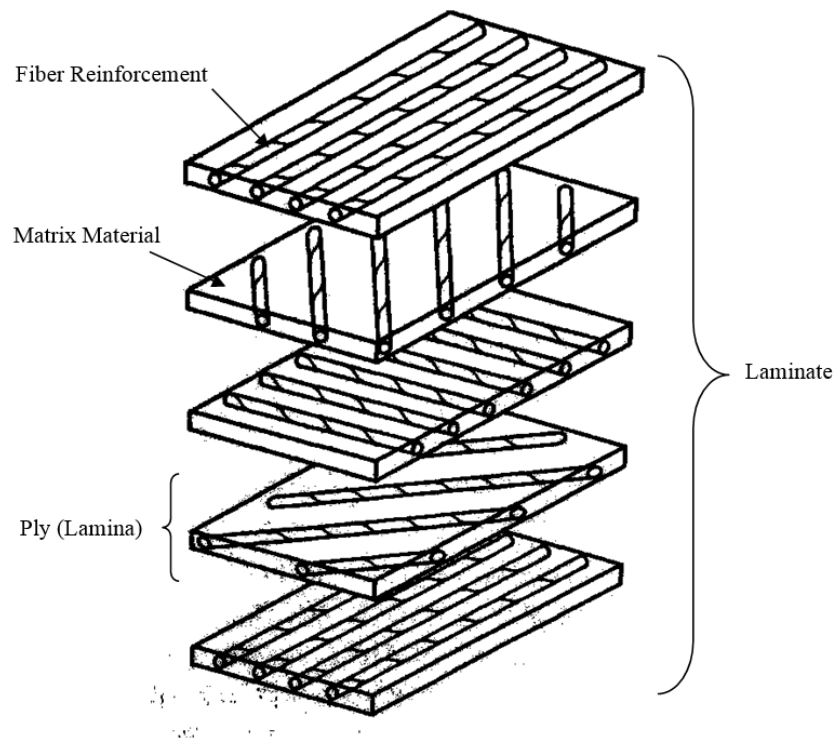


Figure 1.3: Expanded Example of a Laminated Composite (Jones 1999)

While composites have advantages over traditional structural materials, they do have some distinct drawbacks. Foremost amongst these is damage tolerance. In a metal structure, a low-velocity impact might leave a visible indent on the surface. This deformation would be a visible indication of damage and, depending on the structure, loads, and severity, would not likely lead to catastrophic failure as metals tend to be ductile. Further, the stresses, strains, and failure modes for metals and other traditional structural materials are fairly well understood. Composite materials, on the other hand, tend to be less resistant to damage and have much more complicated failure modes

(Sierakowski and Newaz 1995). An impact on a composite structure might leave no visible surface damage, but damage could develop on the rear face or even internally. Because of this, while a visual inspection of a metal structure may be sufficient to identify damage and determine safe use, the same procedure might not be adequate for a composite structure. A visual inspection could underreport the amount of damage present which may result in the use of an unsafe composite structure.

Since damage to a composite structure decreases its strength and stiffness, an accurate assessment of damage is necessary to determine if the structure is capable of bearing the operational loads. A simple visual inspection will not suffice, and so more advanced detection methods must be implemented. Traditionally, internal damage to laminated composite structures is measured using destructive techniques. While these methods do provide accurate measurements of internal damage, they are not useful for functional components; it would not be practical to cut apart an airplane wing just to check for damage. This has motivated research and development of non-destructive imaging techniques, as discussed in a later section.

In the present work, the behavior of carbon fiber reinforced polymer matrix composites subject to low-velocity impact and non-destructive damage assessment techniques are considered. The literature review in the following section focuses on studies analyzing both low-velocity impact damage and the state of the art for non-destructive damage evaluation of laminated composites.

## 1.2 Literature Review

### 1.2.1 Review of Impact on Laminated Composites

Throughout the life of a laminated composite component, particularly in aviation and aerospace applications, impact damage is unavoidable. Impact on composite structures can come from maintenance workers dropping tools, bird strikes during operation, and flying debris during takeoff and landing. Regardless of the cause, these low-velocity impacts can produce extensive damage to the composite structure. What makes low-velocity impact damage especially dangerous in composite structures is that, unlike in their metal counterparts, composite materials tend to develop damage internally or on back faces. This is particularly true for fiber-reinforced laminated composites, and the corresponding degradation of material properties must be taken into account in the design of composite structures (Abrate 1998, Sierakowski and Newaz 1995). Therefore, impact damage of laminated composites has been the subject of a large number of studies.

While research into impact damage of composites has been generally extensive, most investigations can be classified as considering either high-velocity or low-velocity impact events. High-velocity impact studies consider failure mechanisms relating to wave propagation and global effects, while low-velocity impact studies focus on localized stresses and deflections near the impact site. As low-velocity impact is concerned with local effects, it has been shown that classical plate theories and Hertzian contact analysis can provide meaningful, if non-comprehensive, insight into low-velocity impact events (Abrate 1998). To develop a more complete understanding of impact on

composites than is provided by simple analytic models, a great number of experimental investigations have been conducted.

When assessing low-velocity impact damage of laminated composites, several failure mechanisms must be considered. For low-velocity impacts that do not penetrate the composite, damage develops as matrix cracking, delamination between plies, and fiber failure (Sierakowski and Newaz 1995). Damage initiation primarily takes the form of matrix cracking. For thin laminates, matrix cracking develops towards the back, non-impacted face as a result of high bending stresses. For thick laminates, high localized contact stresses can cause matrix cracks to develop near the impacted surface.

Throughout an impact event the matrix cracks propagate away from the initiation point, resulting in a conical “pine tree” shape emanating from the impacted surface (thick laminates) or the back surface (thin laminates) (Tan, Watanabe, and Iwahori 2011, Abrate 1998). This cracking behavior can be seen in Figure 1.4. Matrix cracks can lead to a decrease in stiffness and significantly contribute to ply delamination.

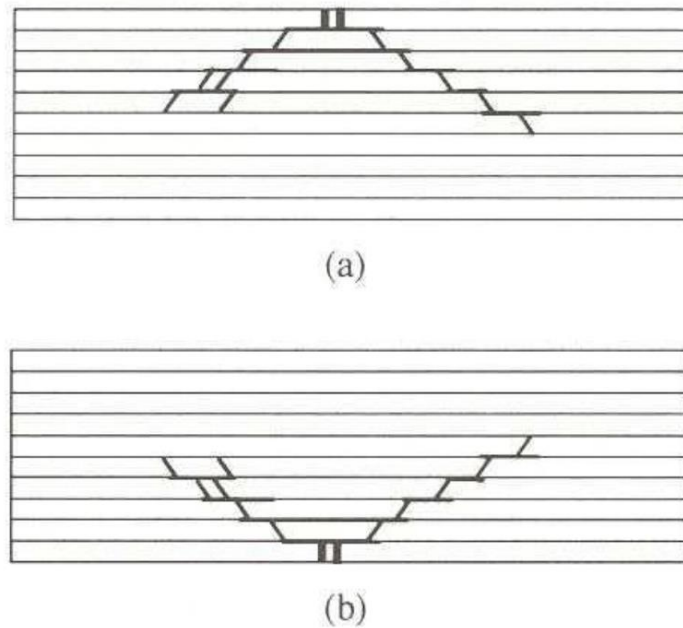


Figure 1.4: Cracking Pattern in Thick Laminates (a) and Thin Laminates (b) (Abrate 1998)

Delamination, which is the separation of two adjacent layers, or plies, occurs when matrix cracks propagate along ply interfaces of different orientations.

Delamination can significantly reduce composite structure stiffness, but it can be arrested by cross-stitching through the layers of a laminate (Pearson et al. 2007). In composite laminates with unidirectional plies, the delaminated area tends to be oblong, or “peanut” shaped, and oriented in the direction of the lower ply (Abrate 1998). An example of delamination orientation is shown in Figure 1.5.

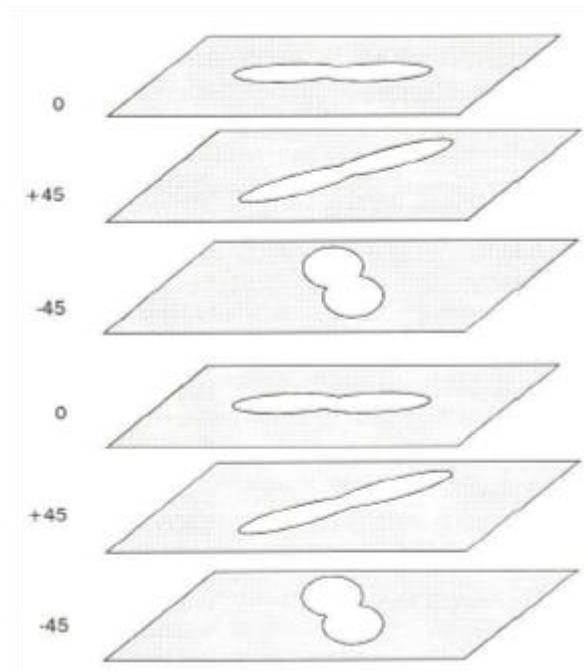


Figure 1.5: Delamination in a Laminated Composite (Abrate 1998)

While matrix cracking and ply delamination contribute to a decrease in residual properties after impact, structural failure of a laminated composite is usually preceded by fiber breakage. As the matrix and ply interfaces degrade, load is transferred to the fiber reinforcement. For normal impact on a plate, the concentrated transverse load on the fibers can cause them to break or separate, leading to penetration and then perforation of the composite. Even when penetration does not occur, internal fiber breakage greatly reduces the residual tensile and compressive strength of the composite structure (Malhotra and Guild 2014).

### 1.2.2 Review of Damage Evaluation Techniques

While the processes involved in impact damage of laminated composite plates are fairly well understood, evaluation of impact damage poses some challenges. Traditional damage evaluation techniques are often destructive, requiring physical access to damaged regions. Optical microscopy, a technique where specimen are cut along a region of interest, treated with contrast, polished, and viewed under high-powered microscopes, necessarily requires access to a free edge located transversely through the zone of interest (Daggumati et al. 2010). Similarly, conventional x-ray techniques require treating damaged areas with an x-ray absorbent to heighten contrast. While contrast treatments allow for small-scale damage to be detected, application of contrast agents often requires open access to the damaged cross-section. Other conventional x-ray techniques, like de-ply radiography, also require physical deconstruction of the laminate to achieve meaningful damage detection (Gao and Kim 1998). While these techniques can provide critical information on damage mechanisms and development in laminated composites, the desire for non-destructive damage evaluation techniques has led to increased research in this area.

For composite damage evaluation in aerospace and industry applications destructive damage assessment is not practical, and this has driven investigations into non-destructive evaluation methods. One of these techniques is ultrasonic scanning. In essence, ultrasonic sensing uses high frequency sound waves to penetrate a composite specimen, and the reverberation of the waves provides insight into the internal structure of the specimen (Gao and Kim 1998, Tan and Watanabe 2012). This technique has been successfully used to detect delamination and large matrix cracks, but it does have limited

resolution and penetration abilities. Specifically, traditional ultrasonic C-scans are unable to resolve layered damage through the thickness of the specimen, which prevents this technique from differentiating delamination zones between different plies (Tan and Watanabe 2012). While enhanced ultrasonic methods such as the acoustic backscatter and scanning acoustic microscopy techniques can provide detailed 3D representations of internal damage, they do not have widespread use in industry (Gao and Kim 1998).

Another non-destructive damage assessment technique is deflectometry. This is an optical strain measuring technique, where the visual deflection of the specimen surface subject to an applied load can provide data about the internal damage regions. While this indirect detection method is capable of sensing and locating cracked regions and impact zones, it does require significant processing, is currently limited to flat panels, and has issues realizing large areas of delamination (Devivier, Pierron, and Wisnom 2013). Beyond these non-destructive techniques, for high-resolution direct measurements of internal damage x-ray computed tomography has been used.

X-ray computed tomography (CT) is a direct imaging technique similar to x-ray radiography in that it differentiates internal structures based on differences in density and x-ray absorption. Unlike standard radiography, however, CT imaging does not require a contrast agent and is capable of producing three-dimensional scans of parts (Desplentere et al. 2005). Computed tomography achieves this by rotating a sample by small angle increments while taking an x-ray image at each step. The images are then reconstructed using CT imaging software, and the complete scan can then be viewed as a 3D model or as orthogonal stacks of 2D images. Depending on the CT scanning equipment and the size of the specimen, image resolution can be as low as ultrasonic scans (generally

millimeter scale) or high enough to capture individual reinforcement fibers (generally micrometer scale) (Gao and Kim 1998). High resolution CT imaging allows for individual matrix cracks and ply delamination to be identified without introducing additional damage when preparing specimens for evaluation.

CT imaging can provide a detailed view of internal damage, but it does have some drawbacks. Particularly, CT scanning is not well suited for in-situ imaging. Some laboratory equipment has been developed for CT imaging of specimen in functional systems while undergoing loading, but geometry restrictions still limit the effectiveness of such a setup (Hufenbach et al. 2012). More often, specimens must be removed from functional setups to allow for 360° access for imaging. Further, for high-resolution imaging specimen must be small in size, often on the order of tens of millimeters. While selecting or cutting specimens to the appropriate size is possible in research scenarios, cutting functional composite structures “in the field” is less practical (Bull et al. 2013). CT scanning can also take a significant amount of time depending on the number of rotational steps captured, and reconstruction and analysis capabilities can depend on the technicians, software, and algorithms available. Despite these challenges, CT imaging is a non-destructive technique that is well suited to provide detailed information on internal damage in laminated composites.

The present work was motivated by the work of Song (2014). This work suggested that high resolution CT imaging could be achieved using medical-grade CT scanning equipment, and that industrial-grade CT scanning equipment was sufficient for preliminary damage assessment in layered textile-reinforced composite plates. Detailed images of the impact zone were developed, but it was noted that the image processing

procedure could use improvement. Specifically, since two different CT imaging systems were used to capture the high and low resolution images, the imaging parameters and software were significantly different. The scans produced using the industrial CT imaging system were able to be processed using a user-friendly software suite that provided quantitative information on the internal damage, but the resolution was not high enough to capture each ply individually. For both high and low resolution scans consistent imaging proved to be difficult, with samples arbitrarily rotated or offset at a small angle to the plane of the scan. Overall, Song's work showed the utility of both industrial- and medical-grade CT scanning systems for use with textile composites and provided a basis for the imaging techniques used in the present study.

The present work was also partially motivated by the work of Hart (2011). This work investigated coordinated impact and electrification of laminated carbon fiber composites. Specimens were subjected to a high-current electric pulse that was coordinated to occur at the same time as an impact event. The effect of current on impact resistance was investigated, and it was determined that as current increased the absorbed energy during the impact increased. While impact force and energy were measured, internal damage was not examined through use of imaging techniques. Hart's work provided the basis for material characterization and impact conditions used in the present study.

### 1.3 Thesis Objectives

There were two objectives of this thesis. The first objective was to determine the parameters for and measure the response of laminated composite plates during a low-

velocity impact event. The impact parameters, including impact height, impact mass, fixture, impact geometry, and impact material, were chosen so as to conform to the laboratory standards and to produce results that could be compared to previous work from this laboratory. Specifically, the impact energy was selected so as to produce little visible damage in 32-ply cross-ply carbon fiber reinforced polymer matrix composite specimens using a hemispherical steel impactor.

The final objective was to determine the capabilities of industrial computed tomography (CT) scanning equipment for damage assessment of laminated carbon fiber reinforced polymer matrix composites. In particular, the imaging capabilities were assessed for standard-sized specimens (152.4 mm square plates) and plates that had been cut to isolate the damaged region. Image resolution and processing methodology were of key interest throughout this investigation.

## CHAPTER 2

### EXPERIMENTAL SET-UP AND EXPERIMENTAL PROCEDURES

#### 2.1 Experimental Considerations

This work builds on the accomplishments of Hart (2011), who investigated low-velocity impact of carbon fiber reinforced polymer composites. The low-velocity impact experimentation method used in this investigation utilized the previous work of Hart, which built on the impact setup developed by Zantout (2009) and Deierling (2010). The previous experimental setup was developed for use with electrified carbon fiber composite plates, which included a non-conductive holding fixture, non-conductive tup insert, and a timed pneumatic trigger for the drop-weight impact machine. To ensure that the results of the current investigation would be comparable to standard impact tests, the custom holding fixture and tup insert were removed and replaced with standard equipment obtained directly from Instron. To ensure safe impact testing procedures, the pneumatic trigger was still used for the current investigation.

This work also builds on the accomplishments of Song (2014), who investigated computed tomography (CT) imaging of woven fabric carbon fiber reinforced polymer plates. The industrial CT scanning equipment used in the current investigation was the same as that used by Song for full-scale specimen imaging. The grey-value thresholding procedure developed by Song for isolating damaged regions was adapted for use in this investigation. Because of changes in software, the damaged area measurement procedure

used by Song could not be replicated and therefore required new development, as discussed in a later section.

## 2.2 Experimental Setup

### 2.2.1 Low Velocity Impact Setup

All impact tests were performed with the Instron 8200 Dynatup impact test machine. The Instron 8200 has an overall height of 2.305 m, width of 0.406 m, and depth of 0.457 m. It can be adjusted to a maximum drop height of 1.0 m, achieve a maximum velocity of 4.4 m/s, and the standard cross-head can carry 3.0 to 13.6 kg of mass. Together, this allows the impact test machine to produce impact energies ranging from 1.356 J to 132.8 J (Instron Corporation 2004). The Instron 8200 used was also equipped with a pneumatic rebound break. The rebound break, triggered by the velocity photogate, was designed to support the cross-head carriage after the impact occurs, decreasing the likelihood of multiple impacts.

For the impact testing considered in this report, the unmodified specimen fixture was used. The fixture (Instron # 7800-056) conformed to the standard for NASA-ST1, with a 5-inch (127 mm) square opening on both the top and bottom plate. This size opening allowed for approximately ½-inch (12.7 mm) clamping around the perimeter of a 6-inch (152.4 mm) specimen. The fixture consisted of a steel bottom base frame and a steel top plate. The bottom base contained alignment pegs that fit into corresponding holes on the top plate, ensuring the alignment of the fixture openings. Specimens were centered within the fixture opening, and alignment of a center mark on each specimen was also checked against the tup insert to verify specimen placement. The four fixture

clamps seen in Figure 2.1 were used to secure the specimen between the fixture plates. All clamps were tightened by hand to the minimum torque to avoid creating additional stresses within the clamped specimen.

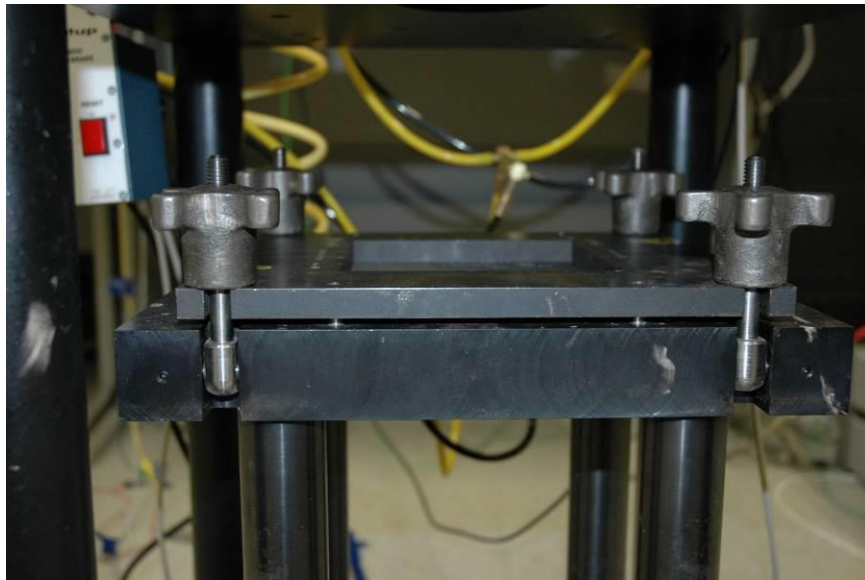


Figure 2.1: Impact Testing Fixture

A standard metallic tup insert (model 8746, Instron # 7910-21 3) was used for the initial impact tests. The tup insert, seen in Figure 2.2, had a 5/8-inch (15.88 mm) diameter hemispherical tip and was fabricated from tool steel. This tup insert was selected as it was believed that the 32-ply specimens would require significant impact

energy to damage, and previous work by Hart (2011) indicated that a machined polymer tup insert would not be strong enough to withstand the impact.



Figure 2.2: Metallic Tup Insert

### 2.2.2 Computed Tomography Imaging Setup

As discussed in the literature review, computed tomography (CT) is a direct imaging technique that uses differences in density to isolate internal structures. Because parts are rotated throughout the scanning process, a three-dimensional image stack can be reconstructed from the CT scan (Desplentere et al. 2005). For the current investigation, impact damage within cross-ply composite plates was investigated using the Zeiss METROTOM 1500 computed tomography (CT) system. The METROTOM 1500 is an industrial CT scanning system, and the internal components are shown in

Figure 2.3. This figure also serves to illustrate the general operation of a CT scanning system. The leftmost component is the x-ray emitter, which produces a conical imaging beam. The rightmost component is the x-ray detector, which records and digitizes the x-ray intensity after the beam has passed through the specimen. In between the emitter and receptor is the specimen turntable. The specimen to be scanned is placed on the turntable, which rotates through 361° during the scan. Before beginning a scan, the turntable can be adjusted closer or farther from the x-ray emitter. Because of the conical beam, a small specimen placed close to the emitter will be magnified on the receiver. The METROTOM 1500 can produce voxel (volumetric pixel) resolutions ranging from 5 µm to 400 µm and can scan objects as large as a 300 mm by 300 mm cylinder (Zeiss 2015). The CT scans were reconstructed into 3D image stacks using VGStudio MAX by the CT Analyst at Schneider Electric.

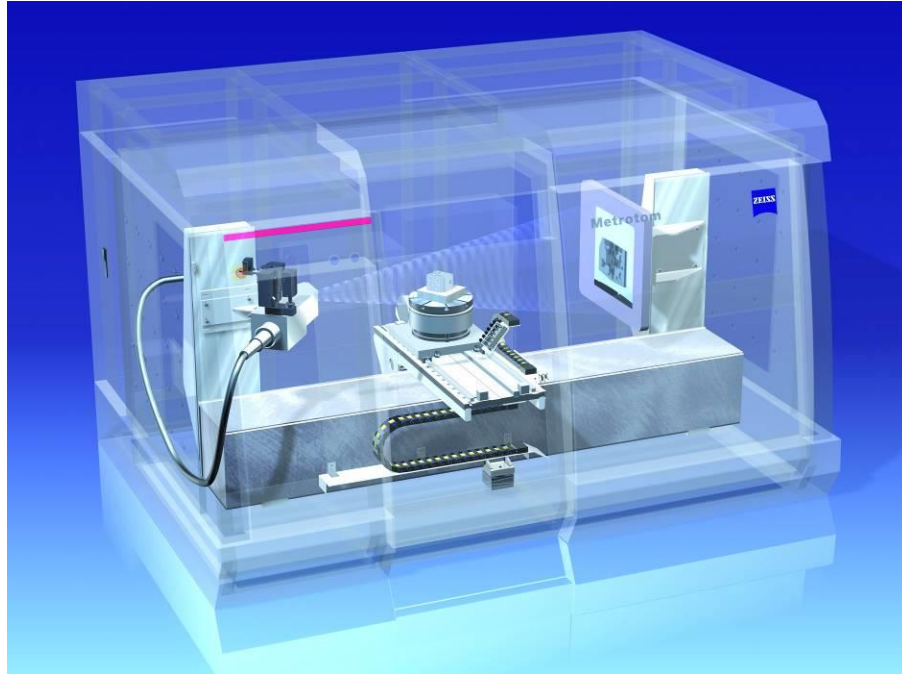


Figure 2.3: Zeiss METROTOM 1500 Industrial CT System (Zeiss 2015)

### 2.3 Summary of Experimental Setup

The goal of the current investigation was to perform CT imaging analysis on carbon fiber composite specimens that had been subject to low-velocity impact. The experimental setup used to perform the low-velocity impact tests employed the standard laboratory equipment and the impact procedures developed by Hart (2011). After impact characterization, the specimens were CT imaged using the Ziess METROTOM 1500 and analyzed following the basic procedure developed by Song (2014). Results of impact experimentation and CT imaging analysis are presented in the following chapters.

## CHAPTER 3

### LOW VELOCITY IMPACT EXPERIMENTAL RESULTS

#### 3.1 Material Characterization

The carbon fiber reinforced polymer composite specimens tested in this report were IM7/977-3 [0/90]<sub>8S</sub>, referred to as 32-ply symmetric cross-ply composite plates. Following standard composite naming conventions, the first part of the name indicates the fiber type and the second part indicates the matrix. In this case, IM7 refers to the high-performance continuous carbon fiber reinforcement, and 977-3 refers to the specific aerospace grade epoxy resin used. The numbers within the square brackets indicate the ply orientation. Cross-ply plates are represented by [0/90]<sub>#S</sub>, where the first ply is oriented at 0° and the next ply is orientated at 90°. The number in the subscript following the bracket indicates how many sets of [0/90] lamina are present, while the “S” indicates that the laminate is symmetric with respect to the middle plane. For example, [0/90]<sub>2S</sub> would designate a composite laminate with an expanded ply sequence of [0/90/0/90/90/0/90/0]. All of the specimens used in this investigation were composed of the same material, but they did not all originate from the same original plate. The 152.4 mm square specimens were water-jet cut from three larger IM7/977-3 [0/90]<sub>8S</sub> composite plates, designated as batch #9022, #9023, and #9024. The material type, 0° ply orientation, batch number, layup, and specimen number were all written on the front face of each specimen. Details on the specimens used in this investigation are included in Table 3.1.

Table 3.1: Summary of Materials Tested

Specimen Type	Batch Number	Number of Specimens	Specimen ID Numbers	Length/Width [mm]	Thickness [mm]
IM7/977-3 [0/90] <sub>8S</sub>	9023	5	1, 2, 3, 4, 5	150	4.47
IM7/977-3 [0/90] <sub>8S</sub>	9022	4	6, 7, 8, 9	150	4.47
IM7/977-3 [0/90] <sub>8S</sub>	9024	2	10, 11	150	4.47

### 3.2 Impact Characterization

#### 3.2.1 Preliminary Impact Testing

Eight 32-ply cross-ply IM7/977-3 specimens were used for initial impact testing.

The critical energy to produce just-visible damage was found through analysis of previous work and trial and error.

From impact testing performed by Hart (2011) on 16-ply cross-ply IM7/977-2 specimens, the critical energy to produce barely visible damage was determined to be 38.2 J. Therefore, for the 32-ply specimens the initial impact energy was chosen to be 75.5 J, twice the energy that was used on the 16-ply specimens and yielding the same energy per ply. One composite specimen, designated as specimen 1, was clamped into the impact testing machine and impacted at an energy of 75.5 J. This corresponded to a

mass of 12.831 kg dropped from a height of 0.60 m above the specimen. This impact energy was calculated using

$$U = mgh \quad (3.1)$$

where  $U$  is the potential (impact) energy in Joules,  $m$  is the mass in kilograms,  $g$  is the acceleration due to gravity ( $9.81 \text{ m/s}^2$ ), and  $h$  is the drop height in meters. The impact resulted in penetration into the specimen and significant back side damage, as shown in Figure 3.1 through Figure 3.3.

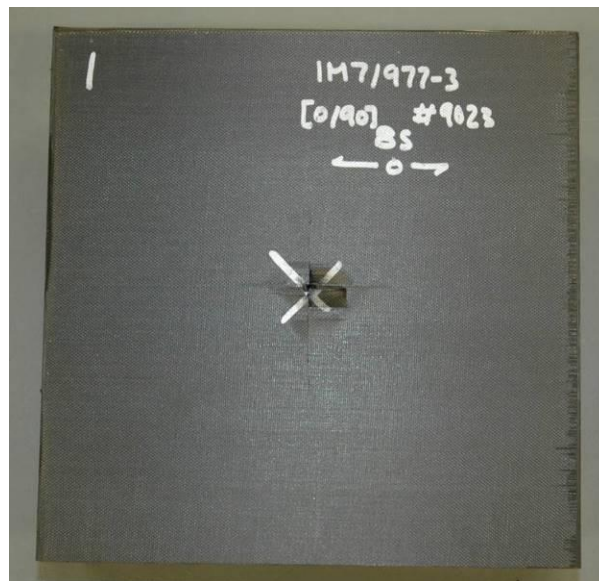


Figure 3.1: Impact Damage on the Top Surface of Specimen 1

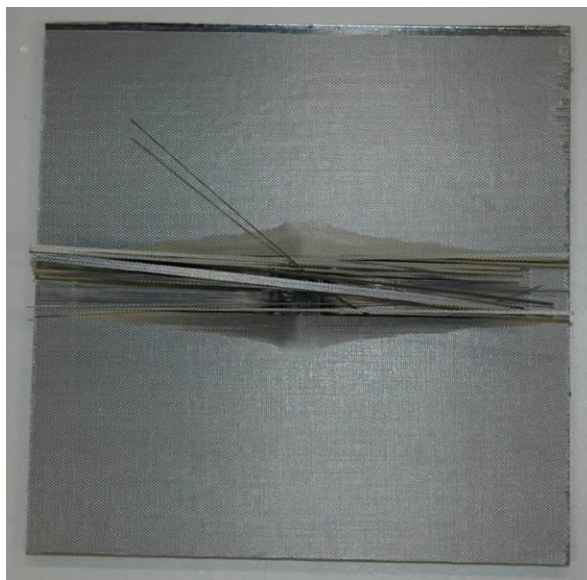


Figure 3.2: Impact Damage on the Bottom Surface of Specimen 1

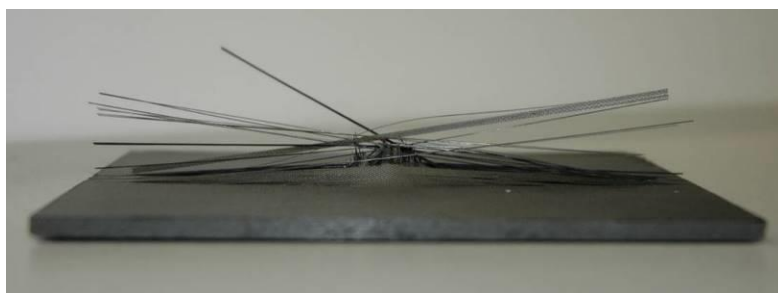


Figure 3.3: Side View of Impact Damage on the Bottom Surface of Specimen 1

To reduce the amount of damage produced during impact, the impact energy was decreased to half of the initial value, resulting in an impact energy of 37.76 J. To achieve this, the same mass was used (12.831 kg) and the height was decreased to 0.30 m. Specimen 2 was clamped into the impact testing machine and impacted at this energy. The specimen damage, seen in Figure 3.4 through Figure 3.6, was moderate in scope with a large dent on the top surface and raised delamination on the back surface. While the damage was less than that for specimen 1, it was still more severe than desired.

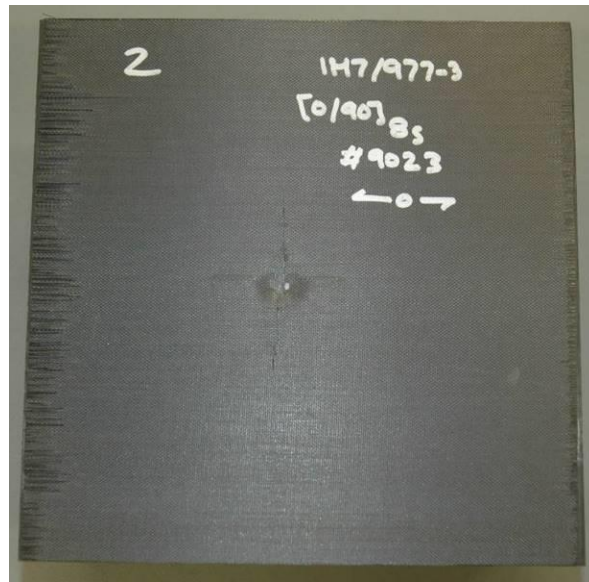


Figure 3.4: Impact Damage on the Top Surface of Specimen 2



Figure 3.5: Impact Damage on the Bottom Surface of Specimen 2



Figure 3.6: Side View of Impact Damage on the Bottom Surface of Specimen 2

### 3.2.2 “Low” Energy (20.77 J) Impact

To further reduce the amount of damage, the impact energy was again reduced by approximately a factor of two. Continuing with the same mass of 12.831 kg, the height

was set to 0.165 m above the specimen. This corresponded to an impact energy of 20.77 J. Specimen 3 was clamped into the impact testing machine and impacted at this energy. After impact, it was determined that the damage produced was as desired. The damage consisted of a small dent on the top surface of the specimen and a barely-visible raised area on the back surface. Specimens 4 and 5 were then also impacted in the same manner as specimen 3. The damage for specimens 3, 4, and 5 were all similar, with specimen 3 having representative visual damage for the three specimen impacted at 20.77 J. The damage to the front and back surfaces of all three specimens can be seen in Figure 3.7 through Figure 3.12. The results from the impacts of the first five specimens tested are shown in Figure 3.13 and Figure 3.14, and the results for the three specimen impacted at 20.77 J are shown in Figure 3.15 and Figure 3.16.

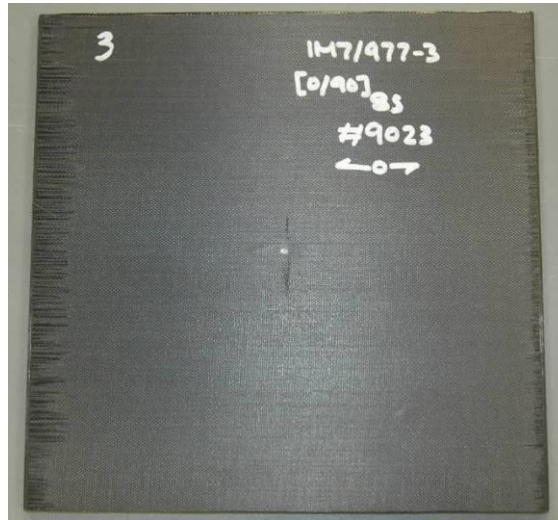


Figure 3.7: Impact Damage on the Top Surface of Specimen 3

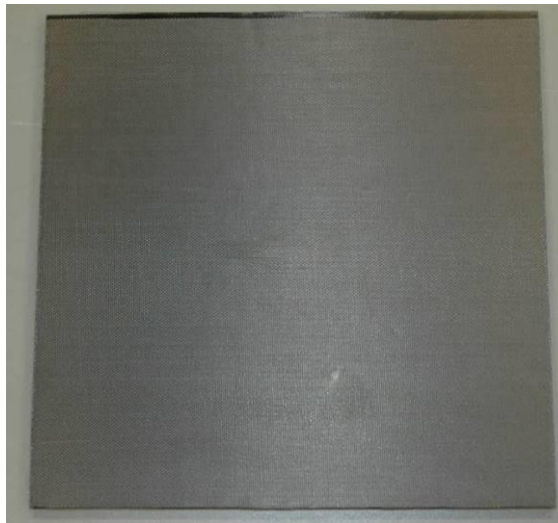


Figure 3.8: Impact Damage on the Bottom Surface of Specimen 3

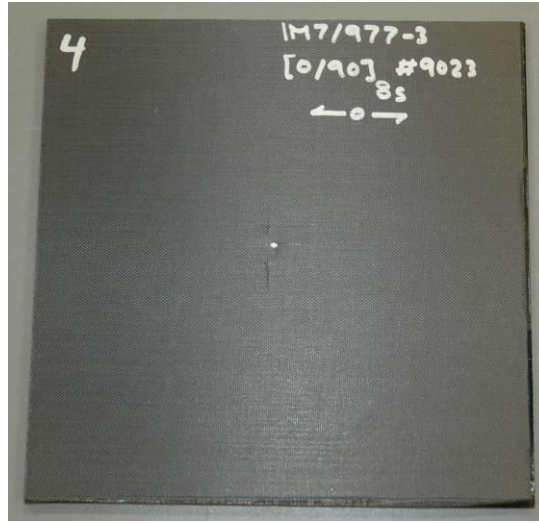


Figure 3.9: Impact Damage on the Top Surface of Specimen 4

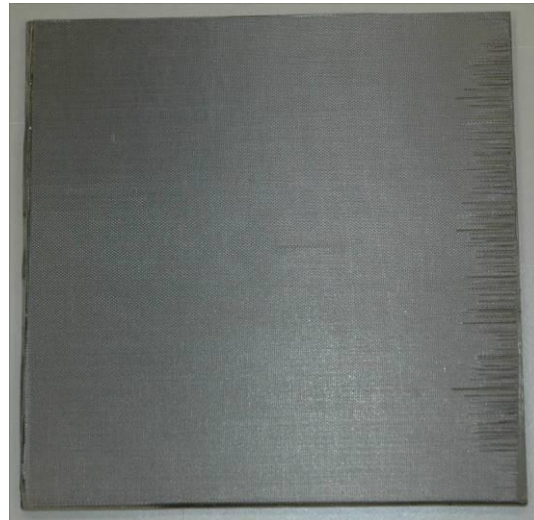


Figure 3.10: Impact Damage on the Bottom Surface of Specimen 4

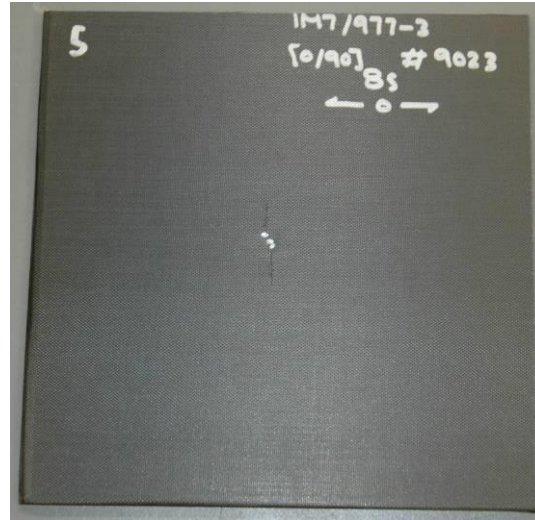


Figure 3.11: Impact Damage on the Top Surface of Specimen 5

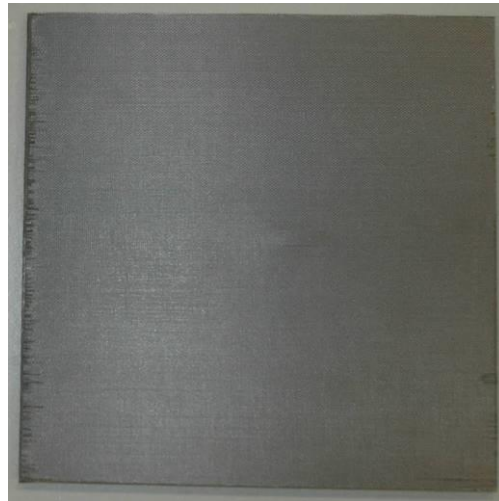


Figure 3.12: Impact Damage on the Bottom Surface of Specimen 5

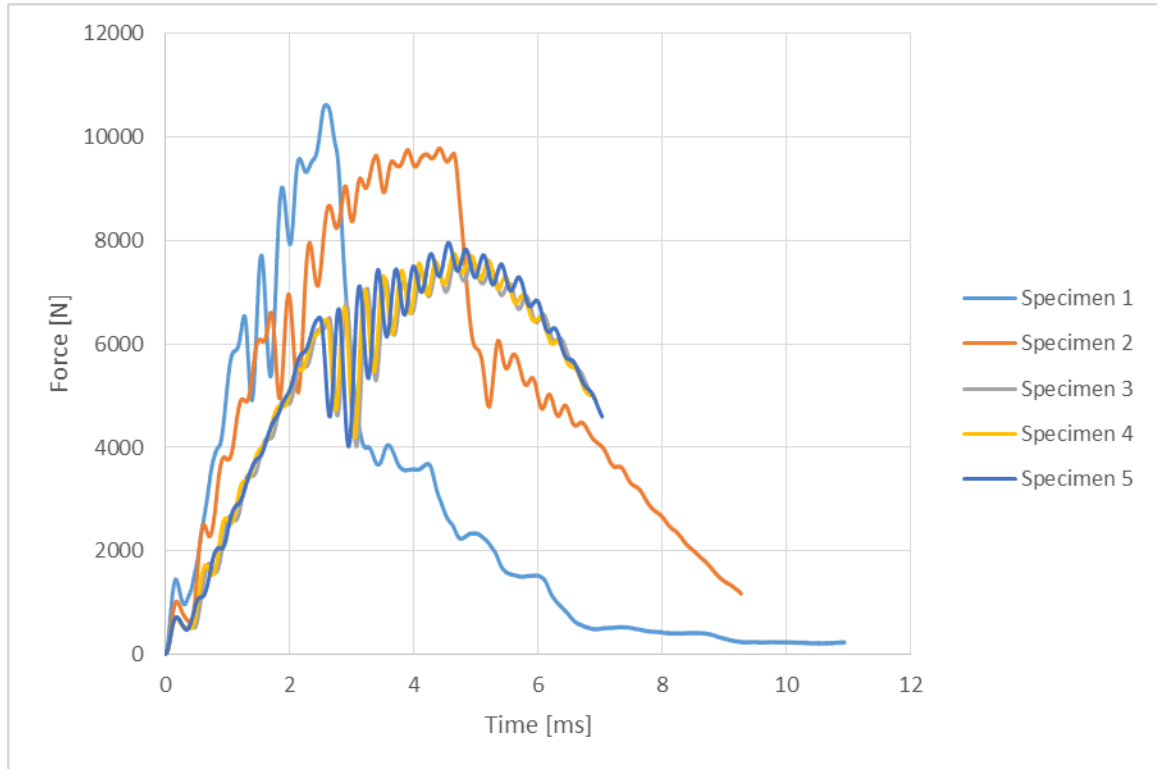


Figure 3.13: Force versus Time for Impact Characterization of Specimens 1 – 5

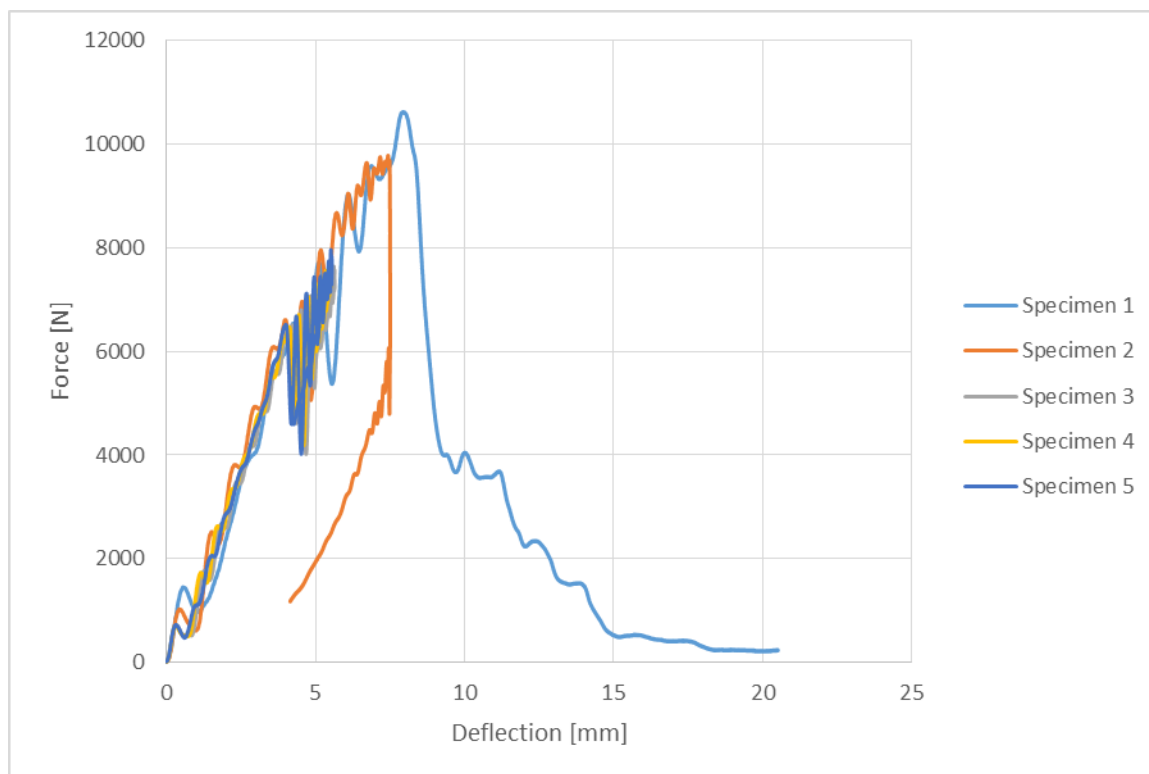


Figure 3.14: Force versus Deflection for Impact Characterization of Specimens 1 – 5

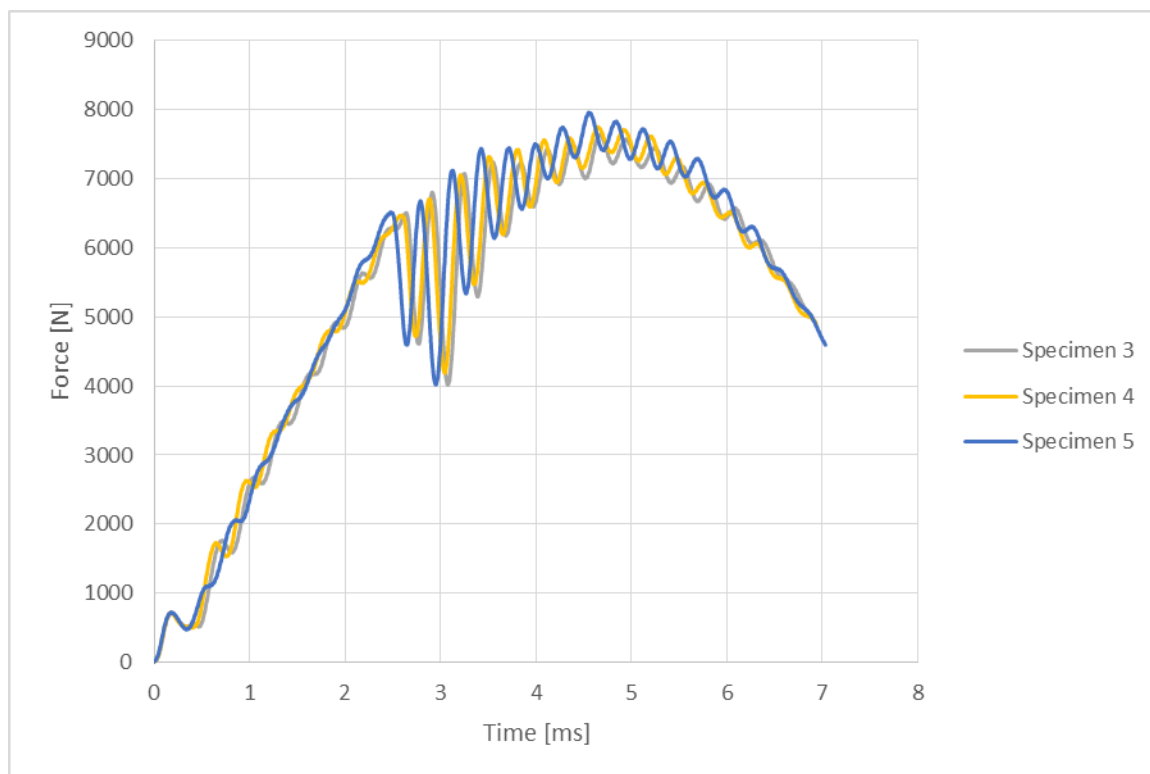


Figure 3.15: Force versus Time for Impact Characterization of Specimen 3, 4, & 5

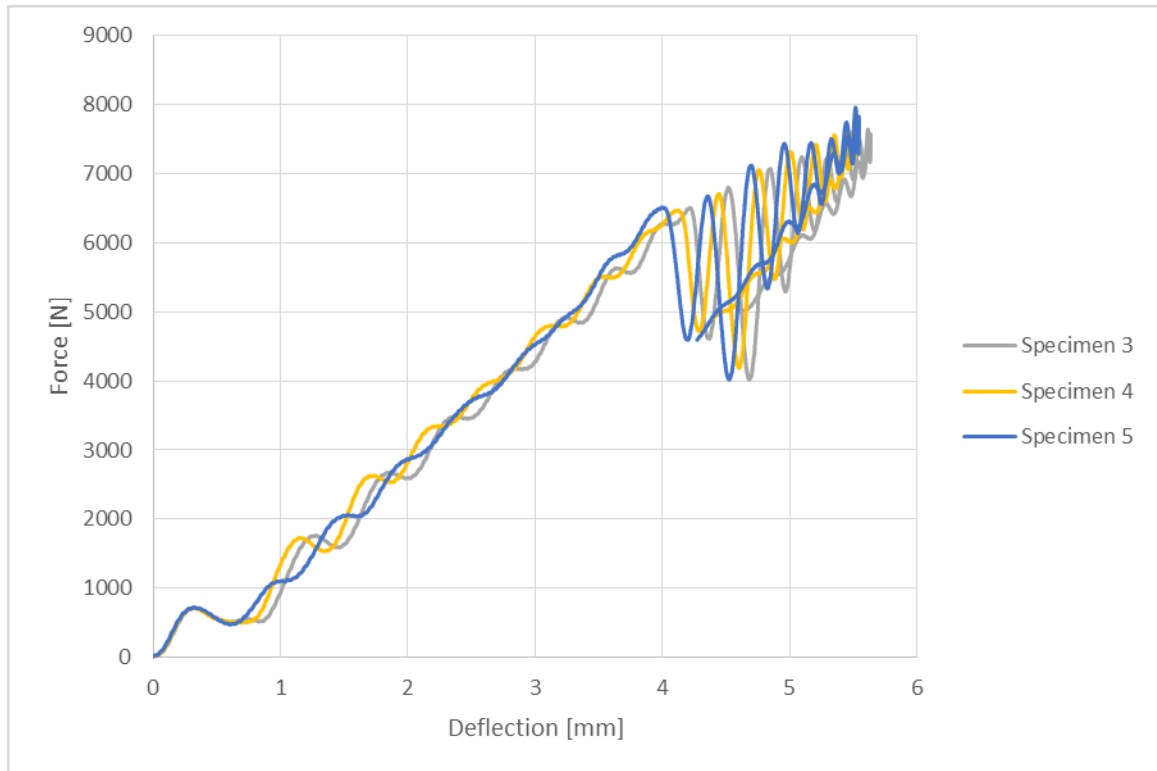


Figure 3.16: Force versus Deflection for Impact Characterization of Specimens 3, 4, & 5

As would be expected, specimen 1 experienced the highest load before failing, specimen 2 had the next highest load, and specimens 3, 4, and 5 all withstood approximately the same load, as shown in Figure 3.13. Further, Figure 3.15 indicates that the three specimens impacted at 20.77 J experienced nearly identical loading over the impact event. While the loading curves for specimens 3, 4, and 5 do not perfectly overlap, the onset of damage within the plate, indicated by the decreases in force, occur at similar force levels. This supports the conclusion that the impact events were similar and that comparable damage should be present within all three specimens. The deflection

results, Figure 3.14 and Figure 3.16, also indicate that specimens 3, 4, and 5 had similar responses to the impact.

### 3.2.3 “Intermediate” Energy (29.27 J) Impact

From testing of the first five specimens, the impact energy to produce barely visible damage was determined to be 20.77 J. Then, in order to analyze the effect of impact energy on internal damage, an impact producing an intermediate amount of damage to the composite plates was desired. This impact energy was determined by selecting an energy half-way between the impact energies used on specimens 2 (high energy, 37.76 J) and 3 (low energy, 20.77 J), which resulted in a target impact energy of 29.27 J. Specimen 6 was clamped into the impact testing machine and impacted with a mass of 12.831 kg at a height of 0.223 m. After impact, it was determined that the amount of damage produced was acceptable. The damage consisted of a small indentation and short cracks on the top surface of the specimen and a small raised area on the back surface. Specimens 7 and 8 were then also impacted in the same manner as specimen 6. Because it was noted that the data collection for specimen 6 did not capture the entire impact event, the length of data collection was increased for specimens 7 and 8. No other testing or data collection parameters were altered. The damage for specimens 6, 7, and 8 were similar in type and magnitude, and the damage can be seen in Figure 3.17 through Figure 3.25. The results from the impacts of these three specimen are shown in Figure 3.26 and Figure 3.27, and are compared to the results of specimens 3, 4, and 5 in Figure 3.28 and Figure 3.29.

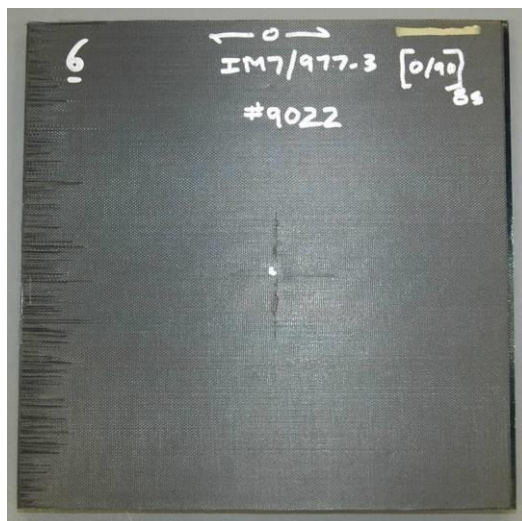


Figure 3.17: Impact Damage on the Top Surface of Specimen 6

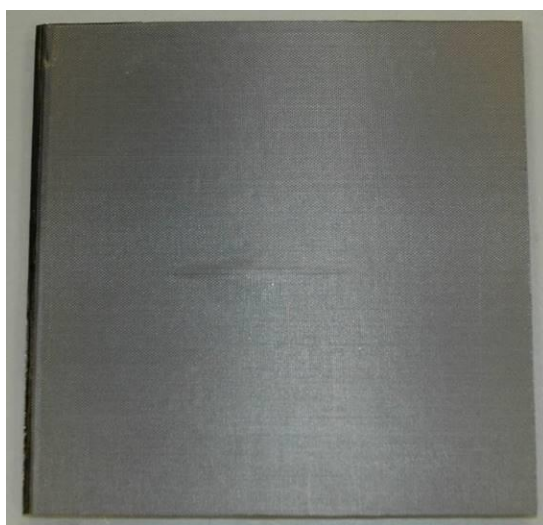


Figure 3.18: Impact Damage on the Bottom Surface of Specimen 6



Figure 3.19: Side View of Impact Damage on the Bottom Surface of Specimen 6



Figure 3.20: Impact Damage on the Top Surface of Specimen 7

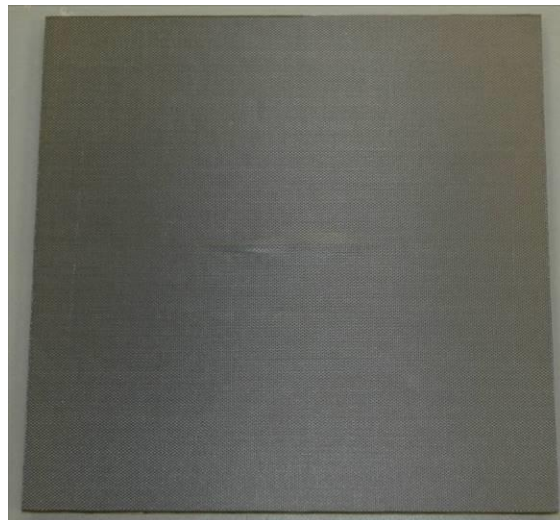


Figure 3.21: Impact Damage on the Bottom Surface of Specimen 7



Figure 3.22: Side View of Impact Damage on the Bottom Surface of Specimen 7

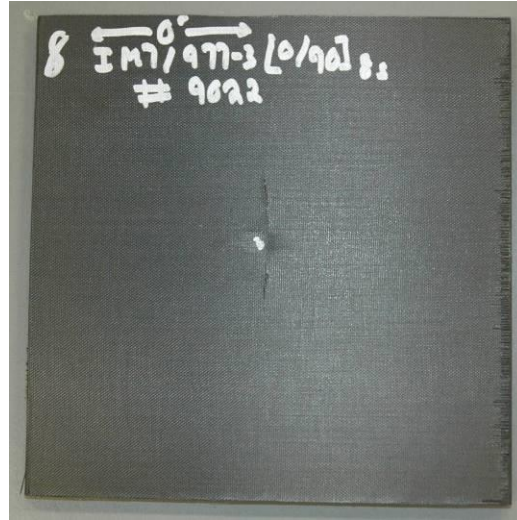


Figure 3.23: Impact Damage on the Top Surface of Specimen 8

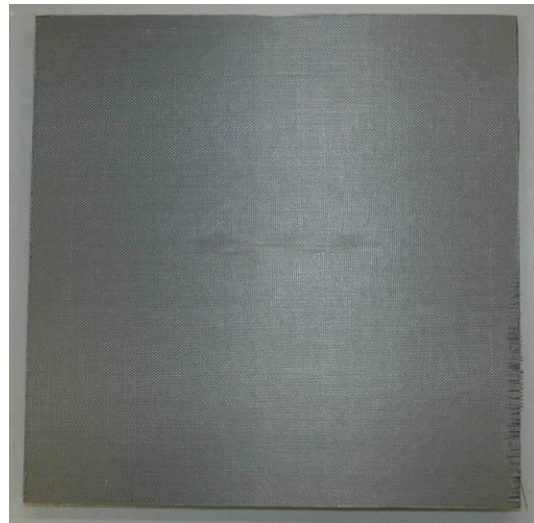


Figure 3.24: Impact Damage on the Bottom Surface of Specimen 8



Figure 3.25: Side View of Impact Damage on the Bottom Surface of Specimen 8

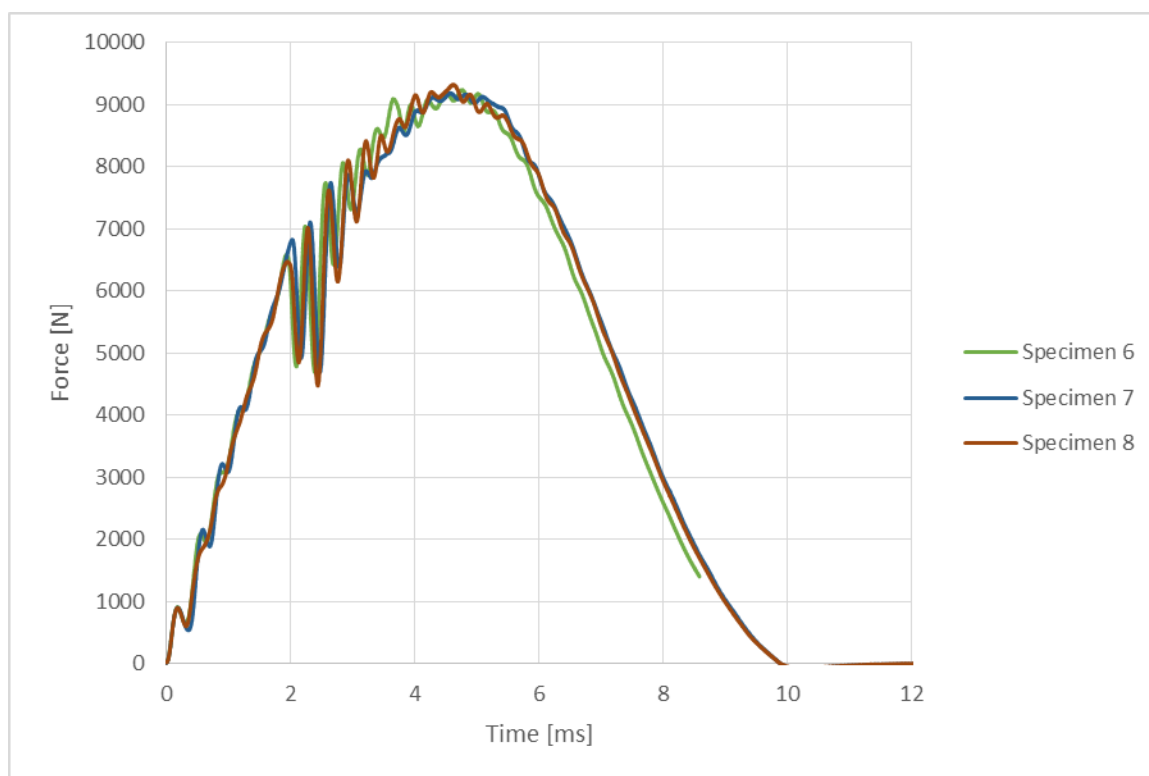


Figure 3.26: Force versus Time for Impact Characterization of Specimens 6, 7, & 8

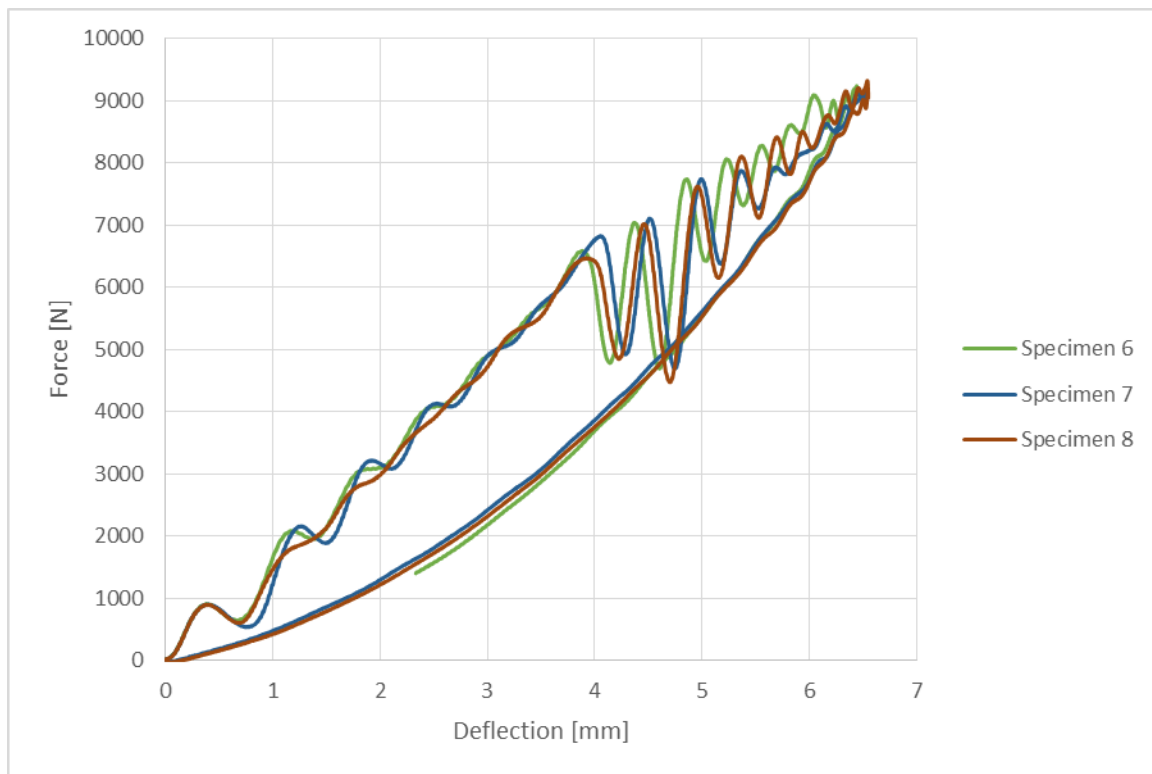


Figure 3.27: Force versus Deflection for Impact Characterization of Specimens 6, 7, & 8

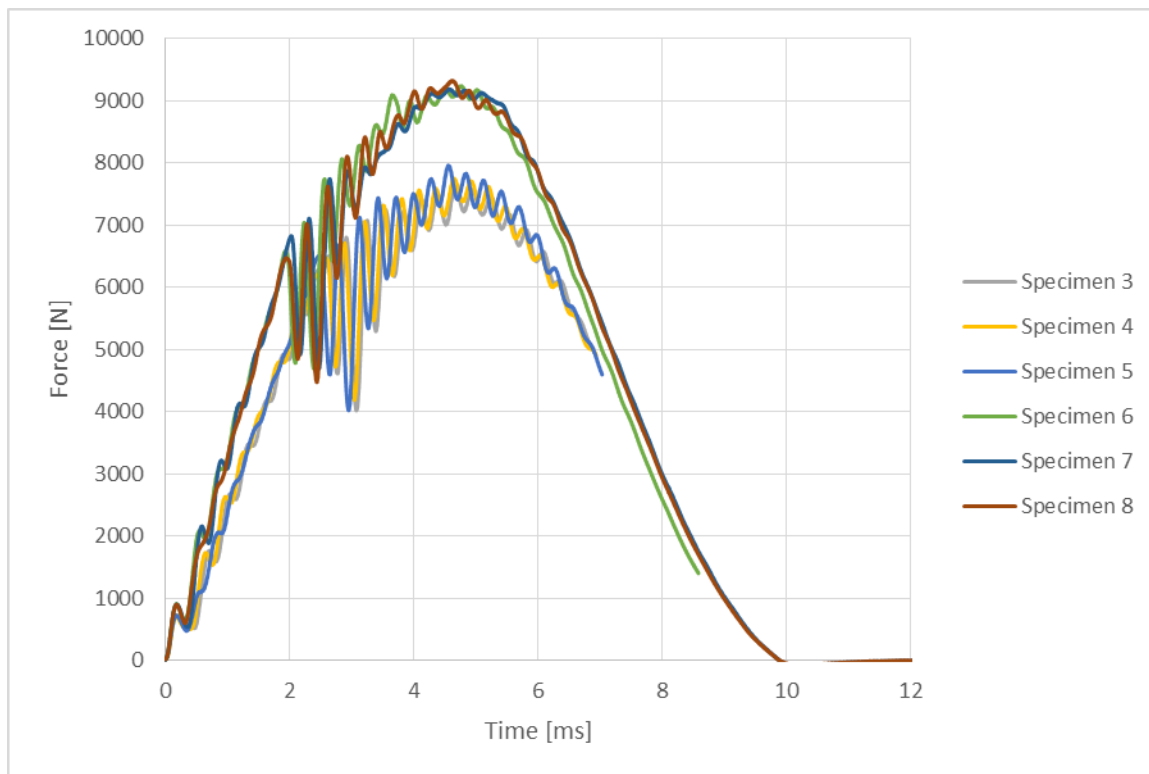


Figure 3.28: Force versus Time for Impact Characterization of Specimens 3 – 8

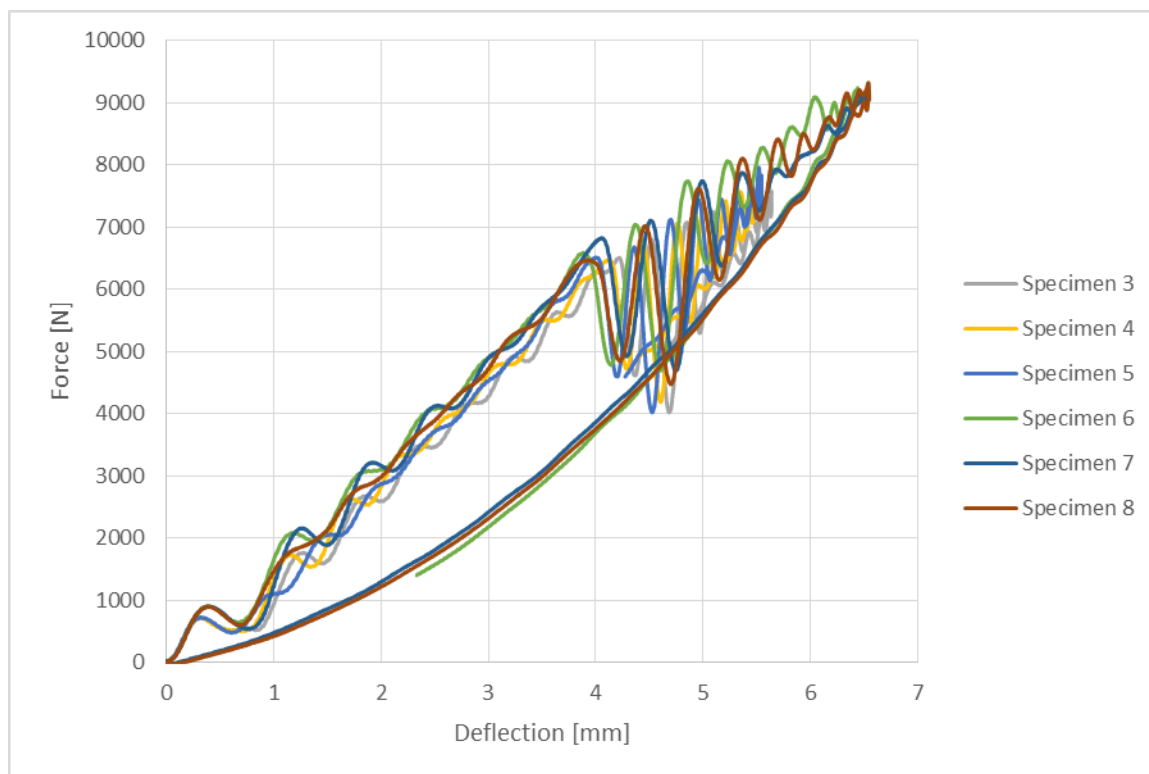


Figure 3.29: Force versus Deflection for Impact Characterization of Specimens 3 – 8

As with specimens 3, 4, and 5, the loading on specimens 6, 7, and 8 all exhibit the same trends. The loading curves for these three specimens do not perfectly align, but they all have the same general structure and indicate damage occurred within the specimens at approximately the same applied force. As noted previously, the data collection length was increased for specimens 7 and 8, which is why the force versus time and force versus deflection curves for those two specimens extend beyond that of specimen 6. Comparing between the specimens impacted at 20.77 J and 29.27 J, it can be seen that the specimens impacted at the higher energy had a larger peak force and greater

deflection. This result follows with the expected outcome of the impact tests, where greater impact energy leads to larger forces and deflections.

#### 3.2.4 “Intermediate” Energy (29.25 J) DELRIN Impact

In order to analyze the effect of the tup insert on impact damage, the impact conditions of specimens 6, 7, and 8 were replicated using a different tup insert. For these tests, instead of using the hemispherical tool steel tup insert, a flat-ended tup insert with the same diameter (15.88 mm) but constructed of DELRIN® was used. This tup insert was the same as was used in the previous investigations conducted by Hart (2011). As it was believed that the damage from this test would be minimal, specimens 9, 10, and 11 had the back face painted white. This would provide higher contrast and allow small amounts of damage to be visible. Specimens 9, 10, and 11 were then individually clamped into the testing machine and impacted with a mass of 12.824 kg at a height of 0.223 m which produced a target impact energy of 29.25 J, similar to specimens 6, 7, and 8. After impact, it was noted that no visible damage was produced on any of the three specimens. Images of the top and bottom surfaces of specimens 9, 10, and 11 are presented in this section, as shown in Figure 3.30 through Figure 3.35. The results from the impacts of these three specimens are shown in Figure 3.36 and Figure 3.37, and are compared to the results of specimens 6, 7, and 8 in Figure 3.38 and Figure 3.39.

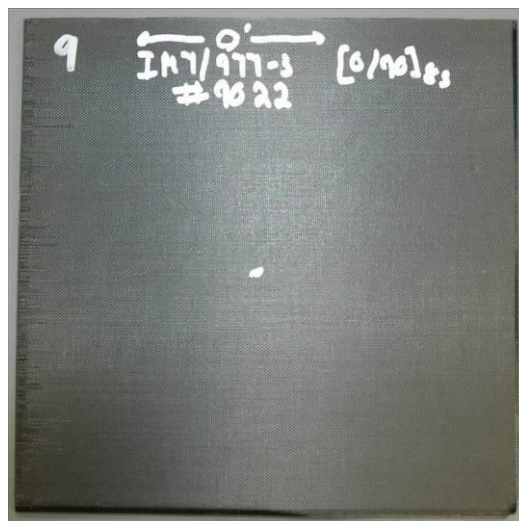


Figure 3.30: Impact Damage on the Top Surface of Specimen 9



Figure 3.31: Impact Damage on the Bottom Surface of Specimen 9

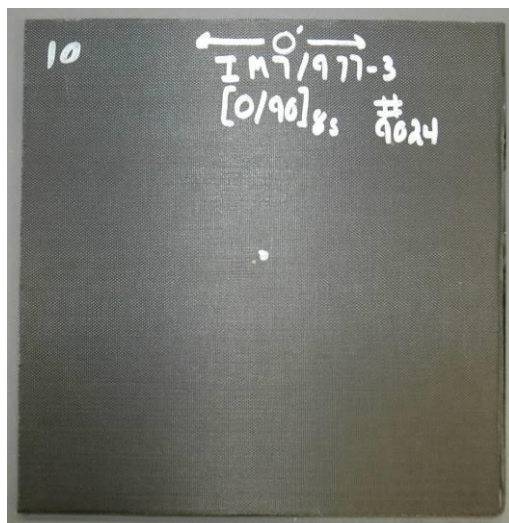


Figure 3.32: Impact Damage on the Top Surface of Specimen 10

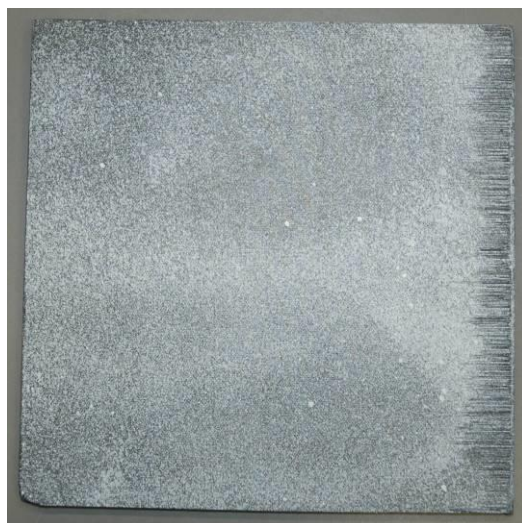


Figure 3.33: Impact Damage on the Bottom Surface of Specimen 10

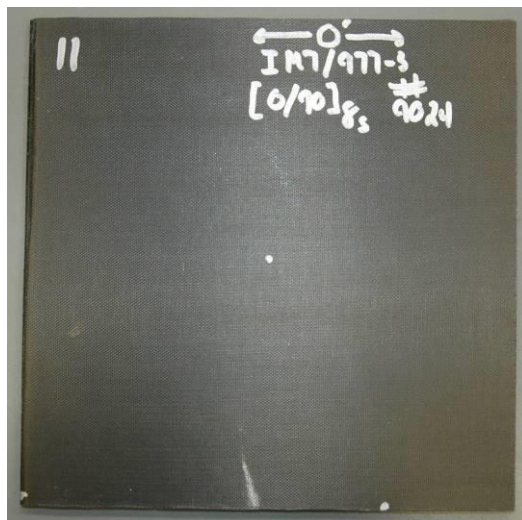


Figure 3.34: Impact Damage on the Top Surface of Specimen 11



Figure 3.35: Impact Damage on the Bottom Surface of Specimen 11

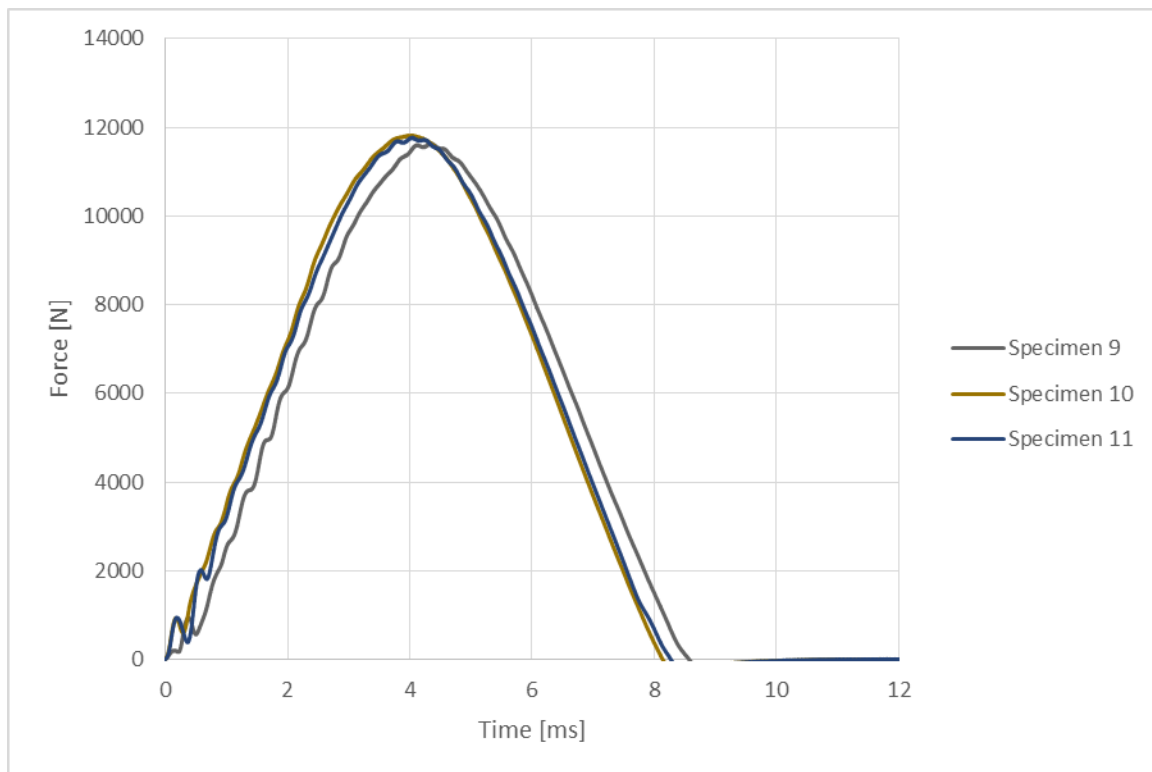


Figure 3.36: Force versus Time for Impact Characterization of Specimens 9, 10, & 11

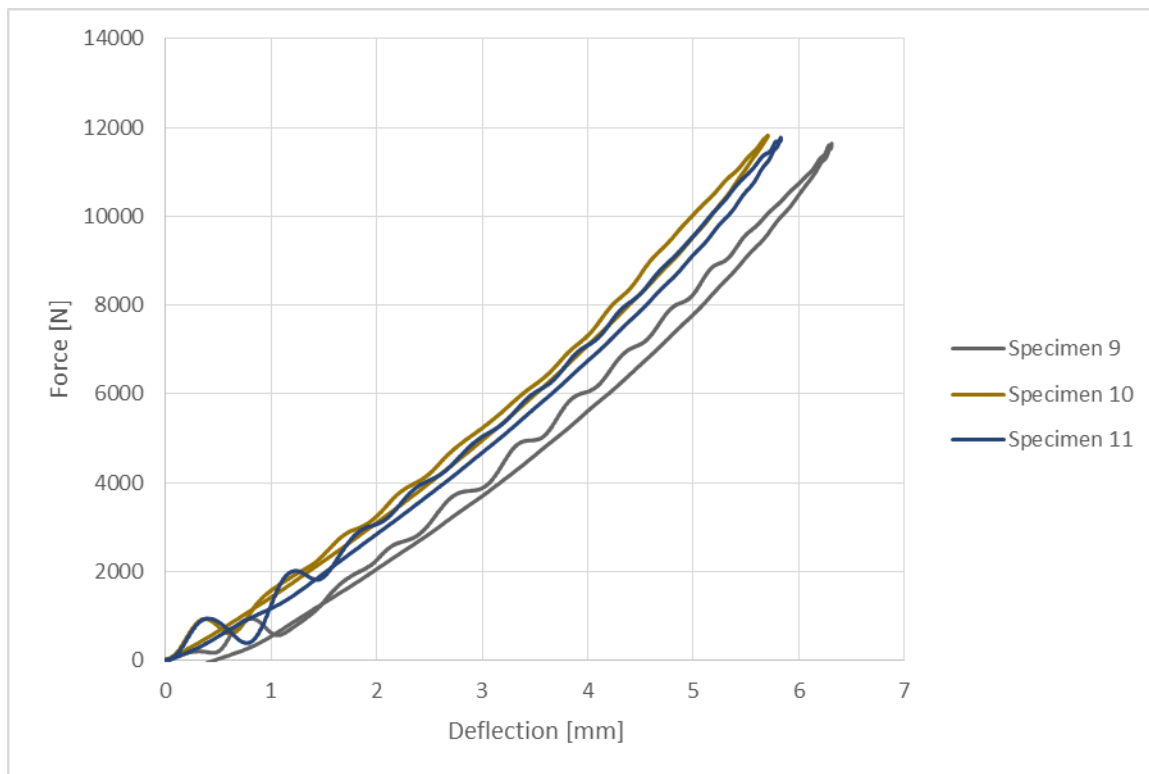


Figure 3.37: Force versus Deflection for Impact Characterization of Specimens 9, 10, & 11

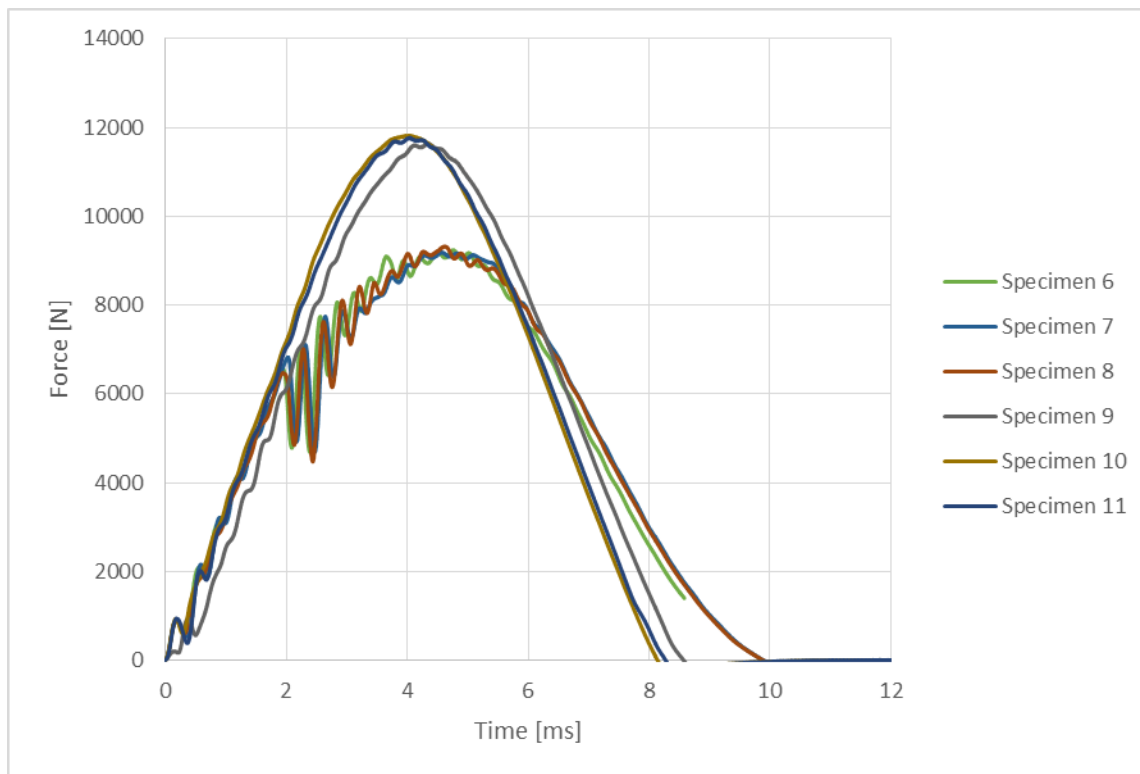


Figure 3.38: Force versus Time for Impact Characterization of Specimens 6 – 11

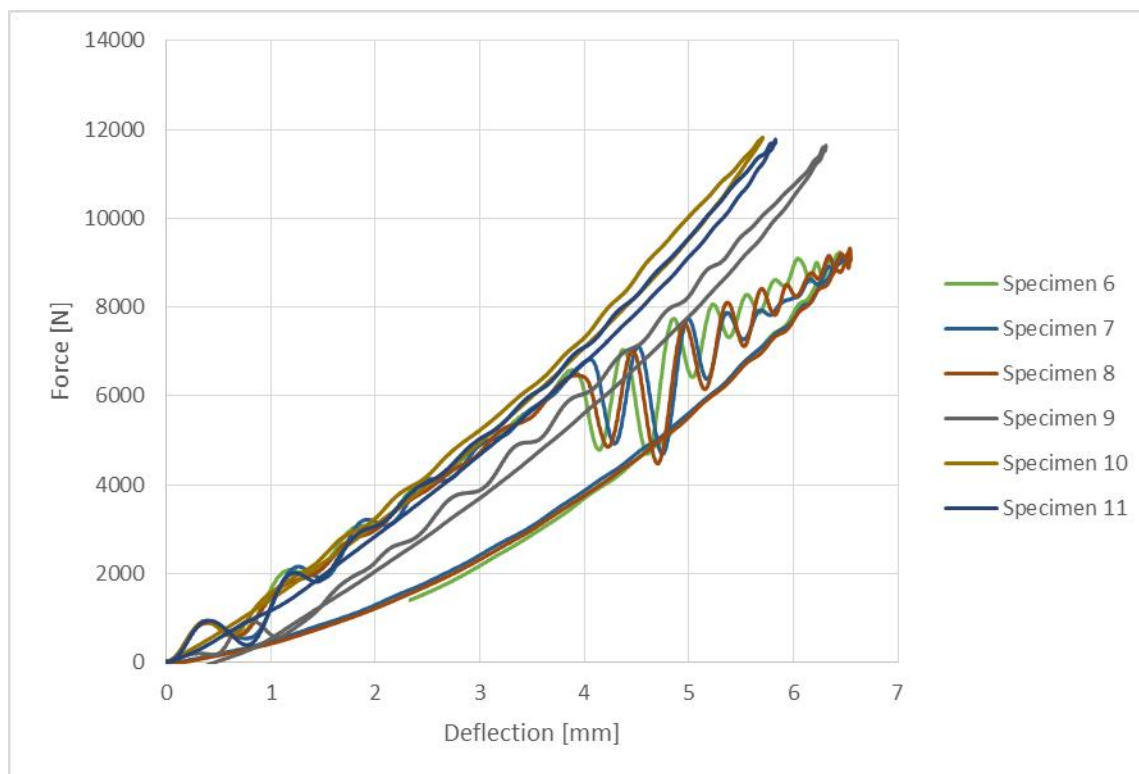


Figure 3.39: Force versus Deflection for Impact Characterization of Specimens 6 – 11

While the impact energy and boundary conditions of the tests remained the same, altering the tup insert did have an effect on the impact results. The DELRIN® tup insert, used for specimens 9, 10, and 11, produced higher peak force and had a shorter impact duration as compared to the steel tup insert, used for specimens 6, 7, and 8, as seen in Figure 3.38. Additionally, the specimens impacted with the DELRIN® tup insert had somewhat smaller deflections than the specimens impacted with the steel tup insert, as seen in Figure 3.39.

### 3.2.5 Impact Characterization Results

To numerically compare the results from the impact tests, the relevant data was recorded. The peak load for each specimen was measured by the instrumented load cell on the Instron impact testing machine tup. The impact energy was calculated by the Instron software based on the measured velocity, the mass (set as an input to the software), and the principle of kinetic energy. The absorbed energy was automatically calculated by the Instron software by integrating the force versus deflection curve for each impact. These results are tabulated in Table 3.2.

Table 3.2: Impact Characterization Data for 32-ply Symmetric Cross-Ply Specimens

Specimen	Impact Mass [kg]	Impact Height [m]	Impact Velocity [m/s]	Impact Energy [J]	Tup Insert Type	Absorbed Energy [J]	Peak Load [N]	Damage
1	12.831	0.600	3.4071	74.4732	Tool Steel Hemisphere	67.8839	10628.5	Significant
2	12.831	0.300	2.4139	37.3826	Tool Steel Hemisphere	29.7847	9785.7	Moderate
3	12.831	0.165	1.7207	18.9951	Tool Steel Hemisphere	15.4207	7642.8	Barely visible
4	12.831	0.165	1.7156	18.8826	Tool Steel Hemisphere	14.5323	7752.1	Barely visible
5	12.831	0.165	1.7175	18.9245	Tool Steel Hemisphere	13.6988	7963.2	Barely visible
6	12.831	0.233	2.0977	28.2304	Tool Steel Hemisphere	11.7148	9241.4	Slight
7	12.831	0.233	2.0998	28.2870	Tool Steel Hemisphere	8.9193	9192.1	Slight
8	12.831	0.233	2.1018	28.3409	Tool Steel Hemisphere	9.3316	9326.0	Slight
9	12.824	0.233	2.1057	28.4462	DELTRIN® Flat-ended cylinder	2.0639	11644.7	None visible
10	12.824	0.233	2.1047	28.4191	DELTRIN® Flat-ended cylinder	1.4061	11821.9	None visible
11	12.824	0.233	2.1038	28.3948	DELTRIN® Flat-ended cylinder	1.6279	11776.2	None visible

For a given impact energy, absorbed energy is greater in specimens that incur less damage. For example, since specimens 3, 4, and 5 all had similar visible damage, this suggests that specimen 5 has the greatest internal damage of the three, followed by specimen 4 and then specimen 3. The difference in absorbed energy between specimen 6 and specimens 7 and 8 can be explained by the increased data collection time. Because the Instron software calculates the absorbed energy from the integral of the force versus deflection curve, collecting data across the entire impact event leads to a closed curve and results in a smaller area of integration. Comparing the absorbed energy for the specimens

impacted with the tool steel and DELRIN® tup inserts at the same energy (specimens 6 – 8 and specimens 9 – 11, respectively), it can be seen that the specimens impacted with the DELRIN® tup insert had lower absorbed energy. This would indicate that these specimens incurred less damage. It is also interesting to note that the impact force in all three specimens impacted by the DELRIN® flat-ended tup insert were larger compared to the impact force in the specimens impacted by the tool steel hemispherical tup insert. This observation is consistent with previous studies, where a similar observation was made when comparing flat-ended and hemispherical impactors of the same diameter (Wright, Fleck, and Stronge 1993). Furthermore, it was also observed previously that the amount of impact energy required to perforate a composite target is larger in the case of a flat-ended cylindrical impactor than in the case of a spherical impactor (Powell, Zohdi, and Johnson 2008). These conclusions are consistent with the results of the previous work.

### 3.3 Comparison to Previous Work

As mentioned in an earlier section, the initial impact energy used for specimen 1, 74.5 J, was calculated by doubling the critical energy required to initiate damage in 16-ply symmetric cross-ply composite plates as determined by Hart (2011). Thus, the impact energy per ply was the same for specimen 1 tested in this study and for the 16-ply cross-ply specimens tested by Hart. Despite using the same per-ply energy and similar composite material, the results of the tests on 32-ply and 16-ply specimens were drastically different. Specimens tested by Hart developed only barely visible damage when impacted by a mass of 12.97 kg dropped from a height of 0.30 m, which

corresponded to an impact energy of 38.2 J. Table 3.3 shows the impact test results reported in Hart's work, and Figure 3.40 shows damage on the bottom surface of specimen 48 tested in Hart's study. Specimen 1 tested in this study, which was impacted at the same impact energy per ply, experienced massive damage as seen in Figure 3.1 through Figure 3.3. Therefore, there is a significant difference in the amount of damage produced by the same impact energy per ply in both studies. This difference can be explained by the differences in the tup insert material properties and geometry as well as the different clamping fixtures used in these studies. Because the primary objective of Hart's work was to investigate the effects of electrification on composite specimens, a non-conductive fixture and tup insert were used in his experimentation. The tup insert was designed by Zantout (2009) and was a flat-ended cylinder with a diameter of 5/8 inches (15.88 mm) machined from DELRIN®, a dielectric polymer. DELRIN® has excellent impact properties, but it could shatter when performing impacts at high energy levels and therefore was not deemed suitable for the current investigation. The test fixture used by Hart was also designed by Zantout, and consisted of copper electrodes (labeled as (1) in Figure 3.42), wooden top and bottom plates (labeled (2) and (3), respectively), and an aluminum clamping plate (labeled (4)). The tup insert can be seen in Figure 3.41 and the fixture can be seen in Figure 3.42.

Table 3.3: Impact Characterization Data for 16-ply Cross-Ply Specimens (Hart 2011)

Specimen #	Electrical	Mass [kg]	Height [m]	Velocity [m/s]	Impact Energy [J]	Absorbed Energy [J]	Peak Load [N]	Peak Current [A]	Visible Damage
Sample 48	no pulse	12.97	0.300	2.434	38.4266	40.9138	9863.3	---	yes
Sample 49	no pulse	12.97	0.300	2.432	38.3706	41.5141	9844.8	---	yes
Sample 50	no pulse	12.97	0.300	2.433	38.4042	41.4866	9785.8	---	none

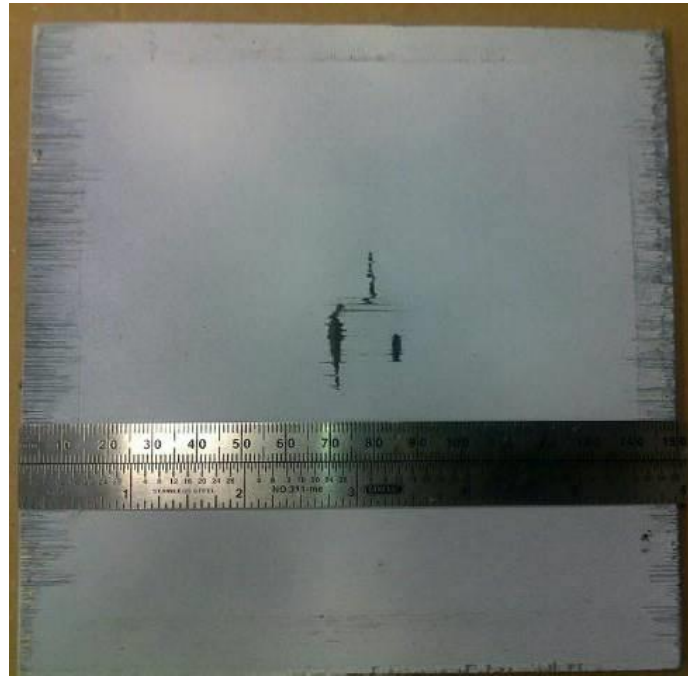


Figure 3.40: Visible Damage on the Back Side of Sample 48 (Hart 2011)



Figure 3.41: Tool Steel (left) and DELRIN® (right) Tup Insert (Zantout 2009)

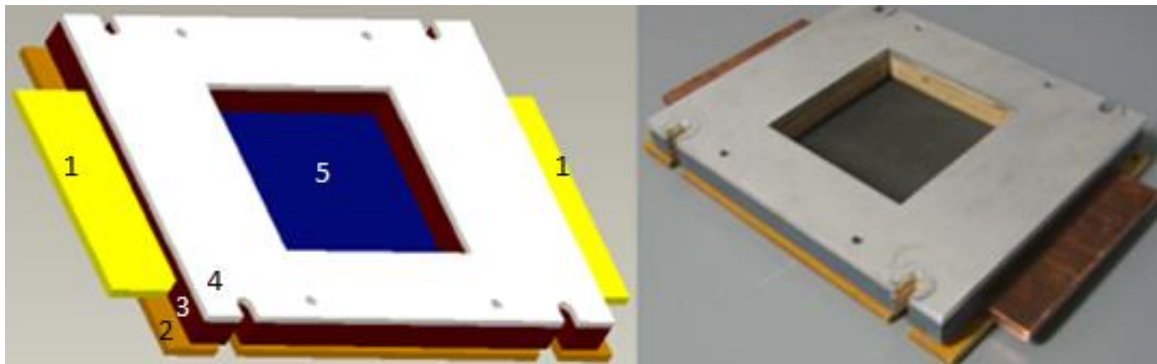


Figure 3.42: Test Fixture 3D Model (left) and Fabricated Assembly (right) (Zantout 2009)

Using the DELRIN® tup insert and wooden fixture, Hart was able to produce just-visible damage in a 16-ply symmetric cross-ply specimen impacted at 38.2 J, or 2.3875 J/ply. The specific impact conditions and results from Hart's tests on 16-ply

symmetric cross-ply specimens can be seen in Table 3.3. Initial testing on specimen 1 attempted to replicate Hart's results by using the same impact energy per ply. This resulted an impact at an energy of 75.5 J using a mass of 12.831 kg and a height of 0.60 m, or 2.369 J/ply. However, the damage produced during the two impact tests were different, with the thicker 32-ply specimen suffering more damage than the 16-ply specimens. These results are summarized in Table 3.4.

Table 3.4: Comparison to Previous Impact Conditions and Results

Researcher	Specimen Type	Mass [kg]	Height [m]	Impact Energy [J]	Tup Insert	Fixture	Visible Damage
Hart (2011)	IM7/977-2 [0/90] <sub>4S</sub>	12.97	0.30	38.2	DERLIN®; Flat-ended cylinder	Wood	Just-visible damage on back
Demerath (2015)	IM7/977-3 [0/90] <sub>8S</sub>	12.831	0.60	75.52	Tool Steel; Hemispherical tip	Steel	Significant damage, with large raised areas on back

While the result of the thicker composite plate receiving more damage for the same energy per ply is counterintuitive, the discrepancies in damage likely arise from the differences in the fixture and tup insert used. As noted by Abrate (1998), at the same energy and for the same geometry, a projectile with a higher modulus of elasticity results

in a higher contact stiffness. This creates higher contact forces and a smaller contact zone, leading to more damage. In this investigation, the tool steel tup insert had a modulus of elasticity of 207 GPa, which is significantly stiffer than the DELRIN® tup insert, which had a modulus of approximately 3.2 GPa (DuPont). Therefore, the tool steel tup insert would be expected to produce more damage for a given impact energy. Additionally, the steel fixture used is stiffer than the wooden fixture, and so would deform less and absorb less energy during the impact. This would also contribute to an increase in specimen damage.

In addition to material differences, the tup inserts also had different tip geometries, seen in Figure 3.41. The tool steel tup insert had a hemispherical tip and the DELRIN® tup insert had a flat end. The flat end would distribute the impact force over a larger contact area, and the decreased stress concentration at the center could contribute to the decreased level of damage. The effect of geometry and impactor size was studied by Icten (2013), who noted that damage increased with decreased impactor contact area. In other words, it was found that an impactor with a smaller contact area, measured by Icten in terms of diameter, produced a larger amount of damage for a given impact energy. Moreover, the density of steel is larger than the density of DELRIN®, and therefore the kinetic energy was larger in the case of the steel impactor compared to the DELRIN® impactor. This provided a slight contribution to the larger amount of damage produced in the impact of a composite plate by a steel impactor. The results obtained from the present study are consistent with the previous research.

### 3.4 Theoretical Contact Analysis

As discussed by Abrate (1998) low-velocity impact can be generally approximated as quasi-static loading, and so Hertzian contact laws are valid for laminated composites for relatively low force levels. Applicability of the Hertzian contact theory is based on the assumption that the distribution of stresses at any moment of the initial low-velocity impact is the same as that in the corresponding static contact problem. The Hertzian contact problem was originally formulated for the contact of isotropic bodies (Hertz 1881, Johnson 1985). The key assumptions that enabled a closed-form solution to the normal contact problem were: (i) absence of friction in the contact, (ii) small size of the contact area compared to the dimensions of contacting bodies and their relative radii of curvature (as a result, the contact of half-spaces was considered instead of contact of bodies of finite geometry), and (iii) the presumed linear elastic material response. According to the Hertzian theory the contact radius is determined as

$$a = \left( \frac{3Fr \left( \frac{1 - \nu_1^2}{E_1} + \frac{1 - \nu_2^2}{E_2} \right)}{4} \right)^{1/3} \quad (3.2)$$

where  $a$  is the contact radius,  $F$  is the contact force,  $r$  is the radius of the contacting sphere, and  $\nu$  and  $E$  are the Poisson's ratio and elastic modulus, respectively, for the contacting bodies 1 and 2. For sphere on half-space contact, the normal stress distribution in the contact zone is parabolic:

$$\sigma(r) = -p_0 \sqrt{1 - \frac{r^2}{a^2}}, \quad r \leq a \quad (3.3)$$

where  $p_0$  is the contact pressure. The relationship between maximum contact pressure, contact force and contact radius is as follows:

$$p_0 = 1.5 \frac{F}{\pi a^2} \quad (3.4)$$

Note that equations (3.2) – (3.4) are applicable only to the contact stress analysis of a plate impacted by a tup insert with a hemispherical tip.

In the case of a rigid flat-ended cylindrical frictionless punch of radius  $b$  pressed against an elastic half-space, the stress distribution has the form (Johnson, 1985)

$$\sigma(r) = -\frac{p_0}{\sqrt{1 - \frac{r^2}{b^2}}}, \quad r \leq b \quad (3.5)$$

and the contact force  $F$  is determined as

$$F = \frac{2}{3} \pi p_0 b^2 \quad (3.6)$$

To investigate the effect of the material properties on the contact stresses, contact between a tool steel hemispherical impactor and a 977-3 epoxy resin half-space as well as between a DELRIN® hemispherical impactor and a 977-3 epoxy resin half-space were considered. The material properties for tool steel and DELRIN® are shown in Table 3.5.

Table 3.5: Material Properties for Contact Analysis

Material	$E$ [GPa]	$\nu$	$\rho$ [g/cm <sup>3</sup> ]	Yield Strength [MPa]
Tool Steel	207	0.295	7.85	440
DELRIN®	3.2	0.35	1.42	73
977-3 epoxy resin	3.8	0.3	1.29	186

The radius of the indenting spheres was taken as the radius of the tool steel tup insert, 0.01588 m. As this analysis intended to illustrate the differences in contact pressure of the materials, the force was selected as 1 N.

From equations (3.2) and (3.4), for a tool steel sphere in contact with a 977-3 epoxy resin half-space the contact radius and maximum pressure were found to be 0.143 mm and 23.45 MPa, respectively. Similarly, for a DELRIN® sphere in contact with a 977-3 epoxy resin half-space, the contact radius and pressure were found to be 0.183 mm and 14.27 MPa, respectively.

These maximum contact pressure results demonstrate that, for all other parameters constant, Hertzian contact analysis predicts that the tool steel tup insert would generate higher contact pressure than the DELRIN® tup insert. As higher contact pressure would produce larger amounts of damage, a steel impactor will produce more damage than a DELRIN impactor.

In this case, for a rigid flat-ended cylinder of radius 0.01588 m and a force of 1 N in contact with a half-space, the contact pressure found from formula (3.6) is 1.893 kPa. This contact pressure at the center of the contact region is significantly less than the contact pressure developed by a hemispherical impactor. While the normal stress distribution for a flat-ended cylinder does increase towards the edge of the contact region, the stress is still orders of magnitude less than that produced by a hemispherical impactor.

To compare the effect of the indenter shape, it is now assumed that a rigid impactor (spherical or flat-ended cylindrical) indents an elastic half-space. In the case of contact of a rigid sphere with an elastic half-space, the contact radius can be obtained from formula (3.2):

$$a = \left( \frac{3Fr}{4} \frac{1 - \nu^2}{E} \right)^{1/3} \quad (3.7)$$

and maximum contact pressure and contact stress distribution follow (3.3) and (3.4). In the case of contact of a rigid flat-ended cylindrical punch with an elastic half-space, the contact stress distribution follows (3.5) and contact pressure  $p_0$  can be found from (3.6).

The normal stress distributions, calculated from equations (3.3) and (3.5), for rigid hemispherical and flat-ended impactors with radius 0.01588 m and 1 N applied force in contact with an elastic 977-3 epoxy resin half space can be seen in Figure 3.43 and Figure 3.44, respectively. Note that, as previously discussed, the stress distribution for the hemispherical impactor is parabolic with the maximum stress at the center of the contact zone. Conversely, the stress distribution for the flat-ended impactor is minimum at the center, with stress singularities along the edge of the contact zone.

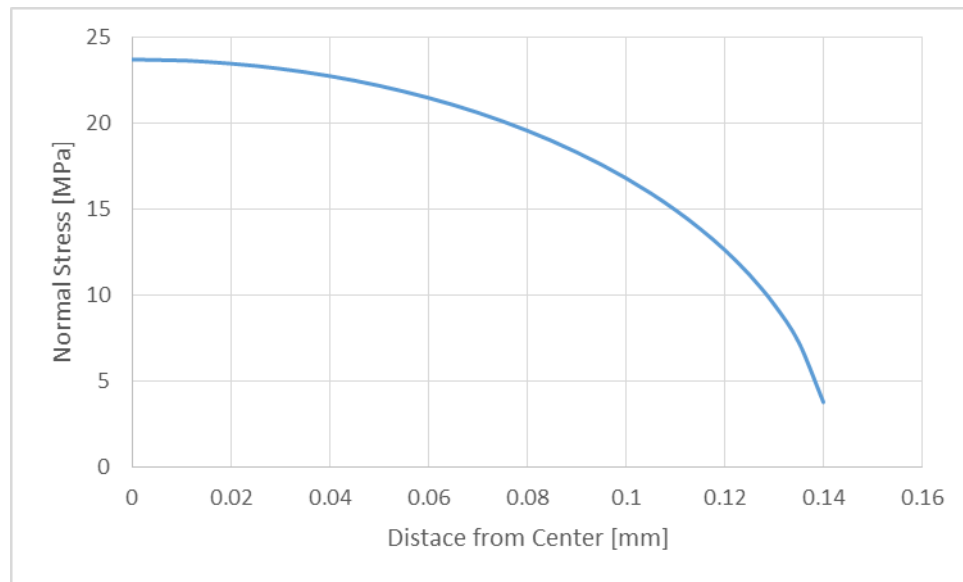


Figure 3.43: Contact Stress for Rigid Steel Hemisphere on 977-3 Half-Space

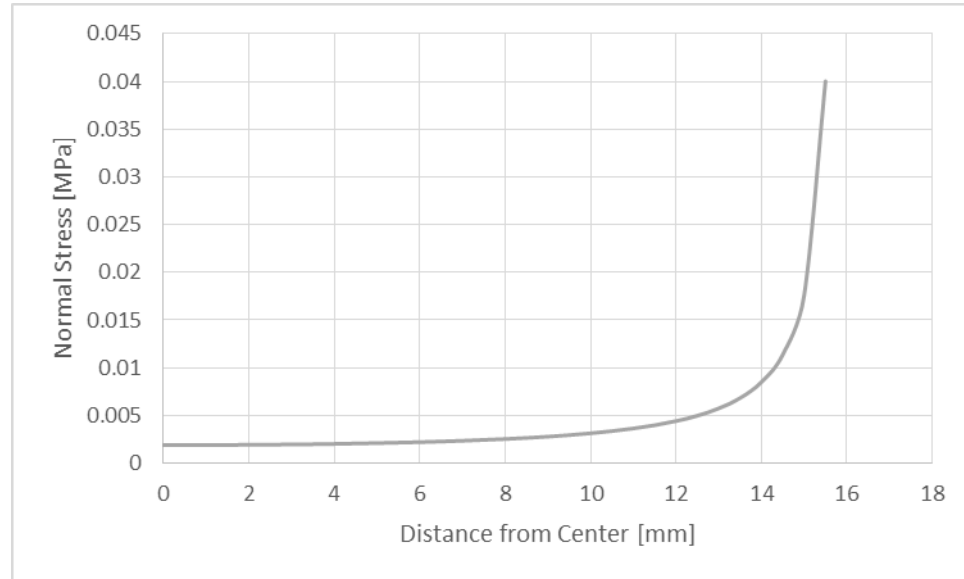


Figure 3.44: Contact Stress for Flat-Ended DELRIN® Cylinder on 977-3 Half-Space

### 3.5 Summary of Low Velocity Impact Experimental Results

The goal of the impact characterization was to determine the parameters for a low-velocity impact that would produce damage that was barely visible on the surface of 32-ply symmetric cross-ply carbon fiber reinforced polymer plates. To determine the parameters, three specimens, numbered 1, 2, and 3, were impacted at various energies. The initial impact energy was selected based on the previous work by Hart (2011). Because of the difference in tup insert material and geometry (tool steel hemisphere in the present work, DELRIN® flat-ended cylinder in the work of Hart), the per-ply energy Hart used to produce barely visible damage in 16-ply cross-ply plates produced

significant damage in specimen 1. By decreasing the impact energy to 20.77 J, barely visible damage was produced in specimen 3. Specimens 4 and 5 also were impacted at this energy.

To produce a set of specimens for comparison, an intermediate impact energy was selected between that used for specimens 2 and 3. This impact energy, 29.25 J, produced slight damage in specimens 6, 7, and 8.

To investigate the effect of impactor geometry and material, a second set of specimens were impacted at 29.25 J. For this set, the tup insert used was the same as that used by Hart (2011) and was a flat-ended cylinder milled from DELRIN®. This impact energy and tup insert produced no visible damage in specimens 9, 10, and 11. This resulting decrease in damage was consistent with the theoretical analysis of the contact stresses. A simple Hertzian analysis predicted that the stresses produced from the stiffer tool steel hemispherical tup insert would be greater than those produced from the resin cylinder for the same impact energy.

## CHAPTER 4

### COMPUTED TOMOGRAPHY IMAGE PROCESSING

#### 4.1 Image Processing Methodology

As discussed previously, impact damage to cross-ply composite plates was investigated using the Zeiss METROTOM 1500 computed tomography (CT) system. The METROTOM 1500 is an industrial CT scanning system, and the generated CT images were reconstructed using VGStudio MAX.

Image processing was performed using MyVGL 2.2, a CT scan analysis program designed to work with the output of VGStudio MAX. To use MyVGL, the raw output files from the METROTOM 1500 were opened and saved using VGStudio MAX, and the resulting project files were then processed in MyVGL. These files contained a greyscale set of images representing the reconstructed 3D object. The intensity of the grey-values corresponded to the amount of x-ray absorption for that region, with black as no absorption (corresponding to open air) and white as complete x-ray absorption.

The image processing procedure was as follows: The sample was imported into MyVGL 2.2 and the project file was opened. Then, areas within the grey-value distribution were selected so as to isolate the damaged region. An example of this can be seen in Figure 4.1. The darkest region (labeled as Interval 1) corresponded to open air and the support material, and thus were discarded from the analysis. The lightest region (labeled as Interval 4) were sections of the specimen where no damaged occurred. Between these two regions were grey-values corresponding to damage within the plate

and undamaged sections of the plate not perpendicular to the scan, as discussed below. To provide contrast between damaged and undamaged sections of the specimen, the undamaged areas were colored blue and the damaged areas were colored yellow.

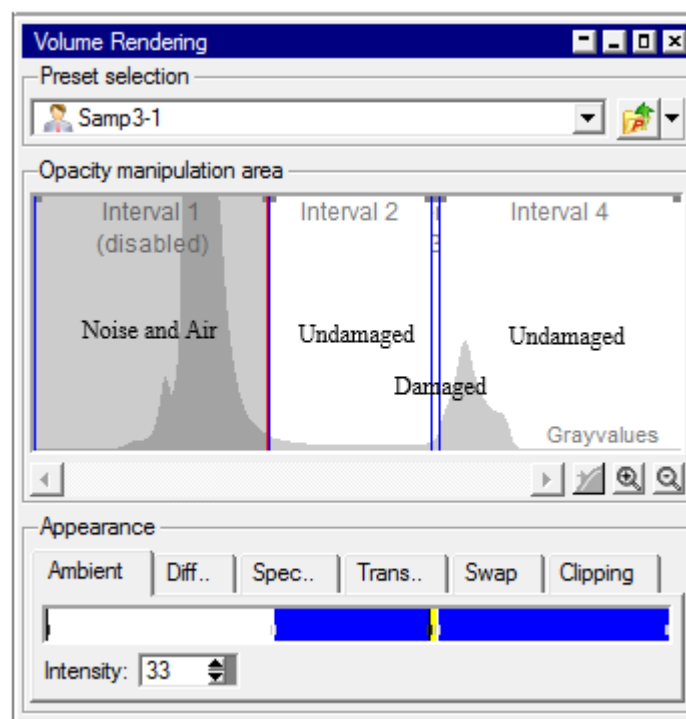


Figure 4.1: Example Gray-Values Setting for Isolating Damage in MyVGL

After the grey-value regions were set for each specimen, an image stack of the in-plane view of the plates was generated. This view best represented the extent of the damaged area in each specimen, and analysis of damage in this view was consistent with

the previous work and literature. One image per CT scan slice was generated through the entire thickness of each specimen.

To obtain numerical data on the damaged region, the colorized images were then processed. MyVGL had some basic built-in measurement features, including a point-to-point distance measurement tool. This tool was used to measure the maximum length of the damaged region in each slice, as indicated by the extent of the yellow area.

The damaged area and volume were of interest in this investigation, but no area or volume measurement tool was available within MyVGL. Therefore, to measure the damaged area a MATLAB image processing program was developed. The program read in the exported images, segmented each image by color into three regions (background/white, undamaged/blue, and damaged/yellow), and then reported the number of pixels for each region. Because the images were at 100 % scale to the CT scan, the resulting number of pixels could be multiplied by the resolution of the image to determine the damaged area. Then, the damaged area could be multiplied by the thickness of the image slice to obtain the damaged volume. Details of the MATLAB program are included in the Appendix.

The resolution of the CT scans for full-sized specimens impacted with the tool steel tup insert (specimens 3 through 8) was 0.180213 mm/px in each orthogonal direction (therefore, each voxel in the CT scan had a volume of  $0.180213^3 \text{ mm}^3$ , or  $0.0058527 \text{ mm}^3$ ). The approximate ply thickness was determined by dividing the plate thickness by the number of plies. For the specimens considered in this investigation, the ply thickness was approximately 0.13969 mm. Because the ply thickness was smaller than the image resolution, each image through the thickness of the plate captured more

than one ply. This meant that the ply interfaces were not uniquely captured in the CT scan at this resolution, and so the damaged area at the ply interfaces could not be individually identified. Further, the relatively low resolution of the CT scan produced a significant amount of noise, contributing to the difficulty in isolating the damaged areas. In addition, the specimens were not perfectly perpendicular to the x-ray sensor, and so the plies do not lie flat to the images. The misalignment was within 1 mm, and due to the setup of the CT scanner cannot be effectively corrected. The images being non-perpendicular lead to several undesirable outcomes. First, this caused the through-thickness direction measurements to not be accurate. The “depth” into the plate of each image was measured from the first image where the plate appeared, which was often only one corner. Because of this skew, the thickness of the plates as measured from the image stack is larger than the true thickness of the plates. Adjusted depth measurements were taken for critical values, but the skew still contributes to some error in these measurements. Therefore, for this analysis, measurements taken that adjust for skew will be referred to as “depth” measurements, while measurements relative to the first image slice will be referred to as “relative depth” measurements. The other result of non-perpendicular scans was a gradient along some of the images. While the scan slices that fully capture the interior of the specimen were unaffected, slices that included a face boundary had an additional gradient line. This line, seen in Figure 4.2, was part of the damaged zone grey-values despite not correlating to actual damage. Because of this, damaged area measurements for slices containing the plate faces overestimate the true damaged area. Despite these issues, image analysis using these scans can provide general information on the range and extent of the internal damage.

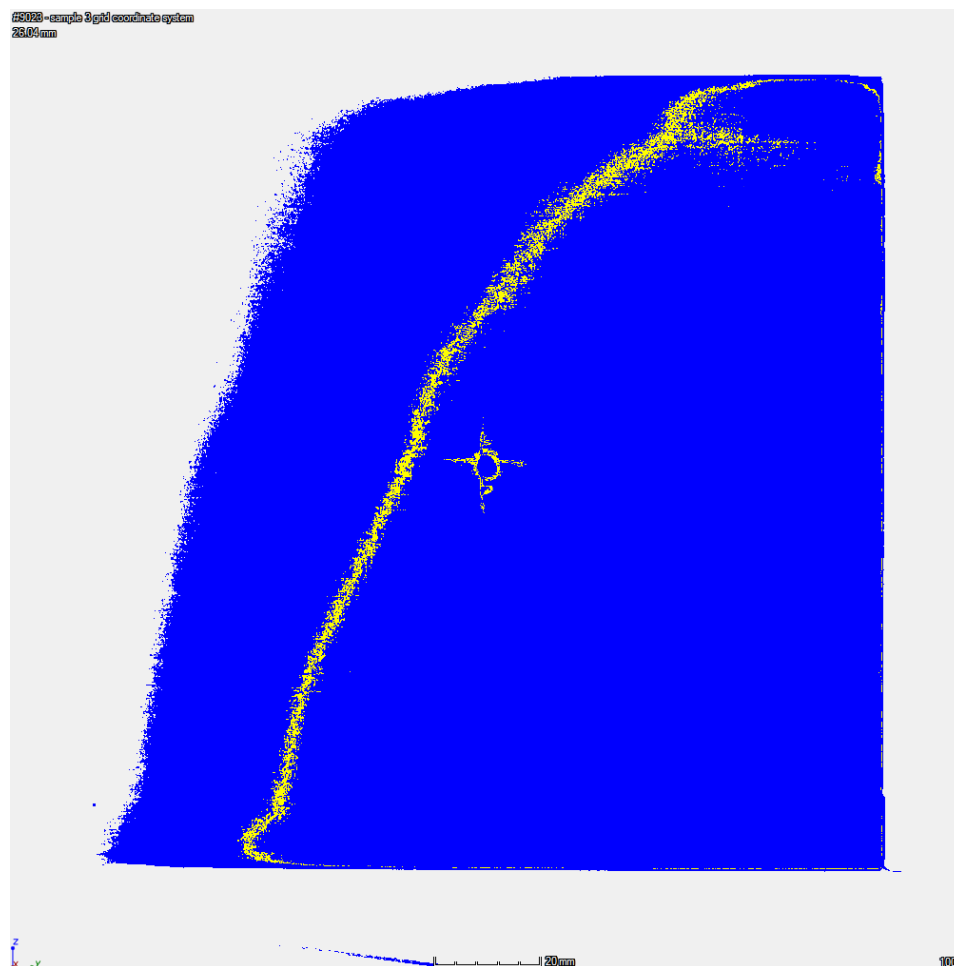


Figure 4.2: Example of Gradient Line in Image 7 (Depth of 1.08 mm) of Specimen 3

## 4.2 Specimen Cut Sizing

In addition to damage zone measurements, a bounding region for the damaged zone was also investigated during the preliminary image processing. Using the greyscale CT scan output, measurements of the length, width, and distance from the edge of the apparent damaged region were taken using Image J (Fiji), an open-source CT scan viewer. From those measurements, the approximate damaged zone size and center were determined. While the damaged zone for each specimen would fit within a 40 mm by 40 mm square region, the center of each cut would need to be located individually. If a uniform specimen cut location was desired, it was determined that a 45 mm by 45 mm region located about the center of each plate would entirely capture the internal damage zone. However, this would not capture the visible back face damage. To achieve the best balance of increased resolution and encapsulating the entirety of the damage, other cut specimen geometries were considered. After consulting with the CT imaging technician, it was concluded that square specimens would provide the best results. Circular specimens were proposed in order to increase scan resolution, but were thought to be too difficult to consistently secure in the CT scanning fixture. Rectangular specimens were also considered so as to capture the back face damage, and while no major objections were raised it was still thought that a more compact specimen size would be best for achieving the highest resolution.

To achieve a balance of image resolution and damaged area capture, a 45 mm by 45 mm specimen size was selected. The specimens were cut using a water-jet CNC cutter, and an example of the results can be seen in Figure 4.3. To facilitate removal from the cutting surface, small tabs were left on one edge of the cut specimen. While the

edge-surface quality of the cuts was generally excellent, there was a small amount of delamination induced near the start and stop of the cut path (located at the corner of the cut specimen, on the lower right in Figure 4.3). This delamination was a result of the crossing toolpath, and the induced damage for Specimen 3 is highlighted in the boxed region of Figure 4.4. A more detailed analysis of the cutting-induced damage is provided in a later section.

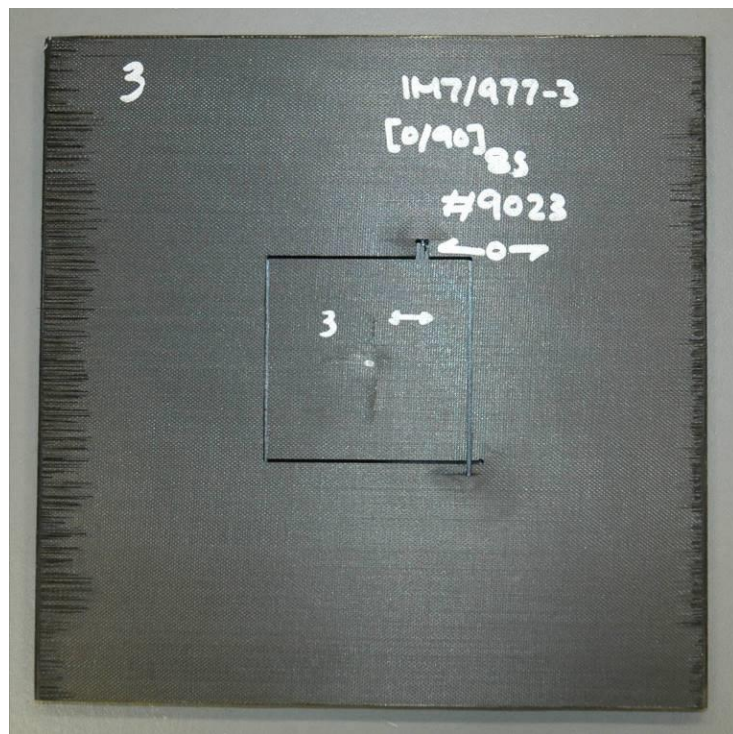


Figure 4.3: Cut Specimen 3 within Original Plate



Figure 4.4: Corner Delamination in Side View of Cut Specimen 3

### 4.3 CT Image Processing Results

#### 4.3.1 Specimen 3

Specimen 3 had been impacted at an energy of 20.77 J. The whole-plate CT scan for specimen 3 had a resolution of 0.1802 mm/px and produced a stack of 36 images through the thickness of the plate. From these images it was determined that the scan through the thickness had a total unadjusted depth of 5.95 mm. The maximum damage length was found to be 29.73 mm at a depth of 2.58 mm (3.24 mm relative depth in the image stack), as seen in Figure 4.5. From image processing on the entire plate, it was found that the maximum internal damaged area occurred at a depth of approximately 2.48 mm (3.06 mm relative depth) from the impacted surface and was measured to be 1040.9 mm<sup>2</sup>, shown in Figure 4.6. The global 0° fiber orientation is indicated by the black arrow above the specimens, and the damaged area is boxed in both figures. From the damaged area for this slice, the maximum damaged volume per slice was 187.6 mm<sup>3</sup>. The total

damaged volume for specimen 3 was found to be 2097.0 mm<sup>3</sup>, which was approximately 0.359 % of the total volume of the plate.

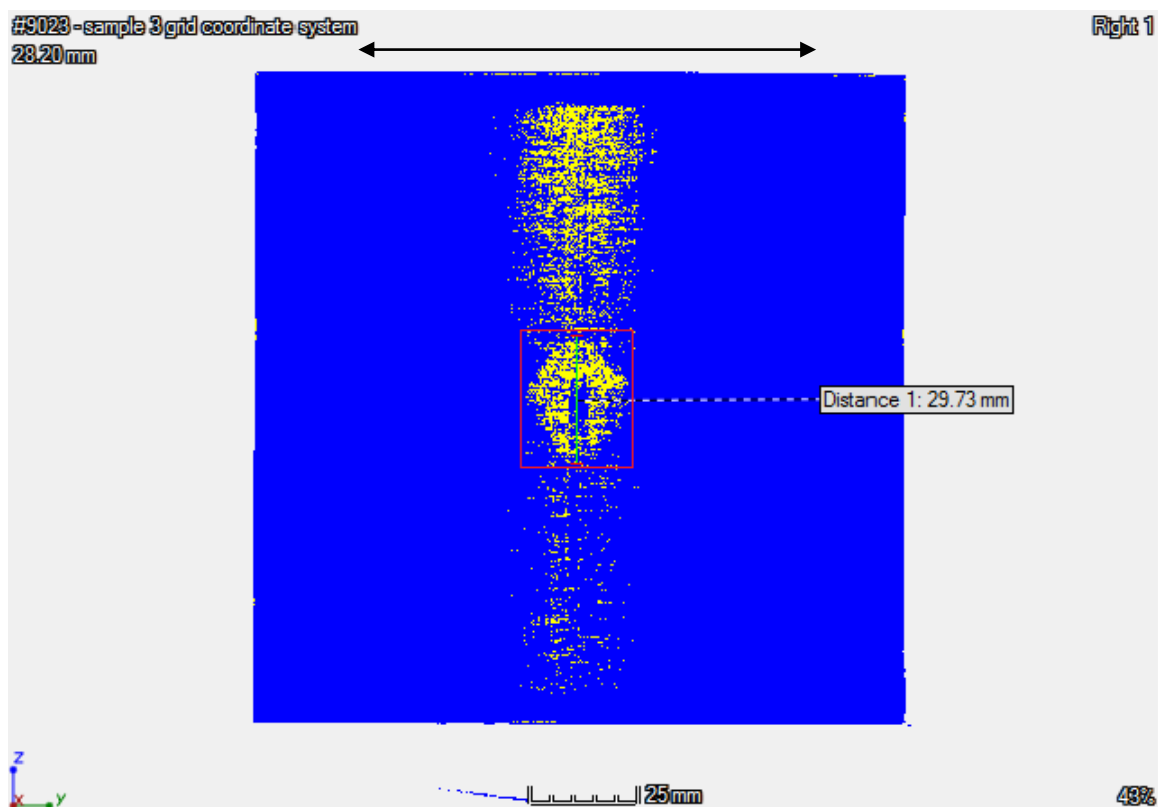


Figure 4.5: Length of Largest Internal Damage for Specimen 3 (Depth of 2.58 mm)

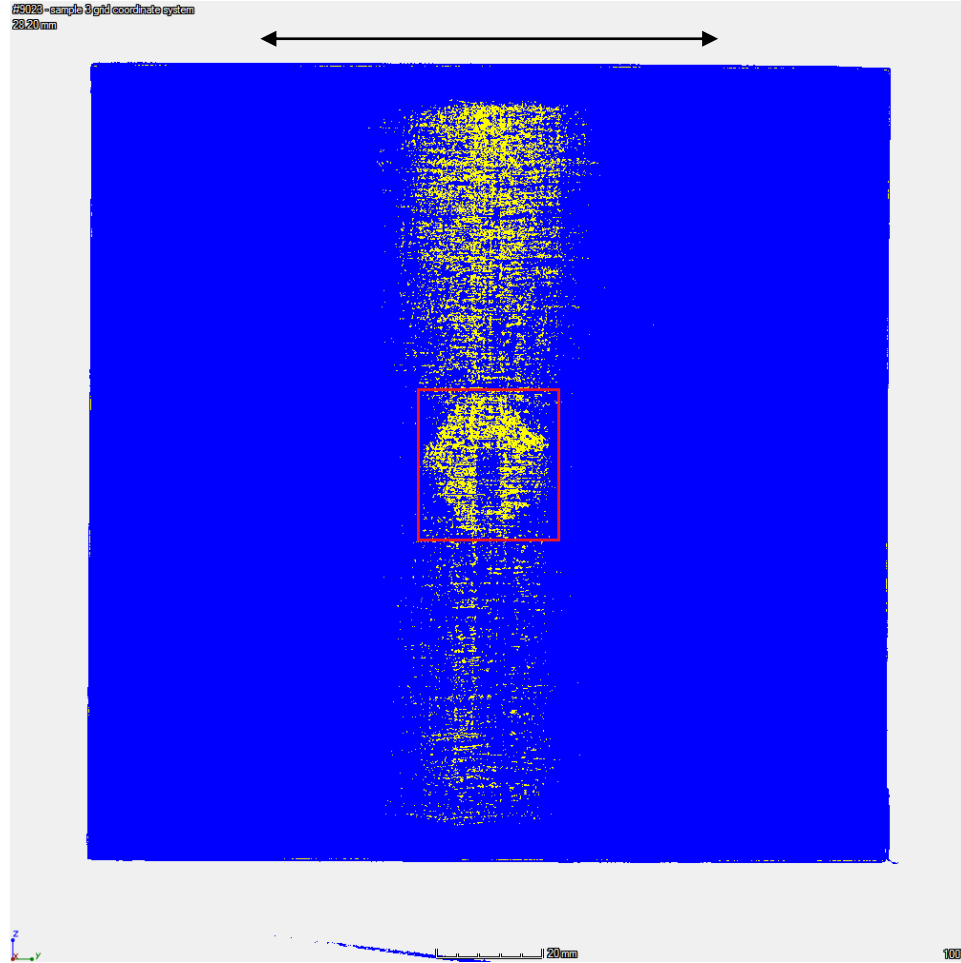


Figure 4.6: Segment with Largest Damaged Area for Specimen 3 (Depth of 2.48 mm)

After cutting of the central region, specimen 3 was processed again. This CT imaging produced a stack of 87 images through the thickness of the plate at a resolution of 0.0588 mm/px. From these images it was determined that the scan had a total relative depth of 4.95 mm and a total measured depth of 4.32 mm. The maximum horizontal ( $0^\circ$  orientation) damage length was found to be 28.92 mm at a depth of 3.61 mm (3.83 mm

relative depth, within the 28<sup>th</sup> ply from the top) and the maximum vertical (90° orientation) damage length was found to be 29.85 mm at a depth of 3.43 mm (3.65 mm relative depth, at the interface between the 26<sup>th</sup> and 27<sup>th</sup> plies). From image processing of the cut plate, it was found that the maximum internal damaged area occurred at a depth of 1.80 mm (2.24 mm relative depth) from the impacted surface and was measured to be 132.5 mm<sup>2</sup>, shown in Figure 4.7. This CT slice occurred within the 16<sup>th</sup> ply from the top, which was the first of the two symmetric 90° fiber orientation plies. In the figure, the black arrow above the plate indicates the global 0° fiber direction, while the red arrow indicates the ply orientation. From the damaged area for this slice, the maximum damaged volume per slice was 7.79 mm<sup>3</sup>. The total damaged volume for cut specimen 3 was found to be 868.5 mm<sup>3</sup>, which was approximately 0.149 % of the total volume of the original plate. This percent volume for the damaged region was calculated using the total volume originally calculated for the uncut specimen and the damaged volume found from analysis of the cut specimen. This allows for direct numerical comparison of the percent damaged volume from the full-sized and cut specimens (presented in a later section). For this specimen, the cutting process induced additional delamination in the lower right corner as seen in Figure 4.7.

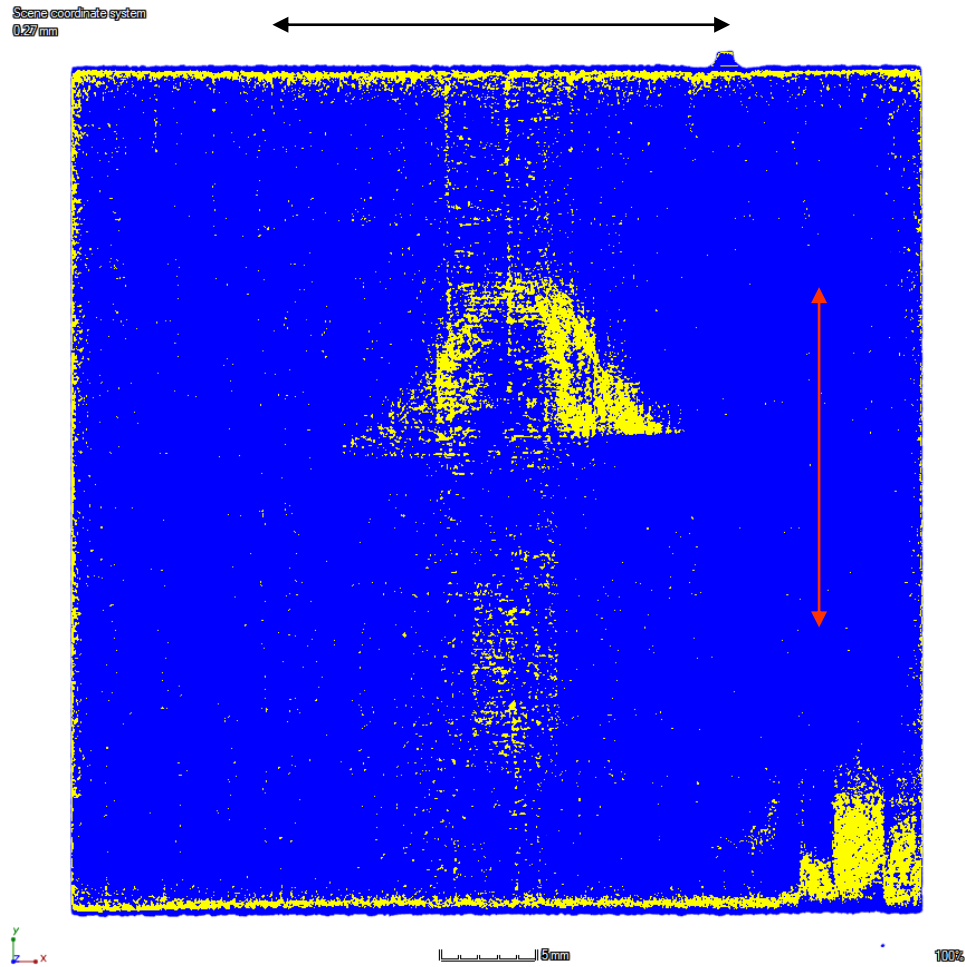


Figure 4.7: Segment with Largest Damaged Area for Cut Specimen 3 (Depth of 1.80 mm, Within Ply 16)

To obtain an even more accurate estimate of the damaged volume, the delamination in the corner induced by the water-jet cutting of the specimen was isolated. It was found that the damage to the corner had a volume of  $93.4 \text{ mm}^3$ . After removing this induced damage from the total damaged volume measured on the cut plate, the adjusted damaged volume was found to be  $775.2 \text{ mm}^3$ , which was 0.1329 % of the total

volume of the original plate. Isolating and removing the cutting-induced damage resulted in a 10.8 % reduction in total damaged volume for specimen 3.

On each of the CT scan images for specimen 3, the maximum damage length in the horizontal ( $0^\circ$ ) direction and vertical ( $90^\circ$ ) direction were measured. A plot of these lengths at the ply interfaces can be seen in Figure 4.8 and Figure 4.9 for the  $0^\circ$  and  $90^\circ$  orientations, respectively. For these figures, the top-most lines correspond to the measurements from the ply interfaces nearest the impacted surface of the plate. While the maximum damage length measurement did not always occur on the same centerline, for illustration purposes the measurements have been centered within the figures.

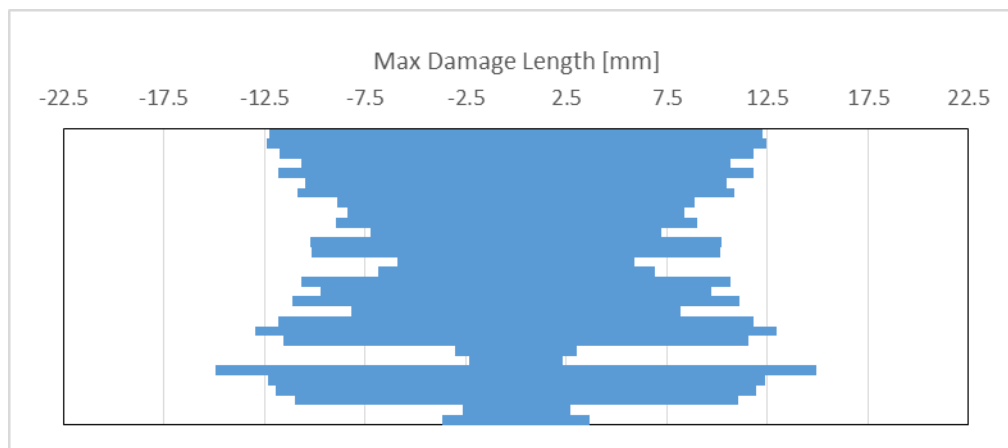


Figure 4.8: Maximum Damage Length in the  $0^\circ$  Direction for Specimen 3

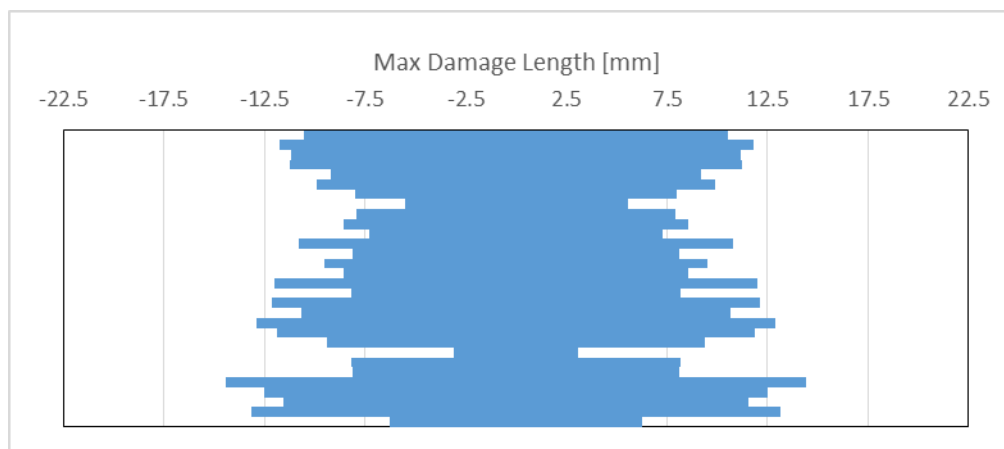


Figure 4.9: Maximum Damage Length in the 90° Direction for Specimen 3

While Figure 4.8 and Figure 4.9 do not appear to provide any meaningful quantitative relationship between the maximum length of damage and the depth into the plate, when combined with qualitative analysis a pattern can be generally seen. When taking the measurements of maximum damage length, it was noticed that two different damage modes dominated the measurements. For the top portion of the plate, the maximum damage length was dominated by cracks caused by the impact. These cracks correspond to the visible surface cracks, indicated by the red arrows on the top face of specimen 3 in Figure 4.10, and go through several of the top layer images. These transverse cracks were oriented perpendicular to the plane of the plate and were primarily matrix cracks across the first few layers extending away from the impacted surface. The second damage mode, predominately seen in the lower plies, was delamination. This delamination, which was characterized by cracking and separation of adjacent plies in the plane of the plate, followed the expected pattern of increasing in length as the depth from

the impacted surface increased. This is illustrated in Figure 4.11 and Figure 4.12. The red lines in these figures indicate the general region where the maximum damage length was dominated by the surface cracks. The gold lines indicate the general shape of the delaminated damage as it became more prevalent than the surface cracking.

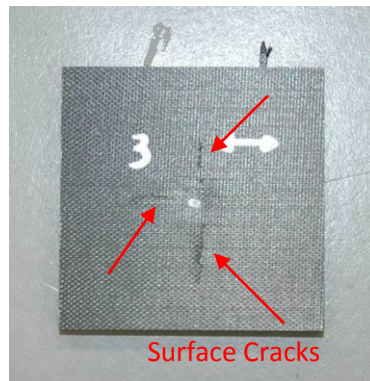


Figure 4.10: Cracks on Impacted Surface for Cut Specimen 3

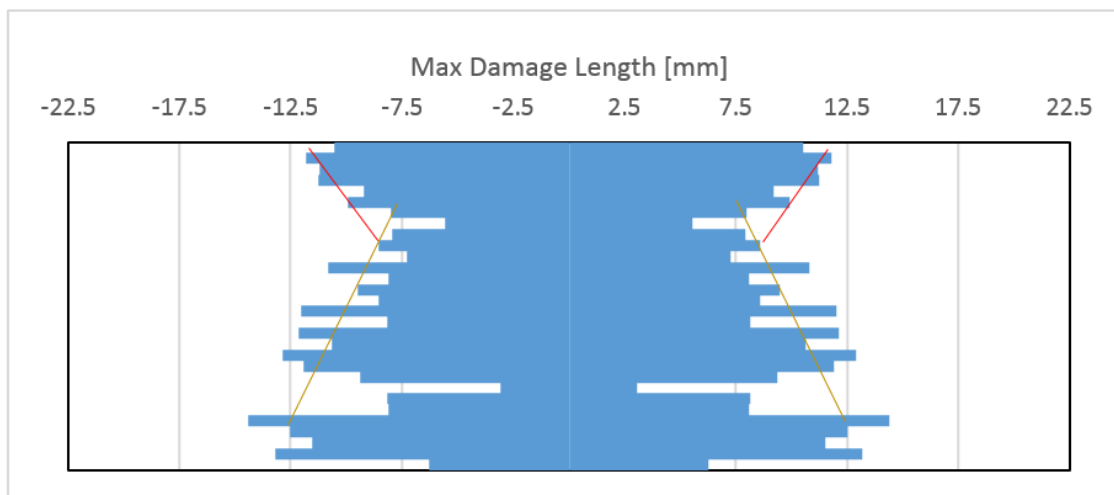


Figure 4.11: Annotated Max Damage Length in the 0° Direction for Specimen 3

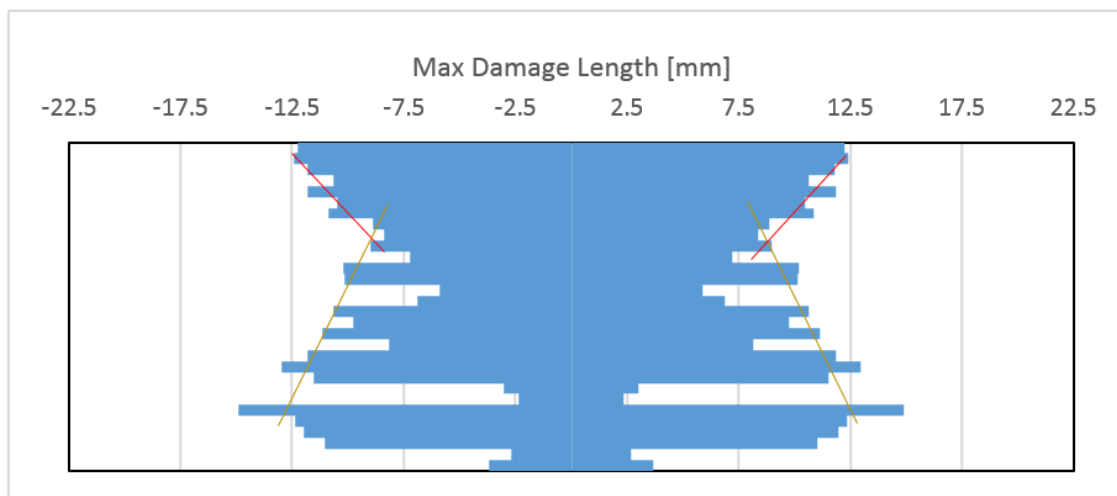


Figure 4.12: Annotated Max Damage Length in the 90° Direction for Specimen 3

From the images of the cut specimen, it was possible to identify the ply orientation of each slice. Further, as there were approximately 2.5 CT slices per ply, images along the ply interface could usually be selected. The 30 different-direction ply interfaces from specimen 3 can be seen in Figure 4.13. The black arrow near the first image indicates the global  $0^\circ$  fiber direction. The first image is at the interface between the top,  $0^\circ$  orientation ply and the second,  $90^\circ$  orientation ply. The pattern continues from there. No ply interface image was included for the central interface between the middle  $90^\circ$  plies. As can be seen from this figure, the damage at the ply interfaces is typically in the orientation of the lower ply, as is expected for unidirectional angle-ply composites. Note that the significant amount of pixels coded as damage near the front and back surfaces (first and last images in Figure 4.13) are a product of surface effects and the threshold used, and so do not accurately reflect damage on these interfaces.

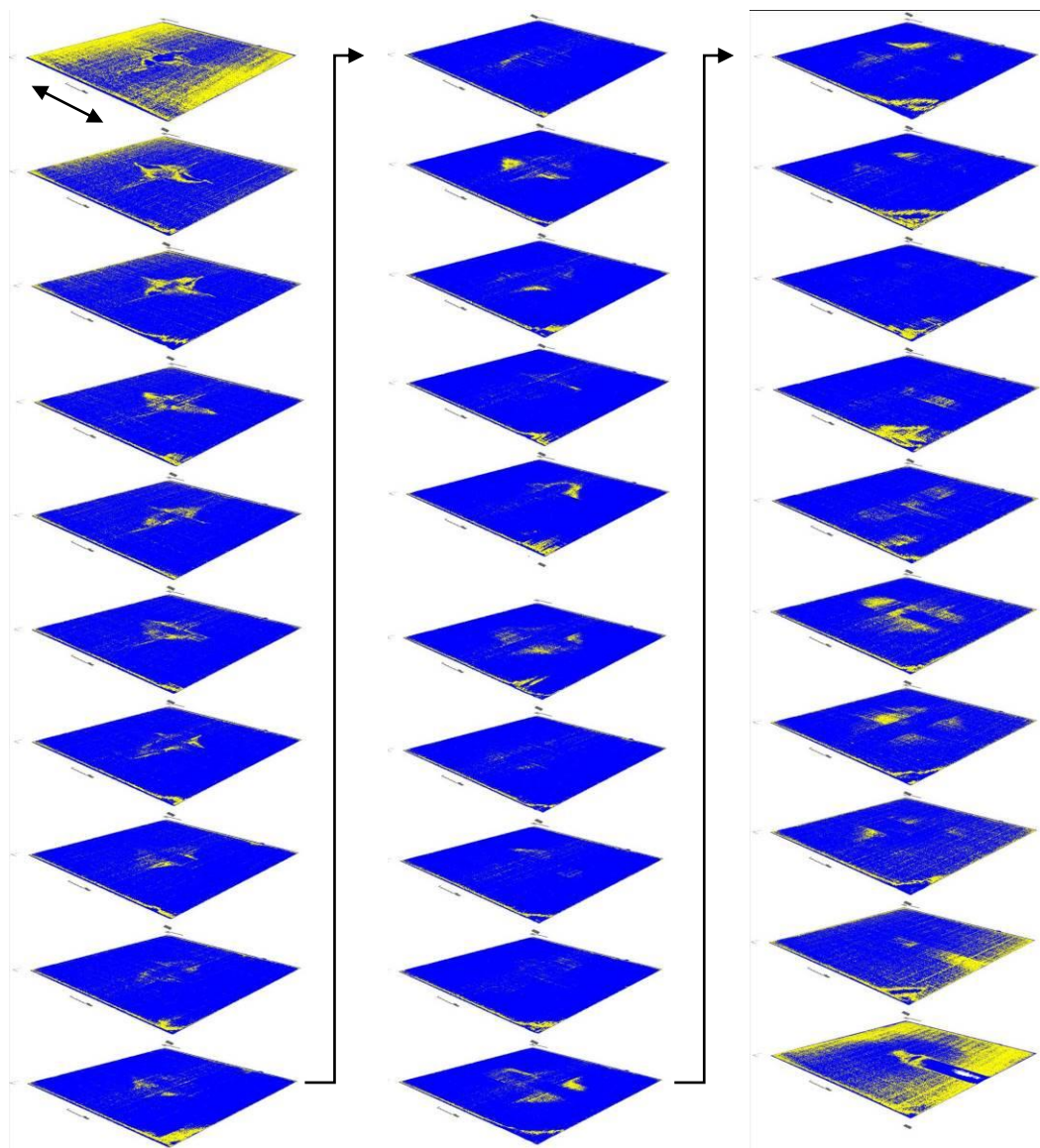


Figure 4.13: Ply Interfaces from Specimen 3

Examining each ply interface in turn presents insight into the overall damage in specimen 3. For the first ply interface, between the top  $0^\circ$  direction ply and the next  $90^\circ$  direction ply, most of the indicated damage comes from edge effects and the damage

isolation threshold, as previously mentioned. A “+” shaped damage zone can be seen in the center of the plate, and this damage matches with the visible surface damage of specimen 3. The next interface has reduced noise, but the “+” shaped damage from the impacted surface remains. The damage at this interface is greater in the 0° direction (24.84 mm maximum damage length for 0° direction as compared to 23.56 mm maximum damage length in the 90° direction), which follows with the expected result that damage extends in the direction of the lower ply. The damage generally follows this conclusion for the next five ply interfaces as well, with damage extending more prominently in the direction of the lower ply. At the ninth ply interface from the impacted surface (90° upper ply, 0° lower ply), the damaged region becomes less distinct as the effect of the surface cracks on overall damage decreases. While the damage still tends to be greater in the direction of the lower ply, the overall damaged region starts to lose the consistent shape it had generally followed. In particular, ply interfaces 11 through 15 (first five images in column two of Figure 4.13) have notable asymmetry, with a greater amount of damage on one half or in one quadrant of the ply interface. After the symmetric ply boundary, starting with interface 16, the damage tends to take on an inverted “+” shape, with damage in the four quadrants around the horizontal and vertical centerlines. Delamination in the corner from water-jet cutting also becomes more severe on the lower plies, most notably at interface 24. Also starting at interface 24 are clear damage effects from the back face damage. Specimen 3 had a noticeable raised damage area on the back face oriented in the 0° direction, and the ply interfaces with a lower ply along that direction tend to reflect this damage in particular. This damage is visible in interface 29, an interface with a 90° orientation lower ply, as the physically

raised damage likely distorted this ply directly. Due to the threshold used, the physically raised area was coded as not damaged in the final ply interface. The final ply interface, like the first, also had edge-effect noise.

#### 4.3.2 Specimen 4

Specimen 4 had also been impacted at an energy of 20.77 J. The CT scan resolution for specimen 4 was 0.1802 mm/px and produced a stack of 38 images through the thickness of the plate. From image processing, it was found that the scan through the thickness had a total unadjusted depth of 6.31 mm. The maximum damaged length was found to be 24.62 mm at a depth of 2.67 mm (relative depth of 3.24 mm), shown in Figure 4.14. The maximum internal damaged area occurred at a depth of 2.40 mm (relative depth of 3.06 mm) from the impacted surface as was measured to be 226.1 mm<sup>2</sup>. The colorized CT scan slice with the largest damaged area can be seen in Figure 4.15. The damaged area is boxed in both figures, and the global 0° fiber orientation is indicated by the black arrow above the specimen. From the damaged area for this slice, the maximum damaged volume per slice was 40.7 mm<sup>3</sup>. The total damaged volume for specimen 4 was found to be 1331.5 mm<sup>3</sup>, which was approximately 0.214 % of the total volume.

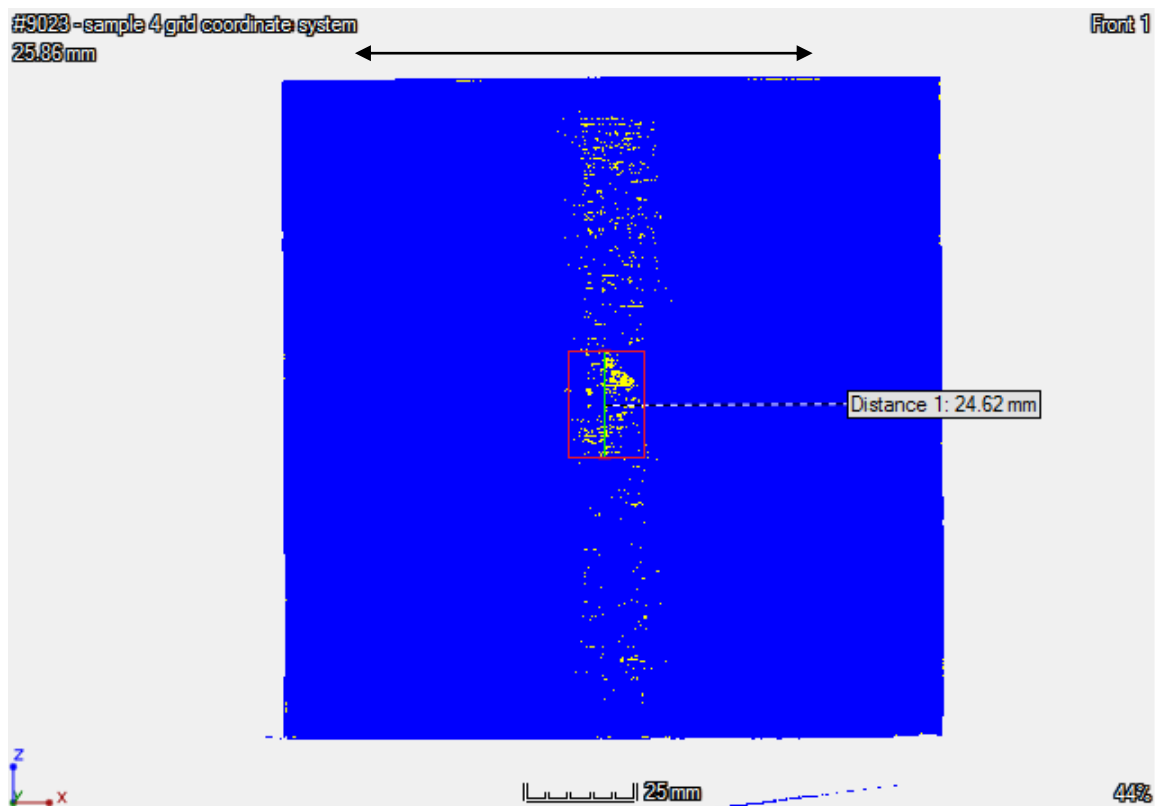


Figure 4.14: Length of Largest Internal Damage for Specimen 4 (Depth of 2.67 mm)

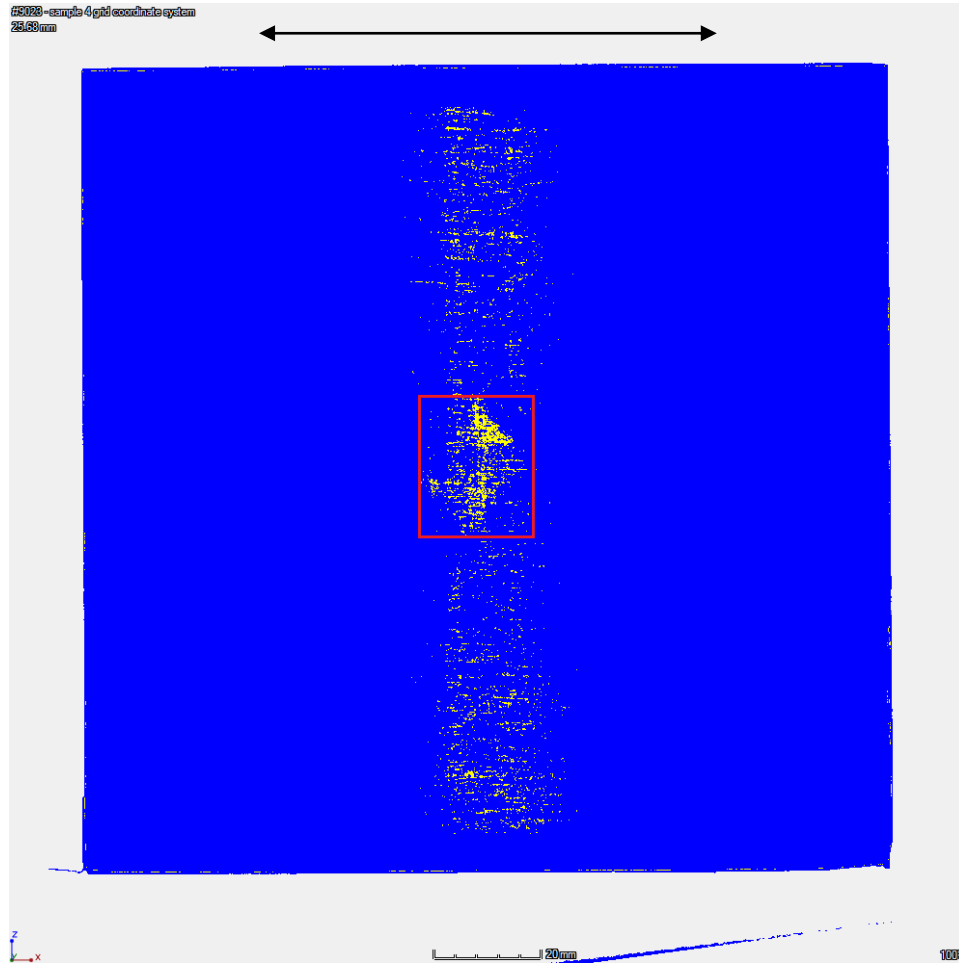


Figure 4.15: Segment with Largest Damaged Area for Specimen 4 (Depth of 2.40 mm)

After cutting out the central damaged region, specimen 4 was processed again. This produced a stack of 90 images through the thickness of the plate at a resolution of 0.0588 mm/px. From these images it was determined that the scan had a total relative depth of 5.12 mm and a central measured depth of 4.34 mm. The maximum horizontal ( $0^\circ$  orientation) damage length was found to be 28.28 mm at a depth of 3.54 mm (4.00 mm relative depth) and the maximum vertical ( $90^\circ$  orientation) damage length was found

to be 28.03 mm at a depth of 0.13 mm (0.59 mm relative depth). From image processing of the small plate, it was found that the maximum internal damaged area occurred at a depth of 2.29 mm (2.77 mm relative depth) from the impacted surface and was measured to be 174.96 mm<sup>2</sup>, shown in Figure 4.16. In this figure, the black arrow above the plate indicates the global 0° fiber direction. From the damaged area for this slice, the maximum damaged volume per slice was 10.29 mm<sup>3</sup>. The total damaged volume for cut specimen 4 was found to be 539.2 mm<sup>3</sup>, which was approximately 0.087 % of the total volume of the original plate. For this specimen, the cutting process induced additional delamination in the upper left corner, as seen in Figure 4.16.

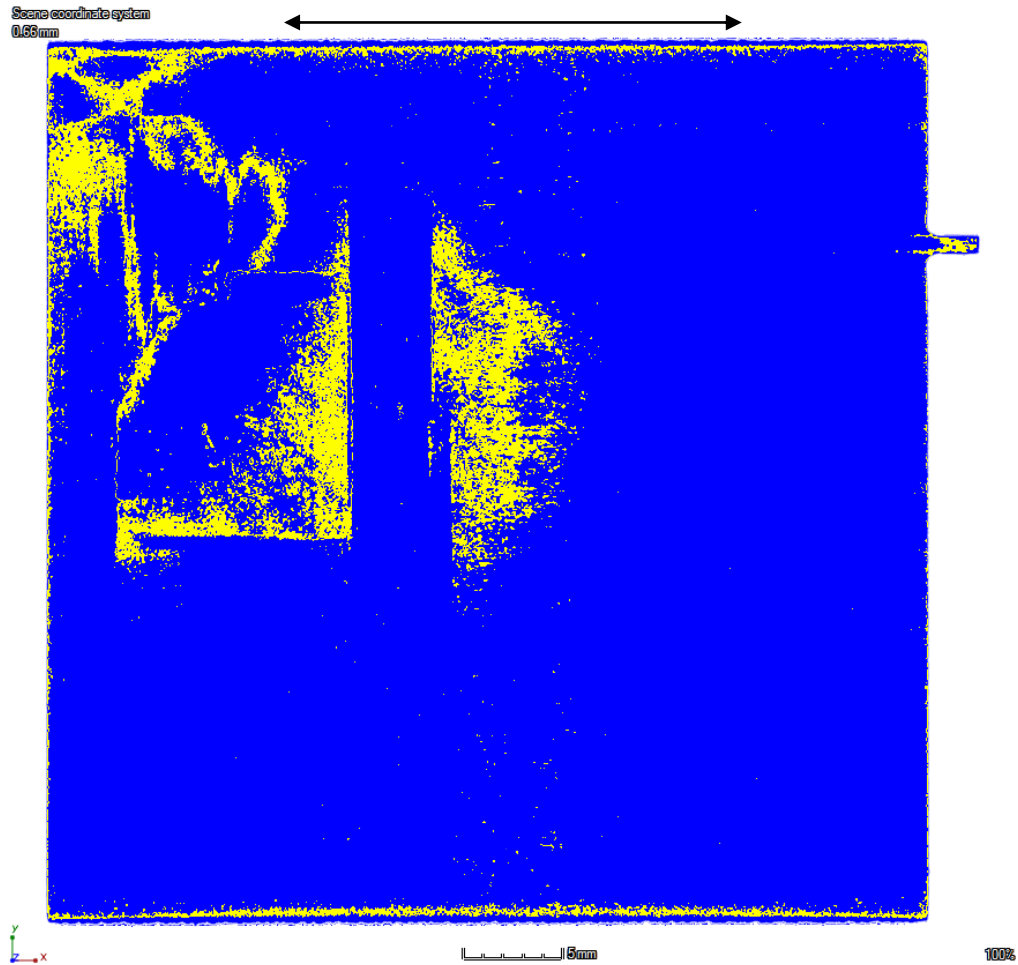


Figure 4.16: Segment with Largest Damaged Area for Cut Specimen 4 (Depth of 2.29 mm)

As with specimen 3, the damage induced by the water-jet cutting was isolated and measured. Because of the location of the impact damage relative to the damaged corner, particular care was needed to isolate the cutting damage. After processing it was found that the damage to the corner had a volume of  $96.2 \text{ mm}^3$ . After removing this damage, the adjusted total damaged volume for specimen 4 was found to be  $443.0 \text{ mm}^3$ , which

was 0.0712 % of the total volume of the original plate. This was a 17.8 % reduction in total damaged volume from removal of cutting-induced damage.

Unlike for specimen 3, analysis at the ply interfaces for specimen 4 could not be completed. During CT scanning, specimen 4 was held at a small angle relative to the imaging plane. This inclination was on the order of millimeters, but due to the high resolution of the scan resulted in each image cutting across multiple plies. Because of this the ply interfaces are not uniquely captured in the images, and so an interface-by-interface analysis was not able to be performed.

#### 4.3.3 Specimen 5

Specimen 5, as with specimens 3 and 4, had been impacted at an energy of 20.77 J. The CT scan for specimen 5 also had a resolution of 0.1802 mm/px and produced a stack of 31 images through the thickness of the plate. From these images it was determined that the scan had an unadjusted plate depth of 5.05 mm. The maximum damage length was found to be 26.79 mm, occurring at a depth of 2.49 mm (relative depth of 2.70 mm). This can be seen in Figure 4.17. From image processing it was found that the maximum internal damaged area occurred at a depth of 2.32 mm (relative depth of 2.52 mm) from the impacted surface. The maximum damaged area was measured to be 887.8 mm<sup>2</sup> and is shown in Figure 4.18. The black arrow above the figures indicates the global 0° fiber orientation, and the damaged area is boxed in both figures. From the damaged area for this slice, the maximum damaged volume per slice was 160.0 mm<sup>3</sup>, which was approximately 0.434 % of the total volume.

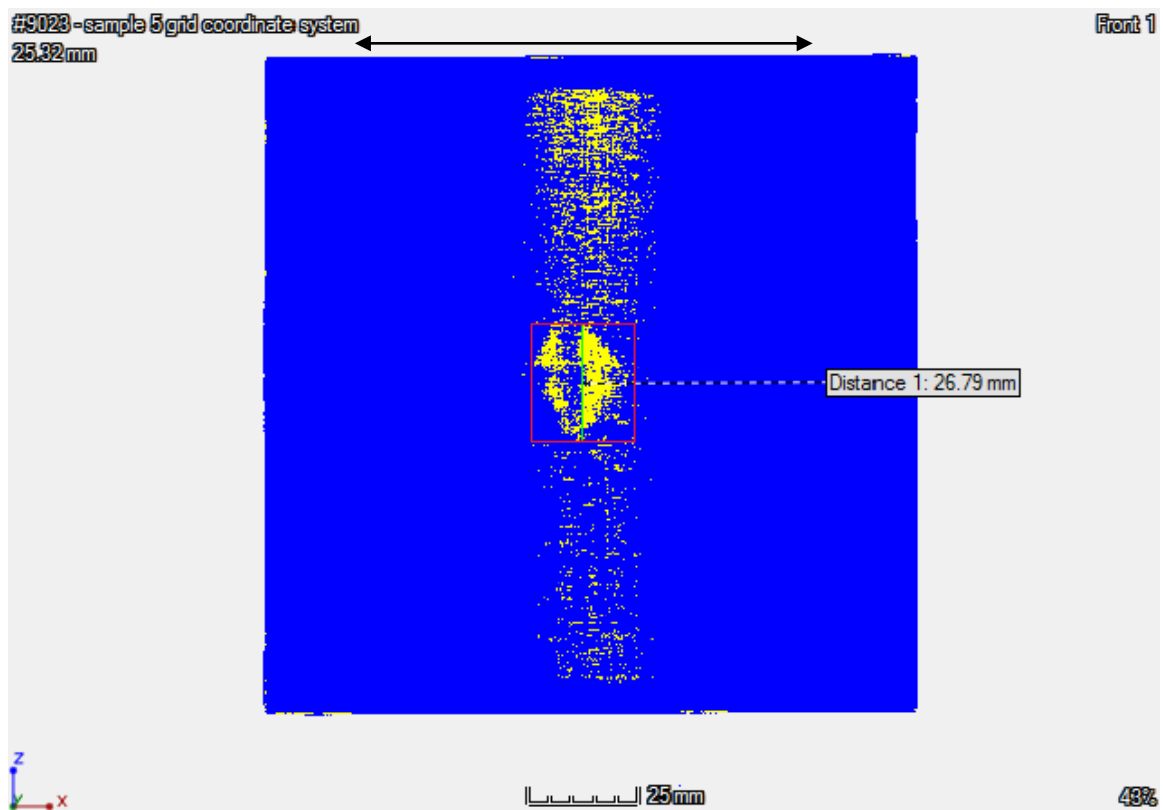


Figure 4.17: Length of Largest Internal Damage for Specimen 5 (Depth of 2.49 mm)

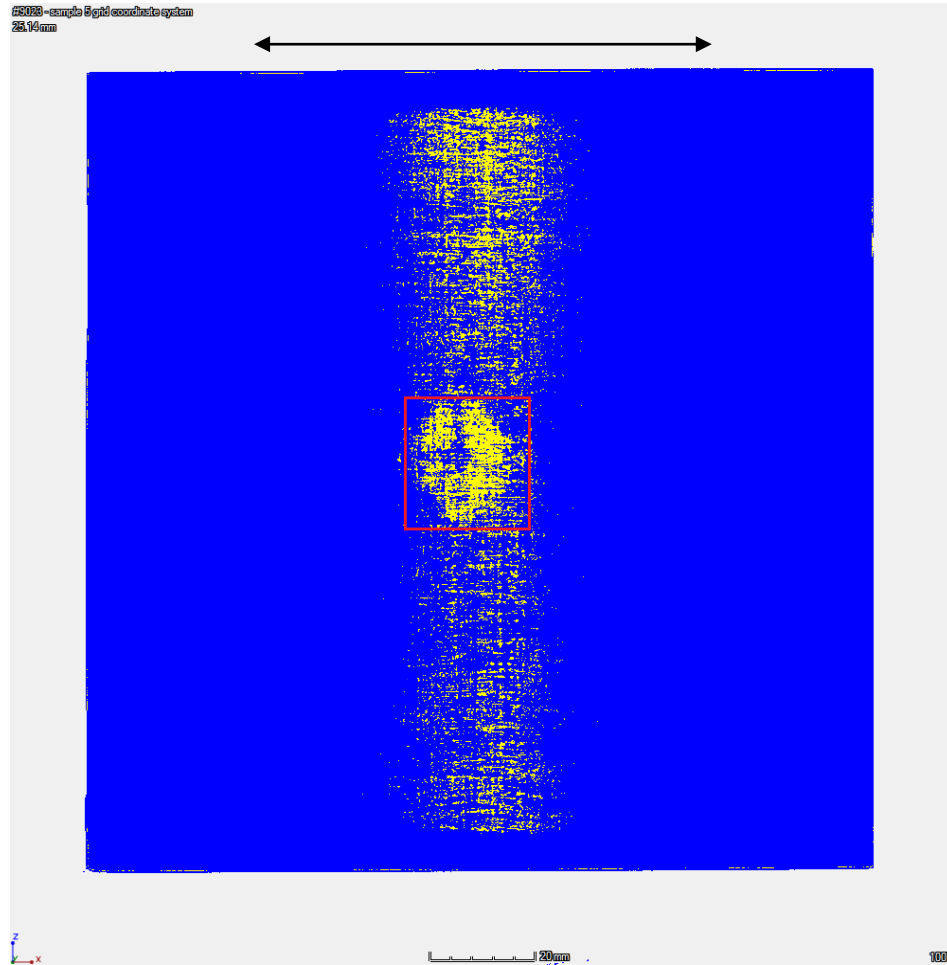


Figure 4.18: Segment with Largest Damaged Area for Specimen 5 (Depth of 2.32 mm)

After cutting of the central region, specimen 5 was processed again. This CT imaging produced a stack of 87 images through the thickness of the plate at a resolution of 0.0588 mm/px. From these images it was determined that the scan had a total relative depth of 4.94 mm and a total measured depth of 4.28 mm. The maximum horizontal ( $0^\circ$  orientation) damage length was found to be 29.54 mm at a depth of 3.63 mm (3.77 mm relative depth) and the maximum vertical ( $90^\circ$  orientation) damage length was found to

be 28.60 mm at a depth of 3.74 mm (3.94 mm relative depth, within the 28<sup>th</sup> ply). From image processing of the cut plate, it was found that the maximum internal damaged area occurred at a depth of 3.02 mm (3.24 mm relative depth, within the 29<sup>th</sup> ply) from the impacted surface and was measured to be 289.31 mm<sup>2</sup>, shown in Figure 4.19. This occurred at the interface between the 24<sup>th</sup> and 25<sup>th</sup> plies from the top surface. In this figure, the black arrow above the plate indicates the global 0° fiber direction. As this slice occurred at a ply interface, the red arrow indicates the fiber orientation of the lower ply. From the damaged area for this slice, the maximum damaged volume per slice was 17.01 mm<sup>3</sup>. The total damaged volume for cut specimen 5 was found to be 1141.1 mm<sup>3</sup>, which was approximately 0.206 % of the total volume of the original plate. For this specimen, the cutting process induced additional delamination in the upper left corner as seen in Figure 4.19.

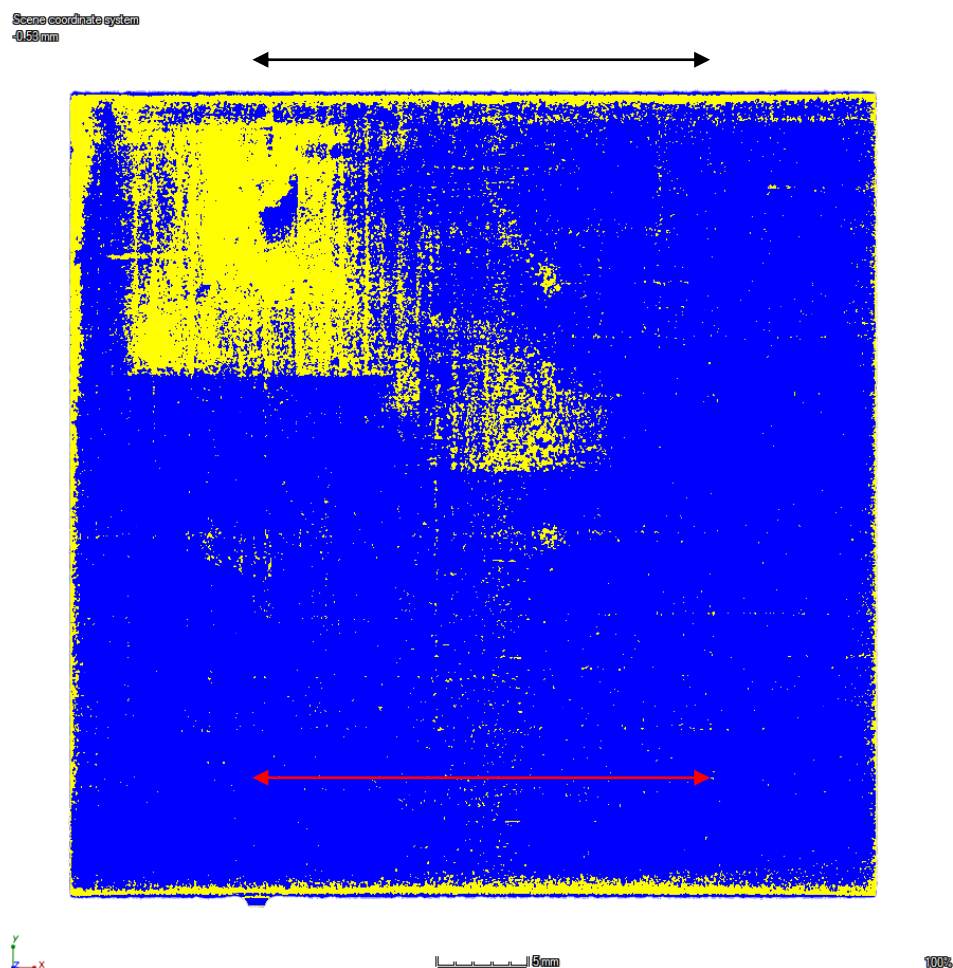


Figure 4.19: Segment with Largest Damaged Area for Cut Specimen 5 (Depth of 3.02 mm, Between Plies 24 and 25)

As before, the damage that was induced by the water-jet cutting of the specimen was isolated and measured. Similarly to specimen 4, due to the proximity of the corner damage to the damaged region of interest, care was needed to isolate the cutting-induced damage. From processing of the induced damage, it was found that the damage to the corner had a volume of  $201.7 \text{ mm}^3$ . After removal, the adjusted total damaged volume for specimen 5 was  $939.4 \text{ mm}^3$ , which was 0.1697 % of the total volume of the original

plate. The removal of the corner damage resulted in a 17.7 % reduction in damaged volume.

On each of the CT scan images for specimen 5, the maximum damage length in the horizontal ( $0^\circ$ ) direction and vertical ( $90^\circ$ ) direction were measured. A plot of these lengths at the ply interfaces can be seen in Figure 4.20 and Figure 4.21 for the  $0^\circ$  and  $90^\circ$  orientations, respectively. For these figures, the top-most lines correspond to the images nearest the impacted surface of the plate, with the top to bottom direction the same as for the physical plate. While the maximum damage length measurement did not always occur on the same centerline, for illustration purposes the measurements have been centered within the figures. As with specimen 3, there were two main damage modes present through the thickness of the plate. The first damage mode, transverse cracking, was the dominate mode in the top section of the plate. The second damage mode, delamination, was more prevalent on the middle and lower plies.

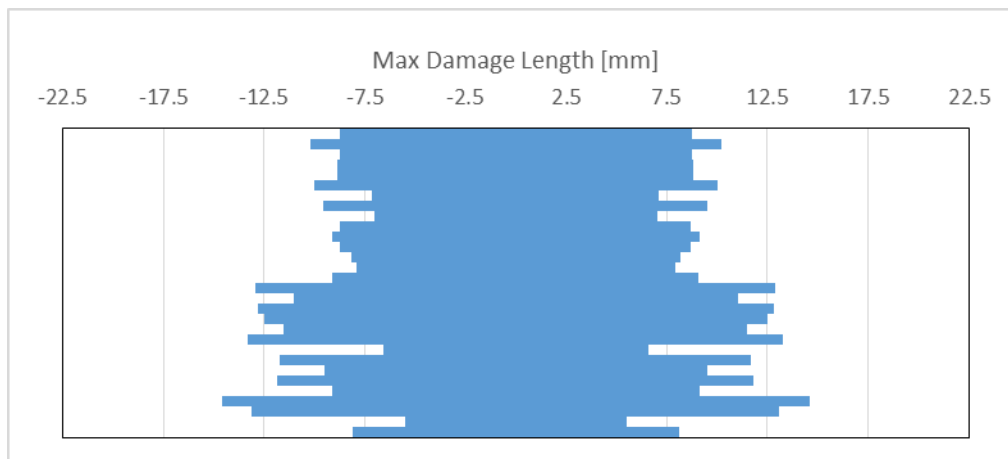


Figure 4.20: Maximum Damage Length in the 0° Direction for Specimen 5

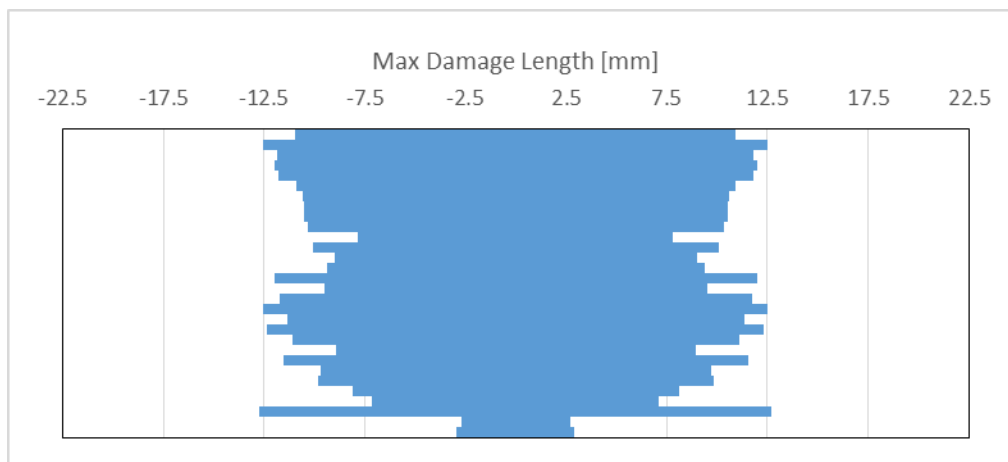


Figure 4.21: Maximum Damage Length in the 90° Direction for Specimen 5

From the cut specimen images, it was possible to individually identify the ply orientation for most slices. Since there were approximately 2.5 CT slices per ply, images

along the ply interfaces were able to be selected. The 30 different-direction ply interfaces for specimen 5 can be seen in Figure 4.22, where the black arrow near the first image indicates the global  $0^\circ$  fiber direction. As with specimen 3, the first image is at the interface between the top,  $0^\circ$  ply and the second,  $90^\circ$  orientation ply, and the pattern continues from there. No ply interface was included between the middle same-direction  $90^\circ$  orientation plies, and so images 15 and 16 reflect the change from  $0^\circ$  top/ $90^\circ$  bottom orientation to  $90^\circ$  top/ $0^\circ$  bottom orientation for each interface. As before, it can be seen that the delamination damage tends to extend in the direction of the lower ply. Also of note is the significant “damage” on the top and bottom ply interfaces. As discussed for specimen 3, this damage is an artifact from imaging along the surfaces of the plate and also the grey-value threshold used to isolate damage.

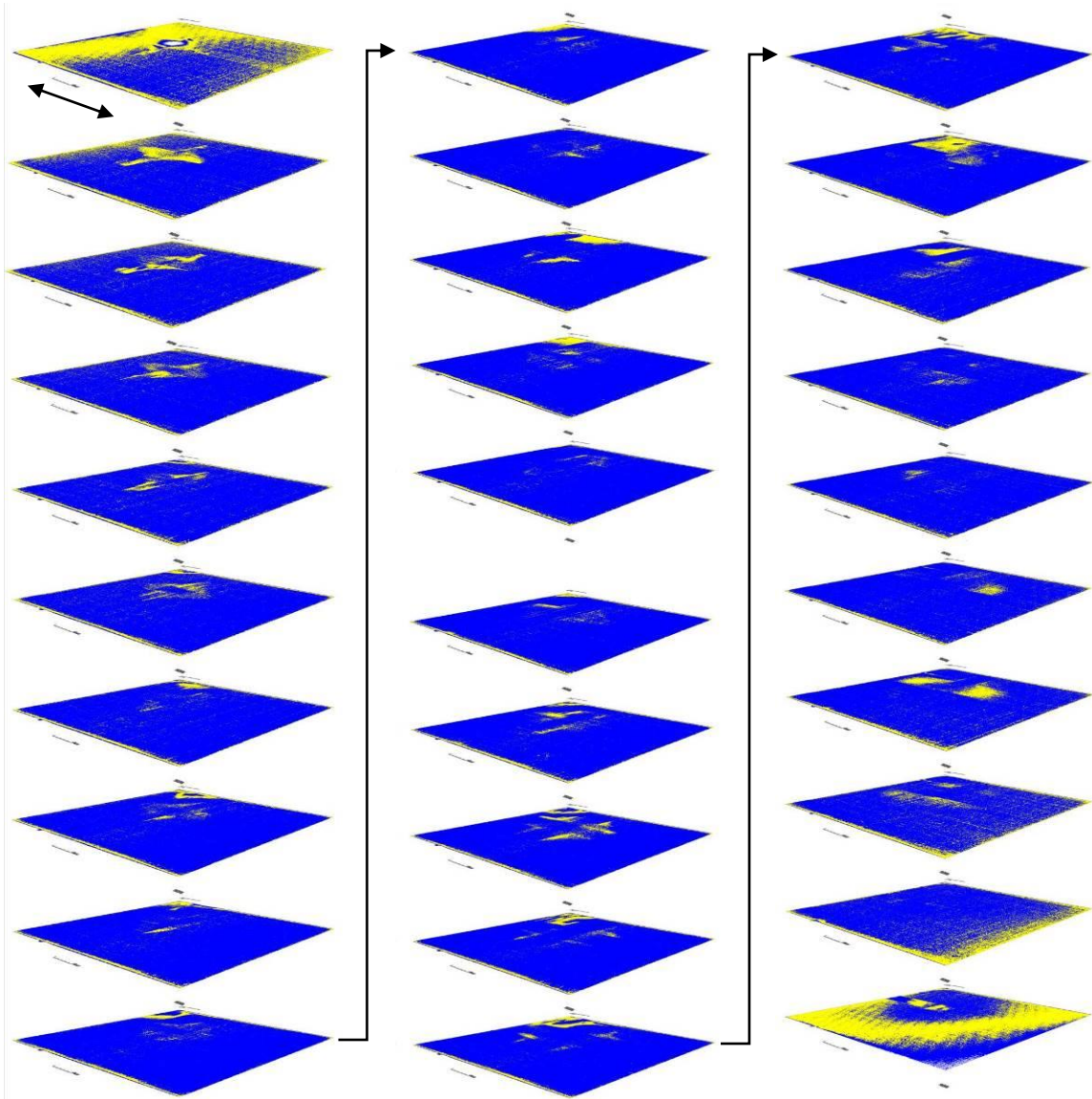


Figure 4.22: Ply Interfaces from Specimen 5

Examining each ply interface in turn, the general progression of damage for specimen 5 can be seen. As mentioned above, for the first interface the majority of damage comes from surface effects from imaging. Through the first five interfaces, the

damage pattern is fairly constant as it is a product of transverse cracks produced from the impact. Even in this area, the damage has a slight tendency to extend along the direction of the lower ply interface. The damage extent appears to decrease from the fifth ply downwards until approximately the 13<sup>th</sup> ply interface. Below this interface the damage has a distinct asymmetric pattern, with a generally inverted “+” shape. This shape tends to be longer in the direction of the lower ply, and this is most evident on interfaces 21 through 27. Also clearly visible on the lower interfaces is the corner delamination caused by cutting of the specimen. The last ply interface exhibits the edge-effect noise previously mentioned.

#### 4.3.4 Specimen 6

Specimen 6 had been impacted at an energy of 29.27 J. The CT scan for specimen 6 had a resolution of 0.1802 mm/px and resulted in a stack of 39 images through the thickness of the plate. From these images it was determined that the scan through the thickness had a total unadjusted depth of 6.49 mm. The maximum damage length was found to be 30.92 mm at a depth of 2.17 mm (relative depth of 3.24 mm), which can be seen in Figure 4.23. From image processing, it was found that the maximum internal damaged area also occurred at approximately 2.17 mm (3.24 mm relative depth) from the impacted surface. The maximum damaged area was measured to be 775.3 mm<sup>2</sup> and is shown in Figure 4.24. The damaged area is boxed in both figures, and the black arrow indicates the global 0° fiber orientation. From the damaged area for this slice, the maximum damaged volume per slice was calculated to be 139.7 mm<sup>3</sup>. The total damaged volume for specimen 6 was found to be 2671.3 mm<sup>3</sup>, which was approximately 0.479 % of the total volume.

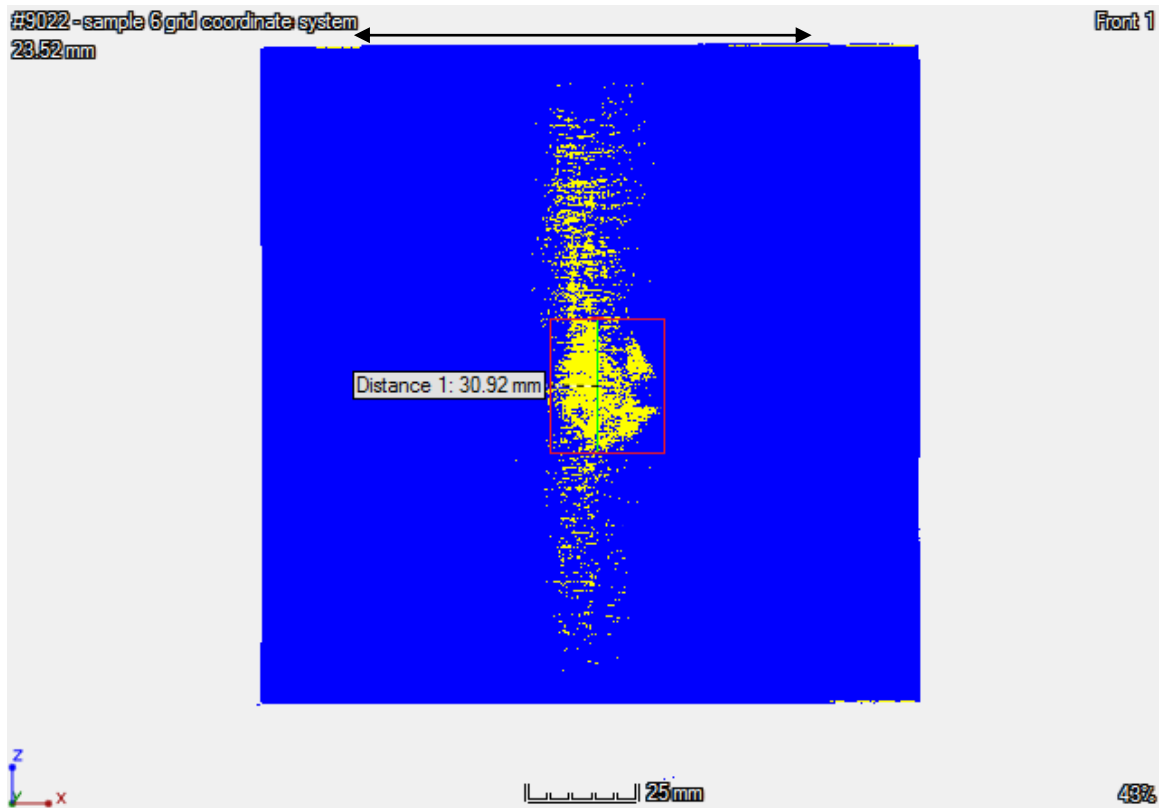


Figure 4.23: Length of Largest Internal Damage for Specimen 6 (Depth of 2.17 mm)

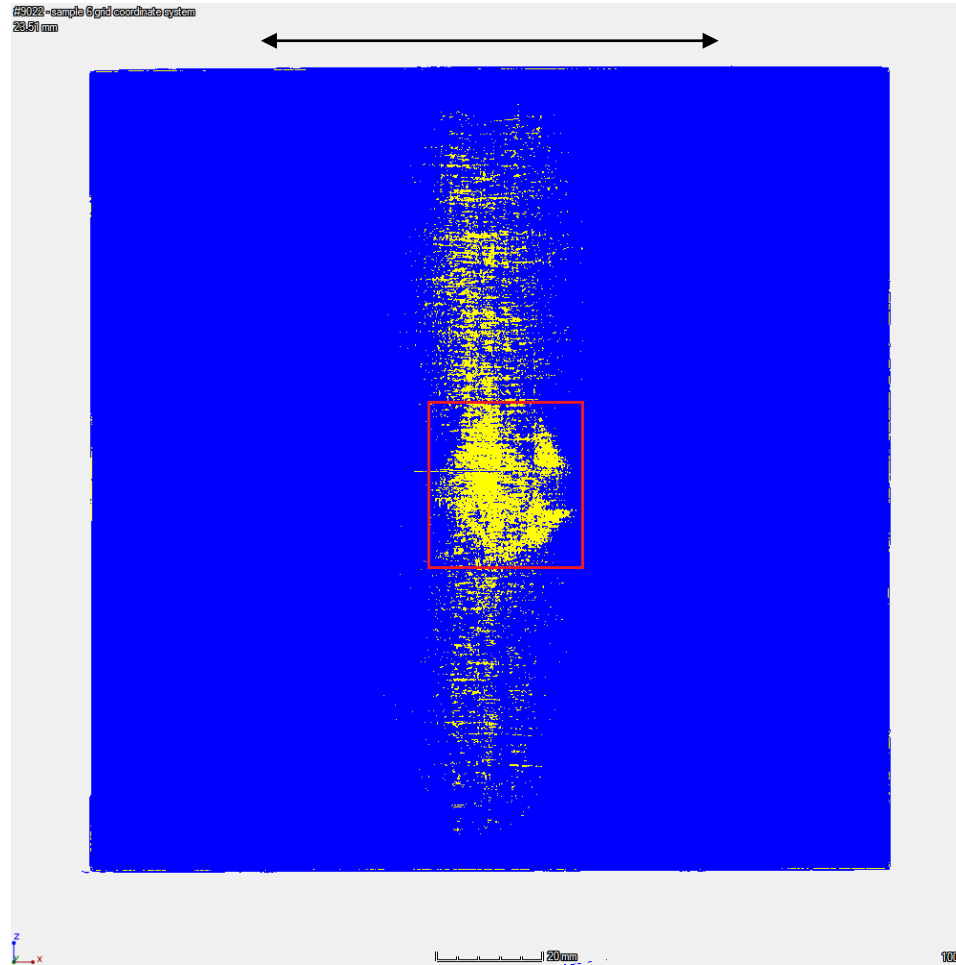


Figure 4.24: Segment with Largest Damaged Area for Specimen 6 (Depth of 2.17 mm)

After cutting of the central region, specimen 6 was imaged again. This CT imaging produced a stack of 91 images through the thickness of the plate at a resolution of 0.0588 mm/px. From these images it was determined that the scan had a total relative depth of 5.18 mm and a total measured depth of 4.20 mm. The maximum horizontal ( $0^\circ$  orientation) damage length was found to be 39.16 mm at a depth of 3.23 mm (3.47 mm relative depth, within the 25<sup>th</sup> ply) and the maximum vertical ( $90^\circ$  orientation) damage

length was found to be 35.80 mm at a depth of 0.53 mm (0.77 mm relative depth, within the 5<sup>th</sup> ply). From image processing of the cut plate, it was found that the maximum internal damaged area occurred at a depth of 1.76 mm (2.00 mm relative depth) from the impacted surface and was measured to be 357.74 mm<sup>2</sup>, shown in Figure 4.25. This occurred at the interface between the 14<sup>th</sup> and 15<sup>th</sup> plies from the top surface. In the figure, the black arrow above the plate indicates the global 0° fiber direction. As this segment was from a ply interface, the red arrow on the figure indicates the direction of the lower ply for that interface. From the damaged area for this slice, the maximum damaged volume per slice was 21.03 mm<sup>3</sup>. The total damaged volume for cut specimen 6 was found to be 1002.7 mm<sup>3</sup>, which was approximately 0.180 % of the total volume of the original plate. For this specimen, the cutting process induced additional delamination in the lower left corner as seen in Figure 4.25.

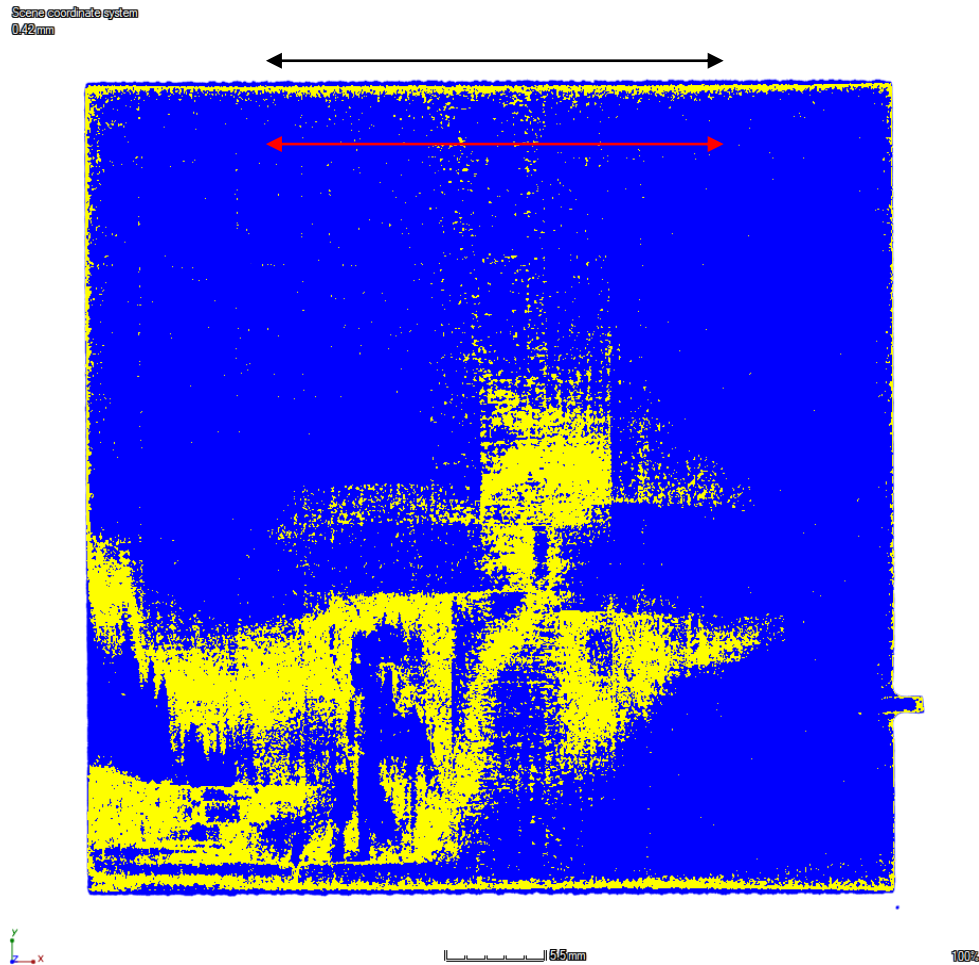


Figure 4.25: Segment with Largest Damaged Area for Cut Specimen 6 (Depth of 1.76 mm, Between Plies 14 and 15)

To obtain an accurate estimate of the damage caused only by the impact event, the damage induced by the water-jet cutting of specimen 6 was isolated and removed. After this processing, it was found that the damage to the corner had a volume of  $200.5 \text{ mm}^3$ . Removing this damage from the total for this specimen, the adjusted total damaged volume was found to be  $802.2 \text{ mm}^3$ , which was 0.1438 % of the total volume of the

original plate. This was a 20.0 % reduction in damaged volume as compared to the analysis including cutting-induced damage.

On each of the CT scan images for specimen 6, the maximum damage length in the horizontal ( $0^\circ$ ) direction and vertical ( $90^\circ$ ) direction were measured. A plot of these lengths at the ply interfaces can be seen in Figure 4.26 and Figure 4.27 for the  $0^\circ$  and  $90^\circ$  orientations, respectively. For these figures, the top-most lines correspond to the images nearest the impacted surface of the plate, with the top to bottom direction the same as for the physical plate. While the maximum damage length measurements did not always occur on the same centerline, for illustration purposes the measurements have been centered within the figures. As with the other specimens, there were two main damage modes present through the thickness of the plate: transverse cracking on the upper layers and delamination on the middle and lower layers.

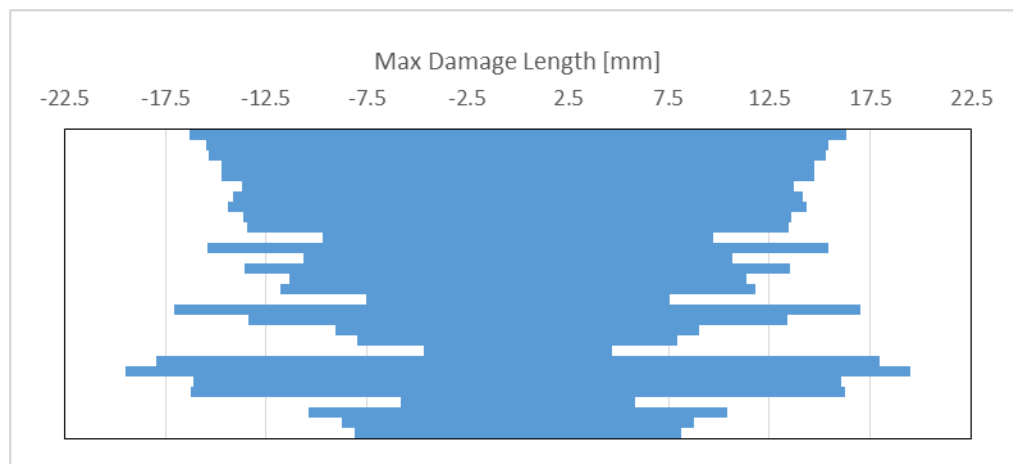


Figure 4.26: Maximum Damage Length in the  $0^\circ$  Direction for Specimen 6

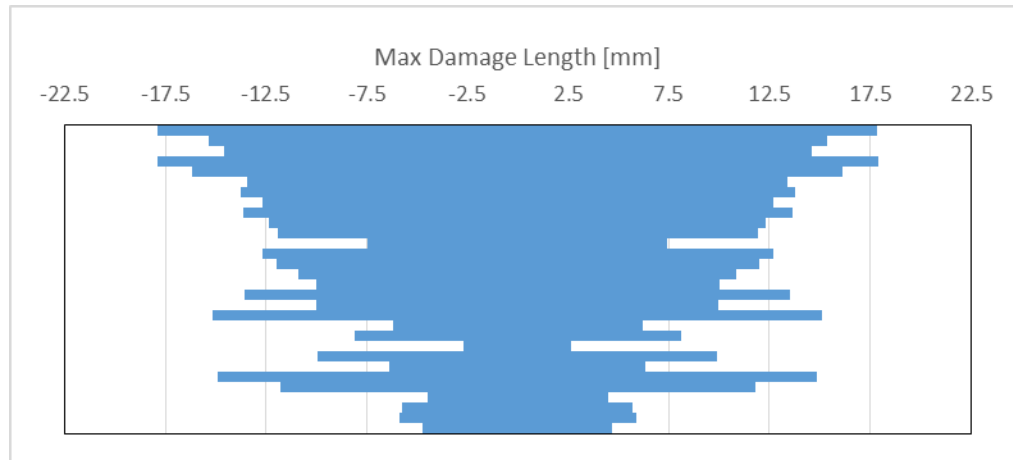


Figure 4.27: Maximum Damage Length in the 90° Direction for Specimen 6

From the cut specimen images, it was possible to individually identify the ply orientation for most slices. At this resolution there were approximately 2.5 CT images per ply, and so images along the ply interfaces were able to be selected. The 30 different-direction ply interfaces for specimen 6 can be seen in Figure 4.28, where the black arrow near the first image indicates the global 0° fiber direction. As with the previous specimens, the first image is at the interface between the top, 0° orientation ply and the second, 90° orientation ply, and the pattern continues from there. No ply interface was included between the middle same-direction 90° orientation plies, and so images 15 and 16 reflect the change from 0° top/90° bottom orientation to 90° top/0° bottom orientation for each interface. As can be seen from this figure, a large “+” damaged region dominates the upper set of interfaces. This damage is a product of transverse cracking

induced by the impact. The middle and lower plies have less coordinated damaged zones produced by delamination, and these regions generally extend in the direction of the lower ply fiber orientation.

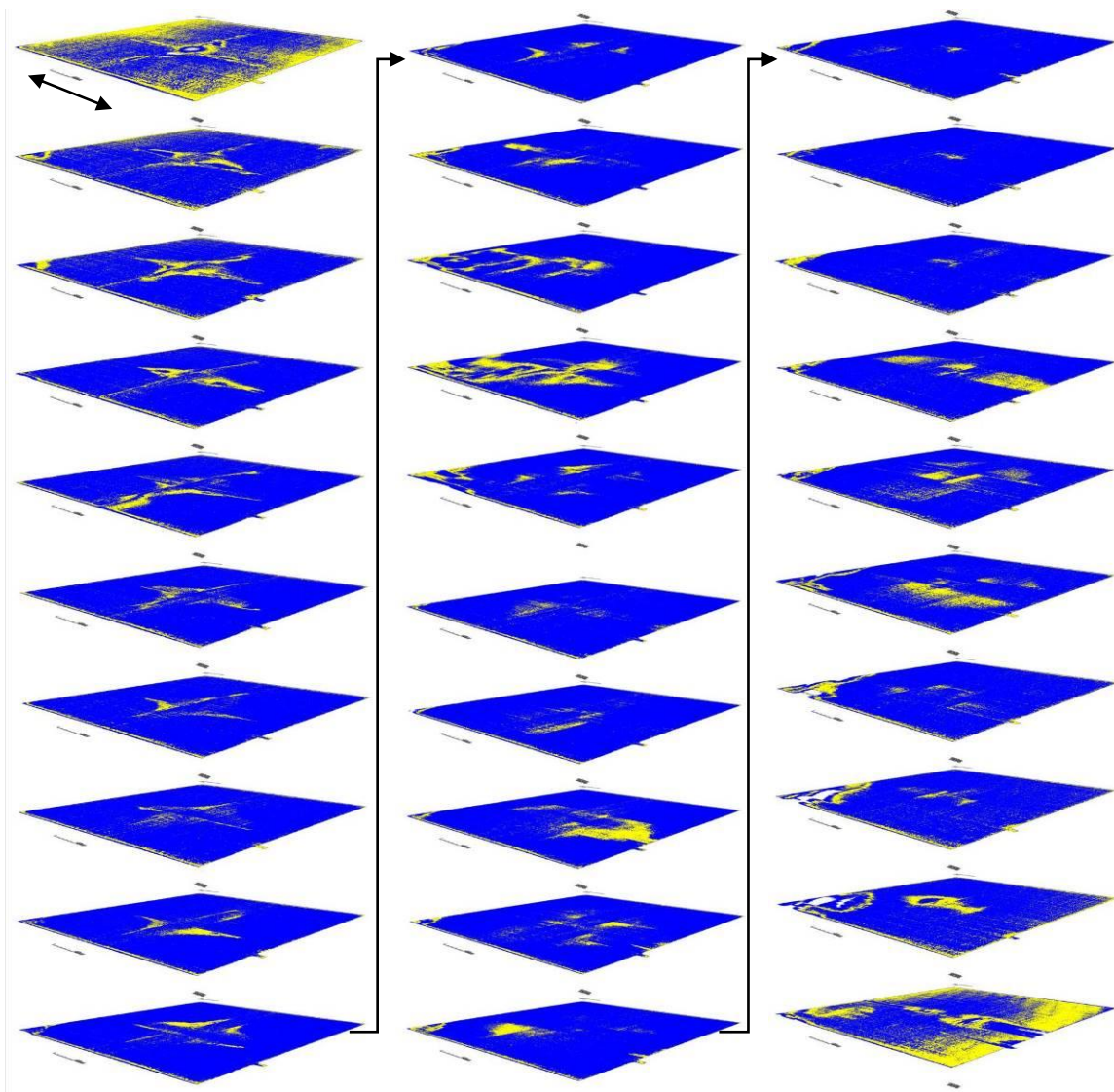


Figure 4.28: Ply Interfaces from Specimen 6

Examining each ply interface in turn, several notable damage features can be identified for specimen 6. On the outermost ply interfaces a significant amount of apparent damage comes from surface effects from scanning and the threshold used to isolate damage. Through the first nine ply interfaces a large “+” shaped damage region is dominant. This damage comes from the transverse cracks induced by the impact. Interfaces 11 through 14, while still showing traces of the “+” shaped damage, have more damage that stems from the corner delamination caused by specimen cutting. After the symmetric center interface the damage takes on highly asymmetric shapes, clearly extending in the direction of the lower ply interface orientation. This is most apparent on interfaces 18 and 24 through 27. Interfaces 26 through 30 also have a consistent and significant amount of corner delamination. The final ply interfaces have a damage pattern that corresponds to the raised damage on the back face. The last ply interface, like the first, also has surface-effect noise.

In comparison to the specimens impacted at a lower energy, specimen 6 did have more noticeable damage. The cracking from the top surface had a greater length and width, and also penetrated deeper into the specimen. The delaminated regions on the lower plies were also larger than those of the specimens impacted at a lower energy.

#### 4.3.5 Specimen 7

Specimen 7 had also been impacted at an energy of 29.27 J. The CT scan for specimen 7 had a resolution of 0.1802 mm/px and produced a stack of 43 images through the thickness of the plate. From these images it was determined that the scan through the

thickness had a total unadjusted depth of 7.21 mm. The maximum damage length was found to be 33.43 mm at a depth of 2.17 mm (relative depth of 3.06 mm), as seen in Figure 4.29. From image processing, it was found that the maximum internal damaged area also occurred at a depth of 2.17 mm (relative depth of 3.60 mm) and was measured to be 1092.0 mm<sup>2</sup>, shown in Figure 4.30. The damaged area is boxed in both figures, and the black arrow above the specimen indicates the global 0° fiber orientation. From the damaged area for this slice, the maximum damaged volume per slice was 196.8 mm<sup>3</sup>. The total damaged volume for specimen 7 was found to be 3889.0 mm<sup>3</sup>, which was roughly 0.689 % of the total volume.

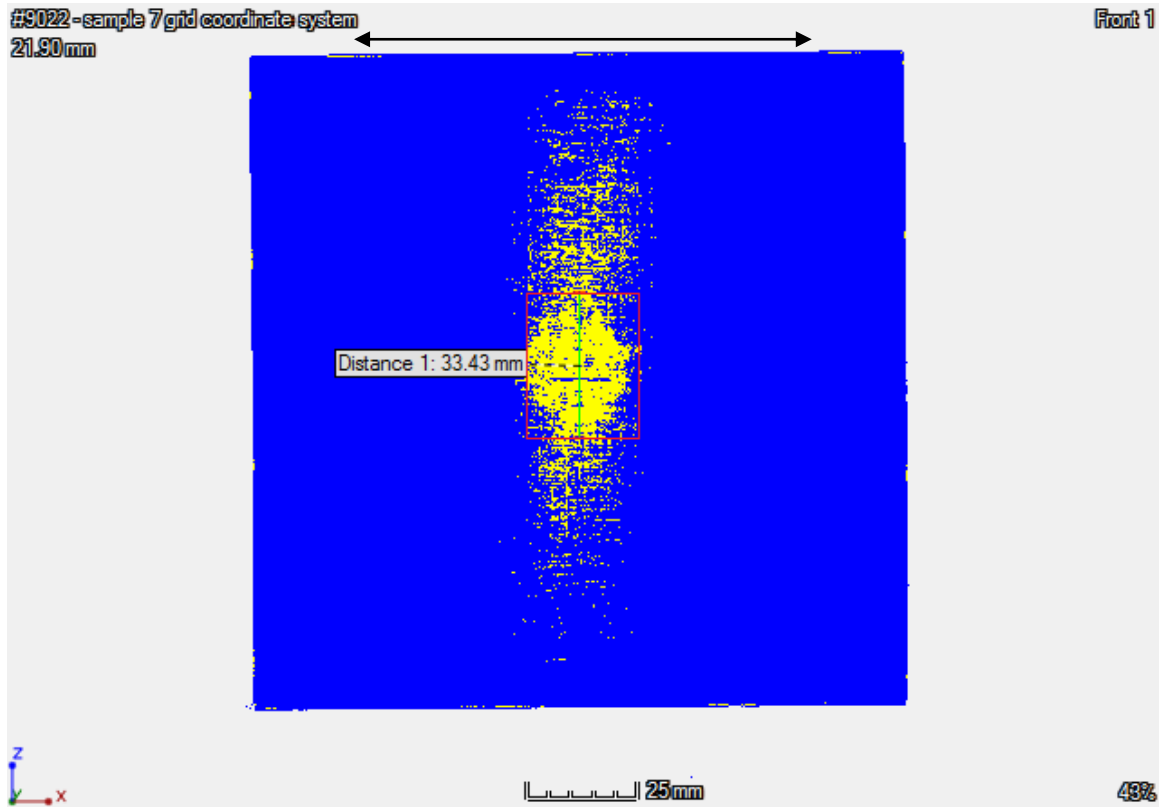


Figure 4.29: Length of Largest Internal Damage for Specimen 7 (Depth of 2.17 mm)

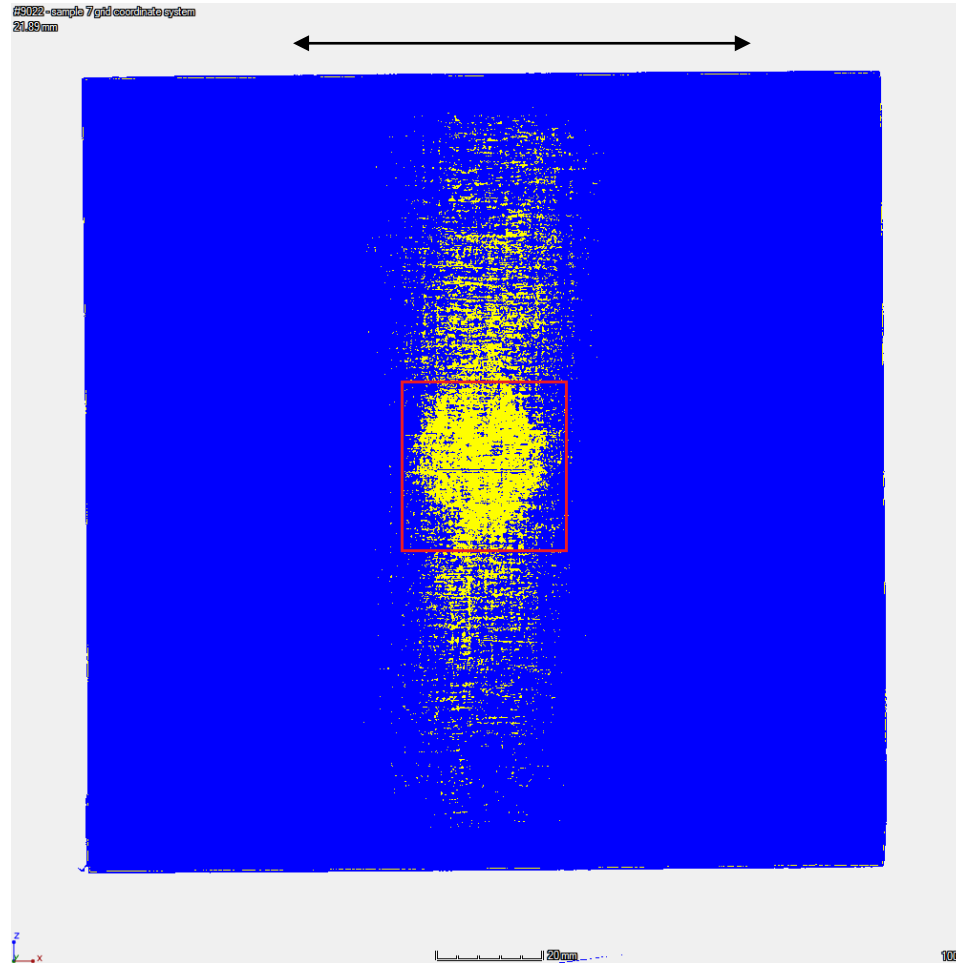


Figure 4.30: Segment with Largest Damaged Area for Specimen 7 (Depth of 2.17 mm)

After cutting of the central damaged region, specimen 7 was processed again. This CT imaging produced a stack of 88 images through the thickness of the plate at a resolution of 0.0588 mm/px. From these images it was determined that the scan had a total relative depth of 5.00 mm and a measured depth of 4.45 mm. The maximum horizontal ( $0^\circ$  orientation) damage length was found to be 32.64 mm at a depth of 3.68 mm (3.82 mm relative depth, within the 22<sup>nd</sup> ply) and the maximum vertical ( $90^\circ$

orientation) damage length was found to be 37.06 mm at a depth of 2.85 mm (3.12 mm relative depth, at the interface between the 27<sup>th</sup> and 28<sup>th</sup> plies). From image processing of the cut plate, it was found that the maximum internal damaged area occurred at a depth of 3.01mm (3.29 mm relative depth) from the impacted surface and was measured to be 494.52 mm<sup>2</sup>, shown in Figure 4.31. This occurred at the interface between the 23<sup>rd</sup> and 24<sup>th</sup> plies from the top surface. In this figure, the black arrow above the plate indicates the global 0° fiber direction. Because this slice was located at a ply interface (22<sup>nd</sup> ply interface from the top surface), the red arrow indicates the orientation of the lower ply. From the damaged area for this slice, the maximum damaged volume per slice was 29.08 mm<sup>3</sup>. The total damaged volume for specimen 7 was found to be 1282.7 mm<sup>3</sup>, which was approximately 0.227 % of the total volume of the original, uncut plate. For this specimen, the cutting process induced additional delamination in the lower right corner as seen in Figure 4.31.

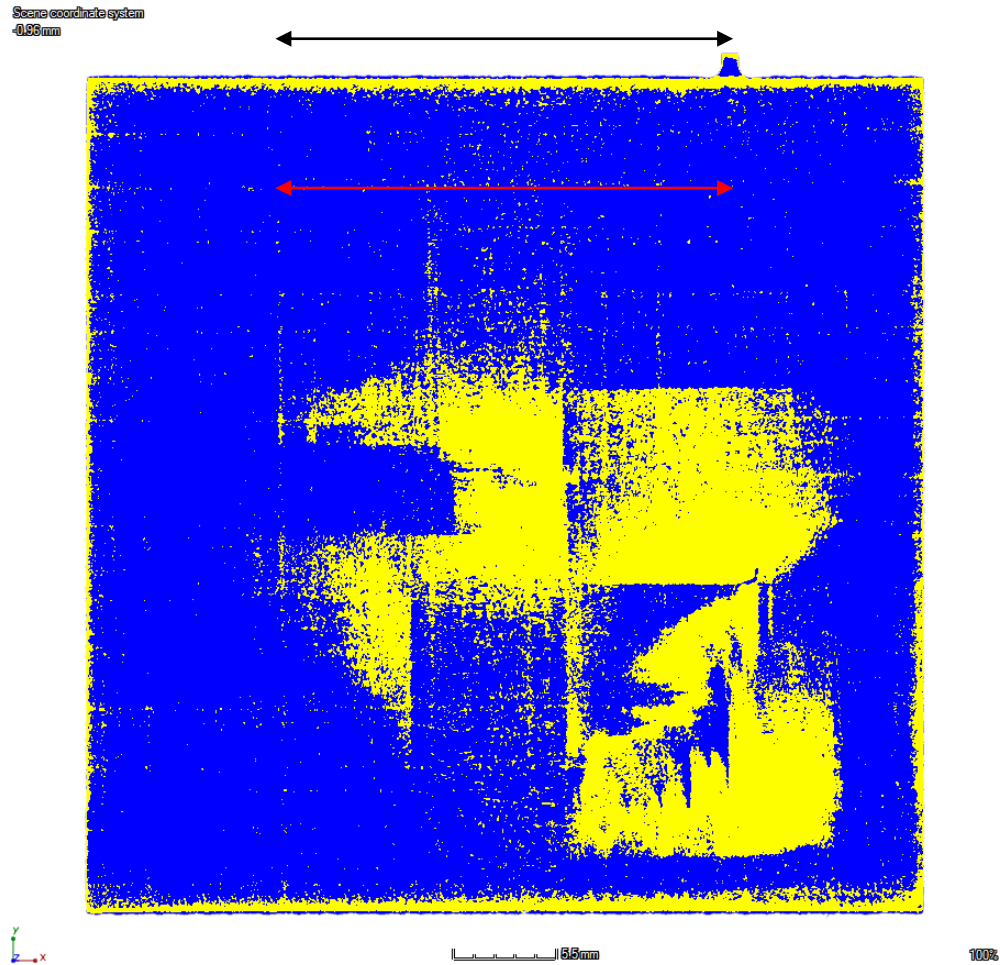


Figure 4.31: Segment with Largest Damaged Area for Cut Specimen 7 (Depth of 3.01 mm, Between Plies 23 and 24)

To obtain a more accurate estimate of the damage from the impact event, the water-jet induced damage was isolated and removed. After processing the corner damage, it was determined that the induced damage had a volume of  $191.1 \text{ mm}^3$ . Removing this damage from the total for specimen 7, it was found that the total plate damaged volume was  $1091.6 \text{ mm}^3$ , which was 0.1933 % of the total volume of the

original plate. This corresponded to a 14.9 % reduction in damage as compared to the measurement including cutting-induced damage.

On each of the CT images for specimen 7 the maximum damage length in the horizontal ( $0^\circ$ ) direction and vertical ( $90^\circ$ ) direction were measured. A plot of these lengths at the ply interfaces can be seen in Figure 4.32 and Figure 4.33 for the  $0^\circ$  and  $90^\circ$  ply orientations, respectively. For both of these figures, the top-most lines correspond with the first ply interfaces, and the lower lines with the lower ply interfaces away from the top. As before, while the centers of the maximum damage lengths did not always line up, for illustration purposes the measurements have been centered in the figures. As discussed previously, the top region of maximum damage length is dominated by cracking from the impacted surface. After this region, the maximum damage length tends to correspond to delamination. For specimen 7, while damage length and depth did not appear to have a strong relationship in the  $90^\circ$  direction, the damage lengths in the  $0^\circ$  direction (Figure 4.32) did support the conclusion that damage generally increased with increasing plate depth.

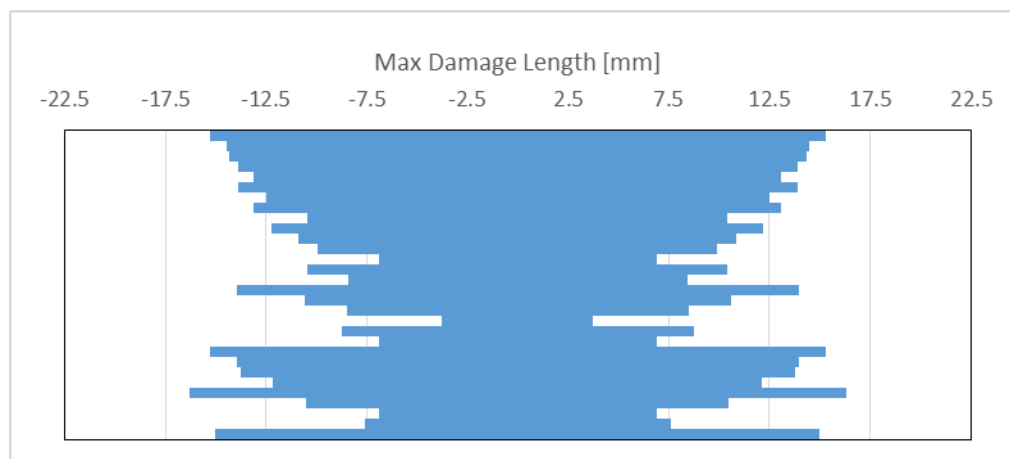


Figure 4.32: Maximum Damage Length in the  $0^\circ$  Direction for Specimen 7

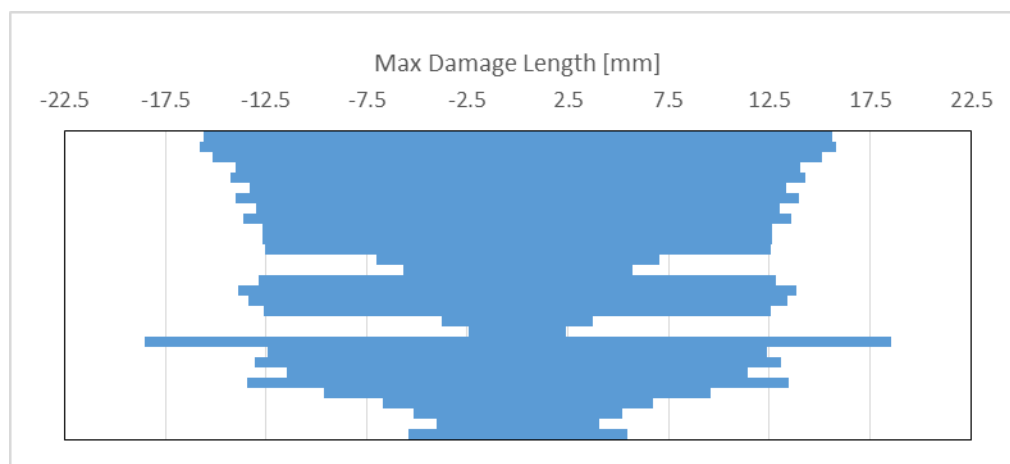


Figure 4.33: Maximum Damage Length in the  $90^\circ$  Direction for Specimen 7

From the cut specimen images, it was possible to identify the ply orientation for most slices. Further, since there were approximately 2.5 CT images per ply, images

along the ply interface could usually be selected for this specimen. The 30 different-direction ply interfaces for specimen 7 can be seen in Figure 4.34, where the black arrow near the first image indicates the global  $0^\circ$  fiber direction. As before, the first image is at the interface between the top,  $0^\circ$  orientation ply and the second,  $90^\circ$  orientation ply, and the pattern continues from there. No ply interface was included between the middle same-direction  $90^\circ$  orientation plies, and so images 15 and 16 reflect the change from  $0^\circ$  top/ $90^\circ$  bottom orientation to  $90^\circ$  top/ $0^\circ$  bottom orientation for each interface. As can be seen from this figure, and as would be expected, the damage tends to extend in the direction of the lower ply orientation. This is most notable on the lower ply interfaces. As before, the top and bottom surfaces have been labeled with a significant amount of “damaged pixels” despite this coding not correlating to actual damage. This edge-effect noise is consistent with the results obtained from all other cut specimens, and is a product of surface effects and the threshold used when differentiating the CT grey-values.

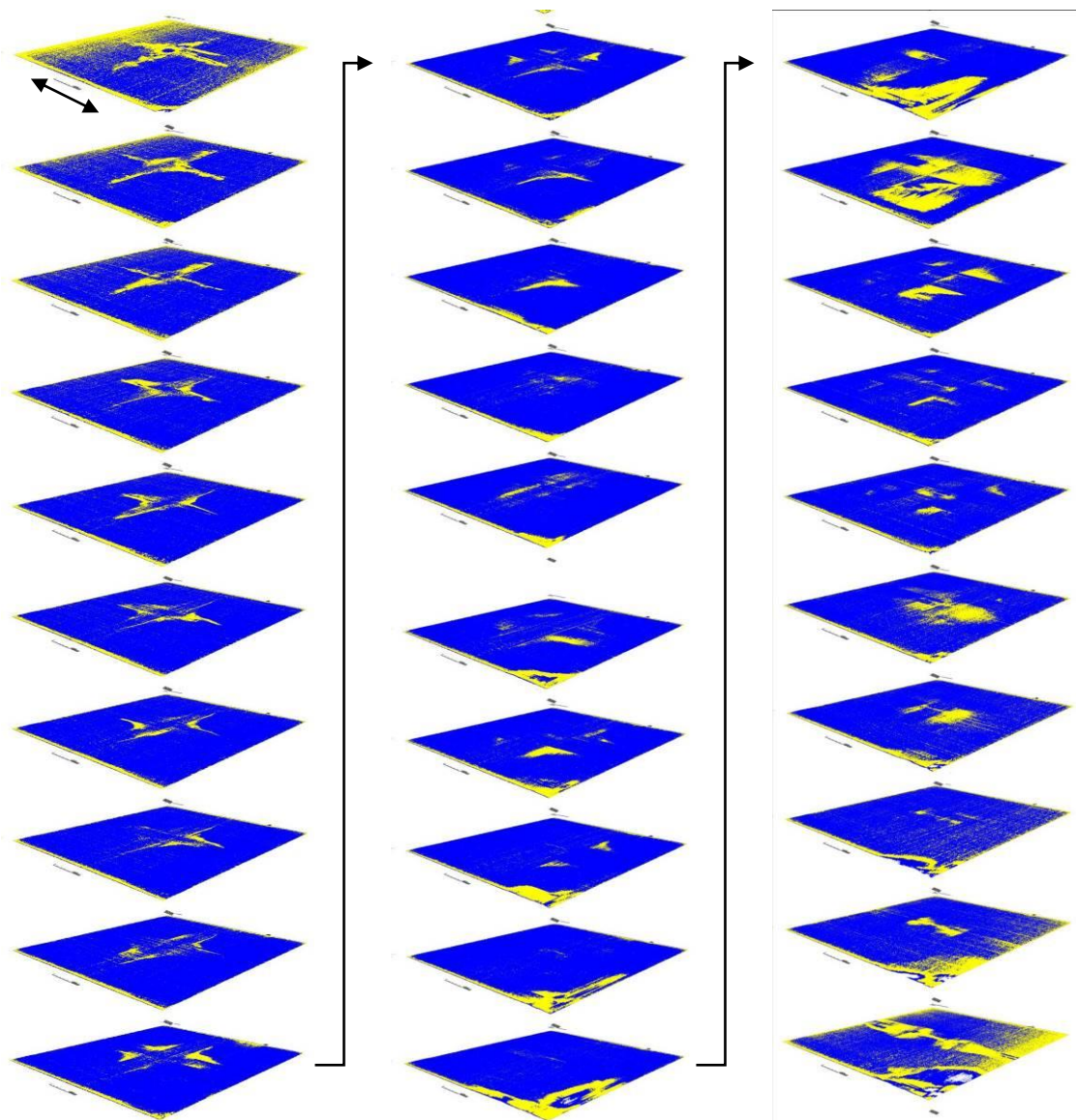


Figure 4.34: Ply Interfaces from Specimen 7

Examining each ply interface in turn, the overall damage pattern can be seen for specimen 7. For the first ply interface, between the top  $0^\circ$  direction ply and the next  $90^\circ$  direction ply, a significant portion of the “damage” is merely a product of edge-effects and the threshold used to isolate damage, as previously mentioned. The small difference

in angle between the specimen and the imaging plane biased the noise towards one edge of the plate (in this case, the upper left edge). Despite this, the first ply also indicates real damage in the form of the “+” shaped damage zone. This damage is a product of the surface cracks formed from the impact event. This damage penetrates down to the eighth ply interface, after which it is no longer a significant source of damage. Starting with the ninth ply interface, the damage tends to extend in the direction of the lower ply, as is expected. While this generally holds true, some of the ply interfaces (notably interfaces 10 and 11) have a damaged region in the form of an inverted “+” shape, with damage in the four quadrants around the horizontal and vertical centerlines. This region becomes less defined on the lower half of the ply interfaces, but the general shape can still be seen. The inverted “+” shape can be most clearly seen again at interfaces 21 and 22, where it has increased in size as compared to interfaces 10 and 11. Interfaces 20 through 22 are also notable for having the greatest corner delamination, which was a product of the water-jet cutting of the specimens. Interfaces 28 through 30 have a “dog bone” shaped damaged region in the center, which corresponds to the raised backside damage on specimen 7. The final ply interface, similarly to the first, has edge-effect noise along one side. On the back side, however, the noise was biased towards the opposite edge (lower right in Figure 4.34).

This analysis provides further insight into the differences between the specimens impacted at different energies. While both the specimens impacted at lower and higher energies had cracking on the first few ply interfaces, the specimens impacted at higher energies had a greater extent of crack damage. For specimen 3, cracks only penetrated through the first four or five ply interfaces. Specimen 7, which was impacted at a higher

energy than specimen 3, had crack damage through the eighth ply interface. While both specimens 3 and 7 generally had increased damage lengths with increased depth, the maximum damage lengths for specimen 7 were larger in magnitude than for specimen 3.

#### 4.3.6 Specimen 8

Specimen 8 had also been impacted at an energy of 29.27 J. The resolution for the CT scan of specimen 8 was 0.1802 mm/px and produced a stack of 43 images through the thickness of the plate. From these images, the total unadjusted depth through the thickness was determined to be 7.21 mm. The maximum damage length was found to be 38.46 mm at a depth of 2.32 mm (relative depth of 3.42 mm), as seen in Figure 4.35. From image processing, it was found that the maximum internal damaged area occurred at a depth of 2.55 mm (relative depth of 3.60 mm) from the impacted surface. The maximum internal damaged area was measured to be 904.3 mm<sup>2</sup> and can be seen in Figure 4.36. The black arrow indicates the global 0° fiber orientation, and the damaged area is boxed in both figures. From the damaged area for this slice, the maximum damaged volume per slice was 163.0 mm<sup>3</sup>. The total damaged volume for specimen 8 was found to be 3368.8 mm<sup>3</sup>, which was approximately 0.556 % of the total volume

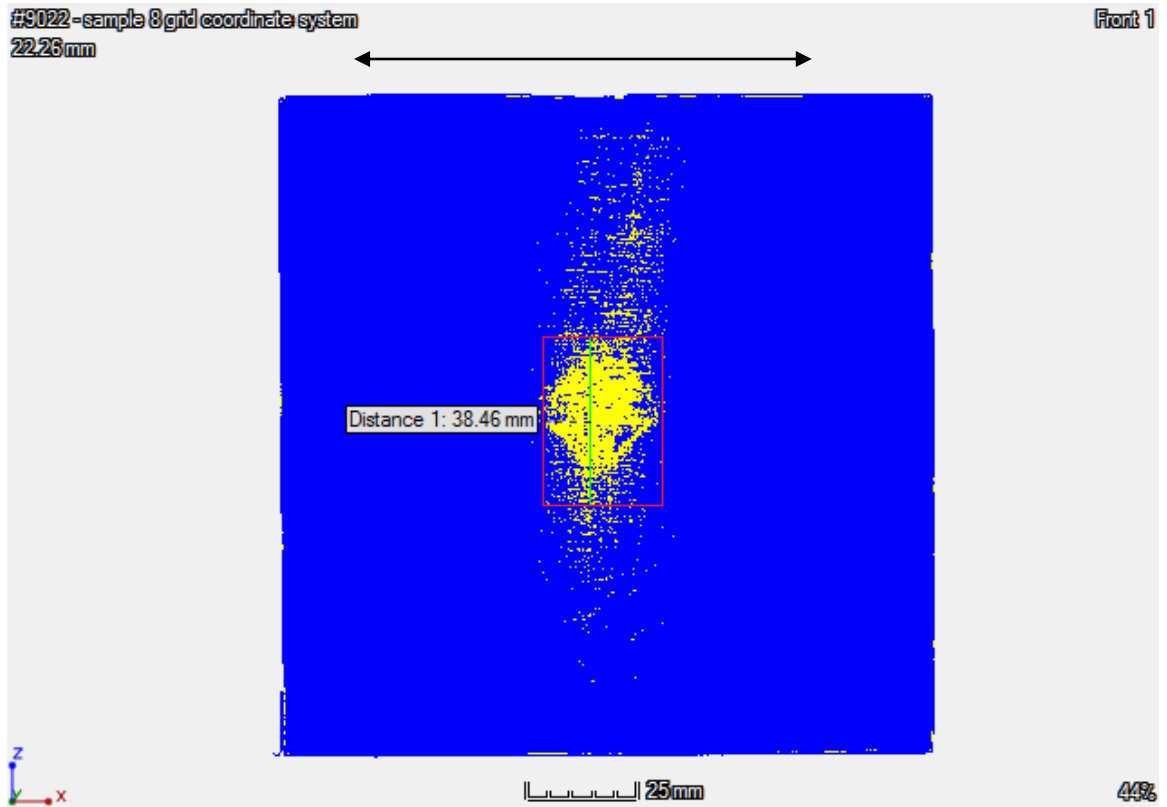


Figure 4.35: Length of Largest Internal Damage for Specimen 8 (Depth of 2.32 mm)

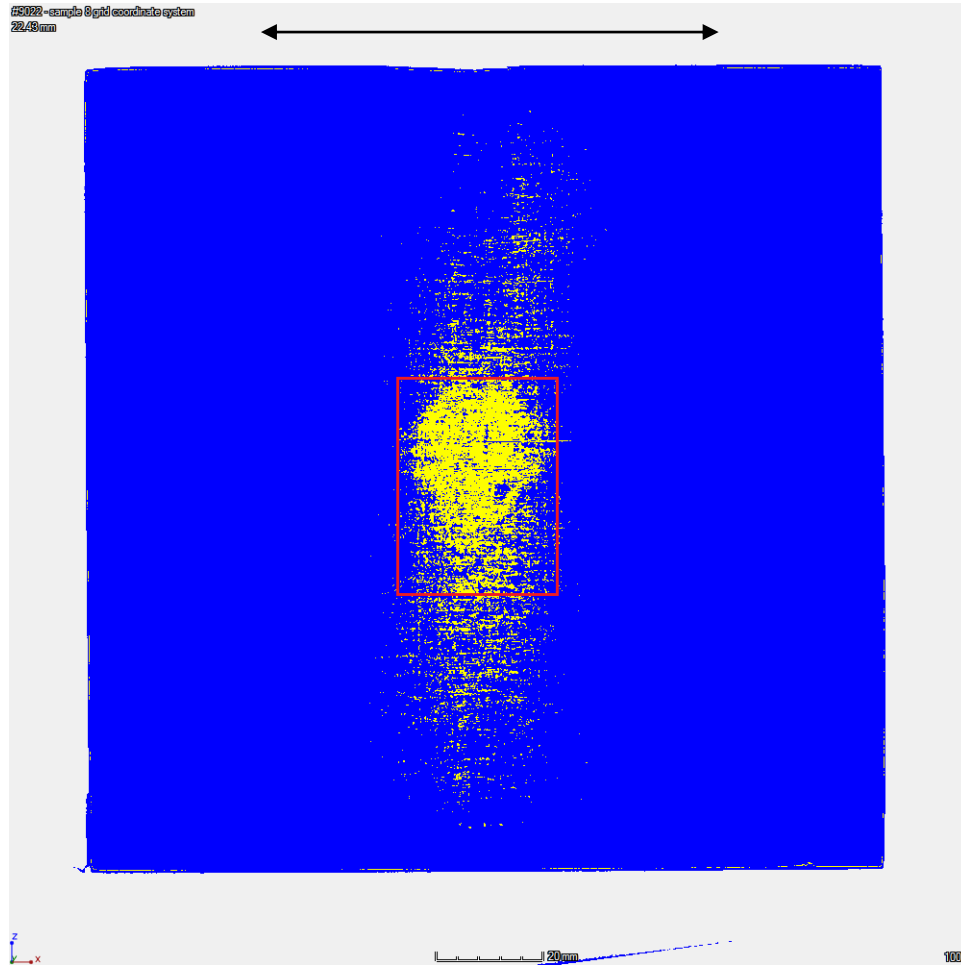


Figure 4.36: Segment with Largest Damaged Area for Specimen 8 (Depth of 2.55 mm)

After cutting out the central damaged region of specimen 8, the plate was again CT imaged. This produced a stack of 90 images through the thickness of the plate at a resolution of 0.0588 mm/px. From these images it was determined that the scan had a total relative depth of 5.12 mm and a central measured depth of 4.27 mm. The maximum horizontal ( $0^\circ$  orientation) damage length was found to be 32.65 mm at a depth of 3.49 mm (3.65 mm relative depth) and the maximum vertical ( $90^\circ$  orientation) damage length

was found to be 40.63 mm at a depth of 0.65 mm (0.83 mm relative depth). From image processing of the cut plate, it was found that the maximum internal damaged area occurred at a depth of 3.57 mm (3.77 mm relative depth) from the impacted surface and was measured to be 419.42 mm<sup>2</sup>, shown in Figure 4.37. In this figure, the black arrow above the plate indicates the global 0° fiber direction. From the damaged area for this slice, the maximum damaged volume per slice was 24.66 mm<sup>3</sup>. The total damaged volume for cut specimen 4 was found to be 1515.5 mm<sup>3</sup>, which was approximately 0.250 % of the total volume of the original plate. For this specimen, the cutting process induced additional delamination in the upper right corner, as seen in Figure 4.37.

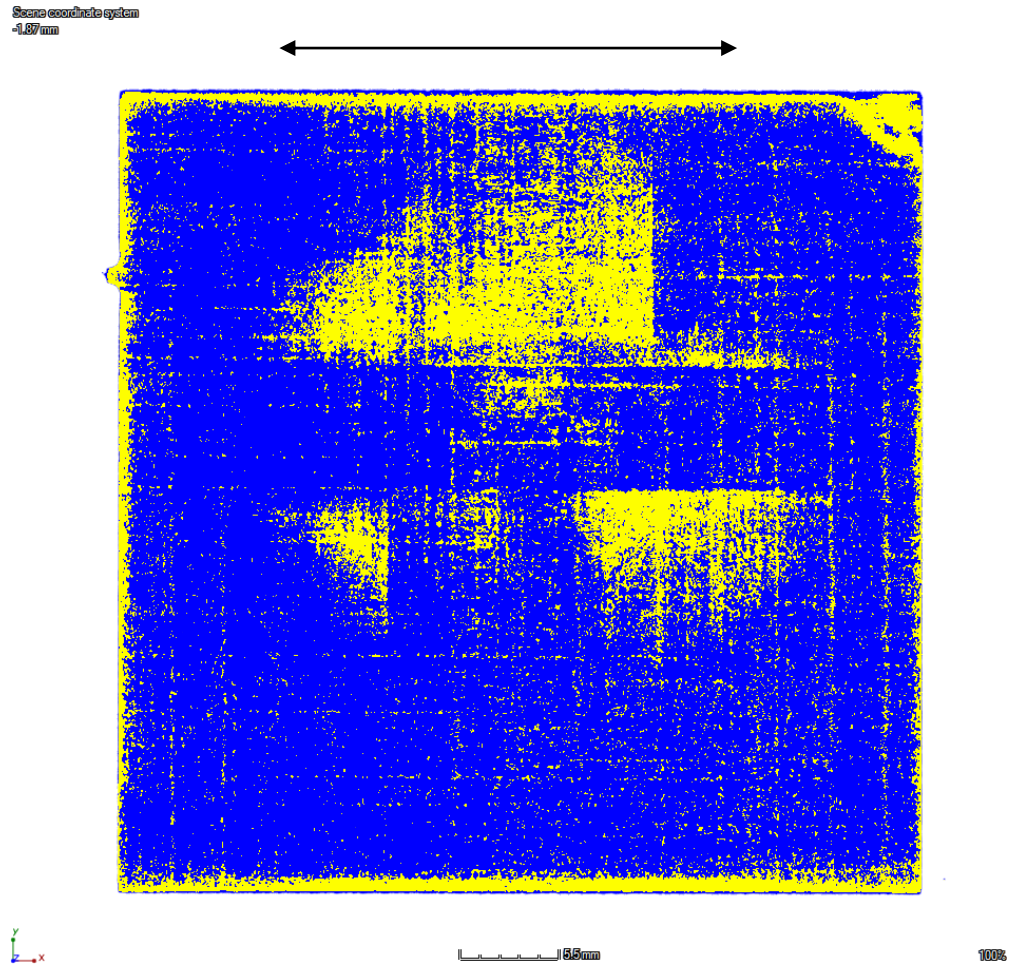


Figure 4.37: Segment with Largest Damaged Area for Cut Specimen 8 (Depth of 3.57 mm)

To isolate the effect of the water-jet induced damage to the corner of specimen 8, the damage in that region was isolated and measured. It was found that the cutting damage had a volume of  $218.9 \text{ mm}^3$ . Removing this damage from the total measured for this specimen, it was determined that the total adjusted damaged volume was  $1296.6 \text{ mm}^3$ , which was 0.2139 % of the volume of the original plate. This was a 14.4 %

reduction in damaged volume compared to an analysis including water-jet induced damage.

Similarly to specimen 4, analysis at the ply interfaces for specimen 8 could not be completed. During CT scanning, specimen 8 was held at a small angle relative to the imaging plane. This inclination was on the order of millimeters, but due to the high resolution of the scan resulted in each image cutting across multiple plies. Because of this the ply interfaces are not uniquely captured in the images, and so an interface-by-interface analysis was not able to be performed.

#### 4.3.7 Specimens 9, 10, and 11

Specimens 9, 10, and 11 were impacted under the same loading conditions as specimens 6, 7, and 8, but with a flat DELRIN® tup insert instead of a hemispherical tool steel tup insert. Therefore, specimens 9, 10, and 11 were impacted at an energy of 29.25 J. These three specimen were imaged in a similar manner to specimens 3 through 8, but with a slightly improved resolution of 0.1670 mm/px. While this was an improvement over the resolution of 0.1802 mm/px used for the first six specimens, it was still not fine enough to capture the 0.1397 mm-thick plies individually.

Even with an increased resolution, the image processing for the three specimen impacted with the DELRIN® tup insert was not able to identify the internal damage region. Figure 4.38 shows a colorized image from the interior of specimen 9, with the black arrow indicating the global 0° fiber orientation. As before, the gradient lines that appear on the plate boundary can be seen. Due to the relatively extreme angle of the CT scan, both the gradient lines for the front and the back of the plate appear in the same image. For this set of specimen the yellow region in the interior of the plate did not

accurately indicate damage, but instead simply represented noise in the filtered CT image. Any regions of internal damage were not able to be filtered from the image noise at this resolution. These results were consistent across specimens 9, 10, and 11.

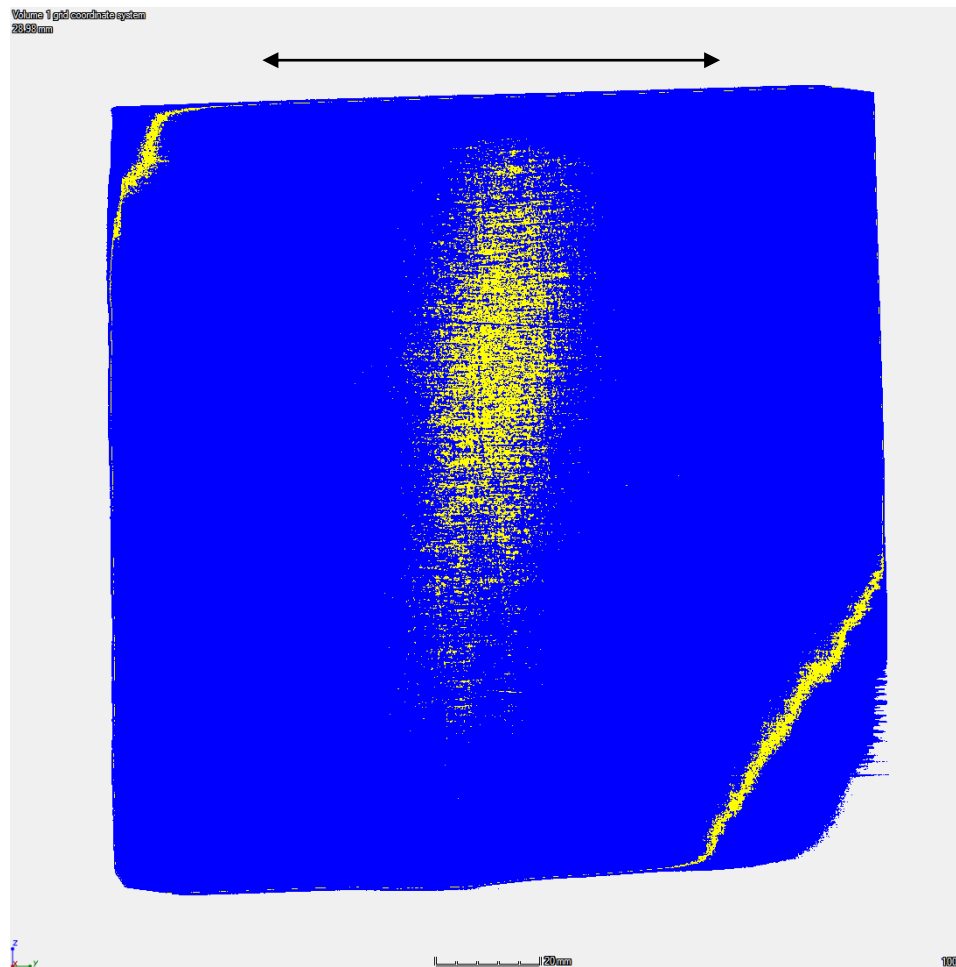


Figure 4.38: Internal Segment from Specimen 9 (Depth of 4.17 mm)

As with the other specimens, specimens 9, 10, and 11 were also cut down to 45 mm square plates taken from the center of the specimens. This produced images with a resolution of 0.0588 mm/px. While this increased resolution did help reduce the amount of noise in each slice, no internal impact damage was visible or was able to be captured in the thresholding process. Only specimens 9 and 11 produced meaningful results at this size, as specimen 10 was improperly cut on the water-jet. The fixture used to hold the specimens and the cutting head were not aligned accurately at the origin of the toolpath, which resulted in specimen 10 being cut improperly. Specimen 10 was still CT imaged, but no meaningful results were able to be obtained from image processing. A typical internal slice from specimen 9 can be seen in Figure 4.39, where the black arrow indicates the global 0° fiber orientation. Also note the damage in the upper left corner of the specimen, which was delamination caused by the water-jet cutting.

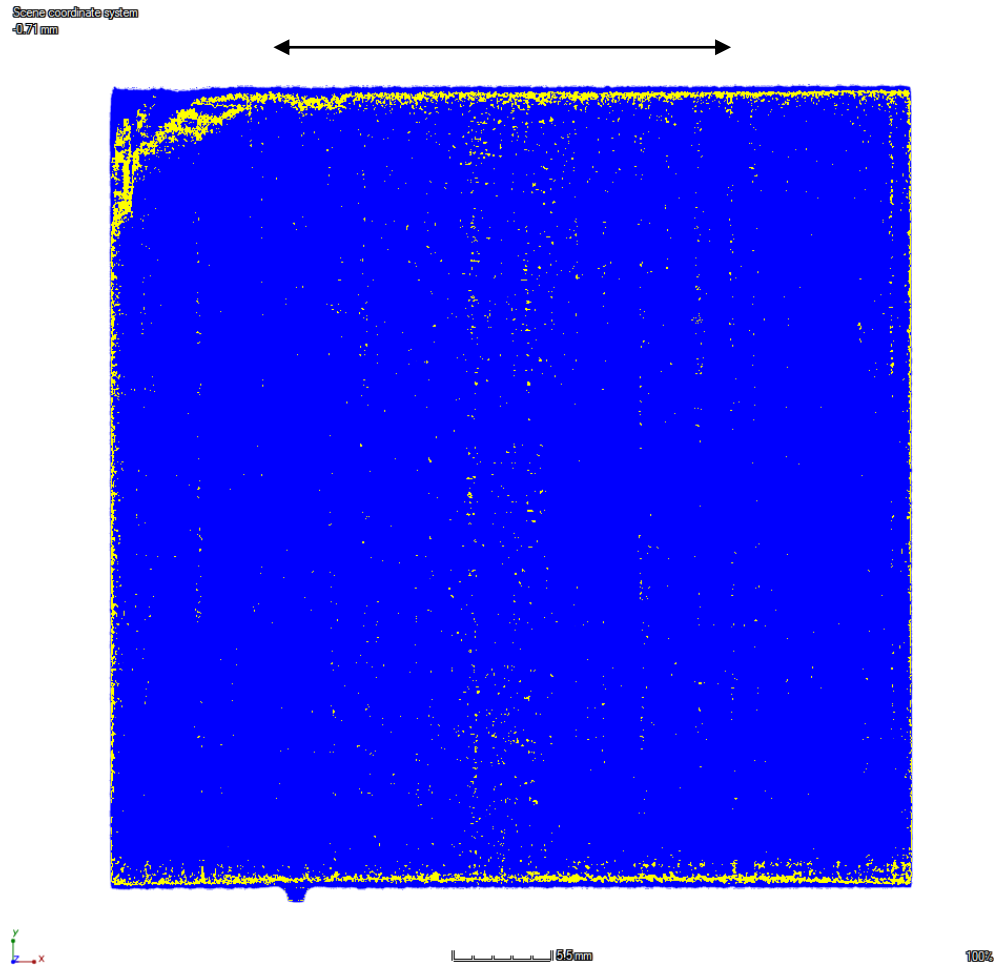


Figure 4.39: Internal Segment from Cut Specimen 9

#### 4.4 Analysis of Image Processing Results

##### 4.4.1 Overall Results

Overall, the specimens impacted at higher energies developed greater internal damage. This can be seen in Table 4.1, where specimens 6, 7, and 8 (impacted at 29.27

J) have greater damage length and volume than specimens 3, 4, and 5 (impacted at 20.77 J). Specimen 9 (impacted at 29.27 J using a DELRIN® tup insert) is included in Table 4.1 so as to show the relative amount of noise measured as damage in the specimens impacted with the DELRIN® tup insert. For specimen 9, the total damaged volume and percent damaged volume were most similar to the results from specimens 6, 7, and 8 despite not actually representing anything meaningful. This illustrates that, for specimens with a low amount of detectable internal damage at low resolutions, the amount of noise can be on the same order as a typical measurement.

Table 4.1: Full Specimen Damage Measurements

Specimen	Resolution [mm/px]	Max Damage Length [mm]	Depth of Max Damage Length (Adjusted) [mm]	Max Damage Area [mm <sup>2</sup> ]	Depth of Max Damage Area (Adjusted) [mm]	Total Damaged Volume [mm <sup>3</sup> ]	% Damaged Volume
3	0.1802	29.73	2.58	1040.9	2.48	2097.0	0.359
4	0.1802	24.62	2.67	226.1	2.40	1331.5	0.214
5	0.1802	26.79	2.49	887.8	2.32	2401.8	0.434
6	0.1802	30.92	2.17	775.3	2.17	2671.3	0.479
7	0.1802	33.43	2.17	1092.0	2.17	3889.0	0.689
8	0.1802	38.46	2.32	904.3	2.55	3368.8	0.556
9	0.1670	N/A	N/A	N/A	N/A	3690.0	0.561

From the impact and full-sized specimen imaging results, shown in Table 4.2, basic correlations can be drawn. As the impact energy increased, the damaged volume increased. Damaged volume had a positive correlation with maximum load and

maximum deflection, but that relationship was generally weak. The graphical relation between damaged volume and impact energy, maximum impact force, and maximum displacement can be seen in Figure 4.40, Figure 4.41, and Figure 4.42, respectively.

Table 4.2: Specimen Impact and Imaging Results

Specimen	Impact Energy [J]	Max Load [N]	Max Deflection [mm]	Max Damage Length [mm]	Total Damaged Volume [mm <sup>3</sup> ]	% Damaged Volume
3	20.77	7642.8	5.64	29.73	2097.0	0.359
4	20.77	7752.1	5.53	24.62	1331.5	0.214
5	20.77	7963.2	5.55	26.79	2401.8	0.434
6	29.27	9241.4	6.44	30.92	2671.3	0.479
7	29.27	9192.1	6.54	33.43	3889.0	0.689
8	29.27	9326.0	6.55	38.46	3368.8	0.556
9	29.25	11644.7	6.31	N/A	3690.0	0.561

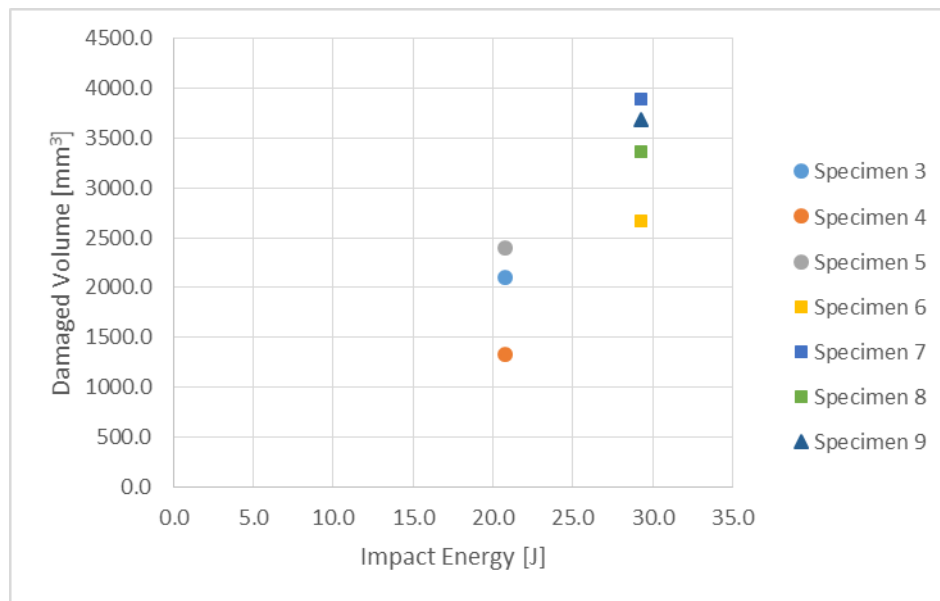


Figure 4.40: Damaged Volume versus Impact Energy for All Specimens

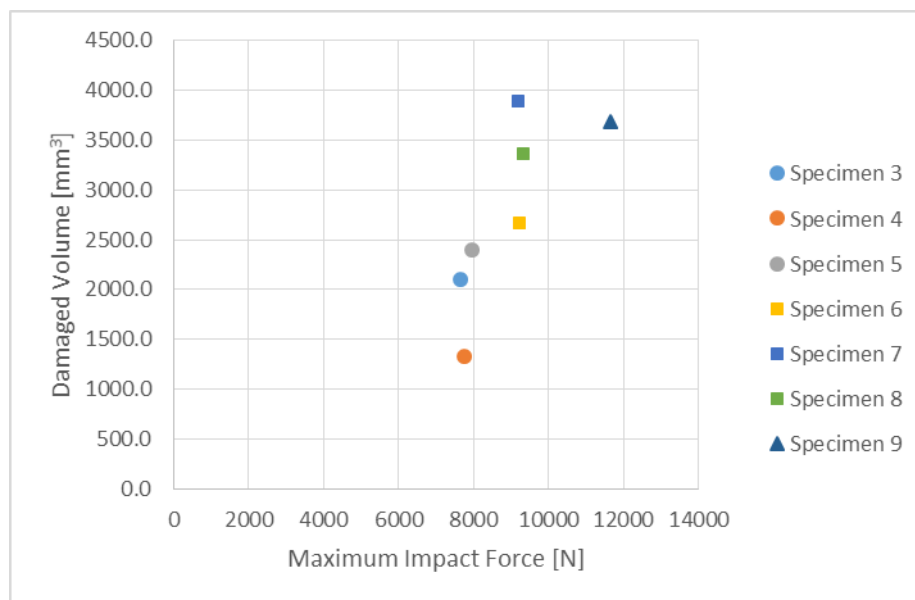


Figure 4.41: Damaged Volume versus Maximum Impact Force for All Specimens

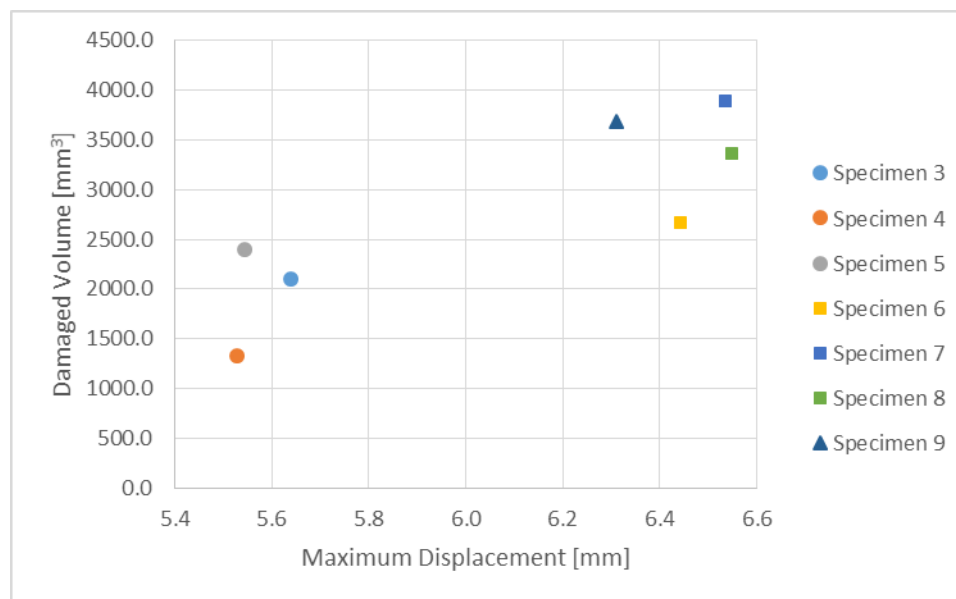


Figure 4.42: Damaged Volume versus Maximum Displacement for All Specimens

After trimming the specimen to only include the central damaged region and performing imaging analysis, slightly different results were obtained as seen in Table 4.3. Note that, while the results presented in Table 4.3 include the damage induced from the cutting process, the conclusions presented in this section still hold. Conclusions developed that account for the induced damage are presented in a later section. While the relative magnitudes of the damaged volume for the cut specimens was roughly the same as for the full-sized plates, the total damaged volume was found to be smaller when analyzing the trimmed plates. This can likely be attributed to a reduction in noise from the increased imaging resolution. Noise is still present in the images for the smaller specimen, but the amount of noise was greatly reduced relative to the amount of damage

present. While the percent damaged volume did not change significantly in relative magnitude, the analysis on the cut specimens did result in smaller percent damaged volume measurements. This would be expected for a decrease in measured damaged volume. The graphical relation between damaged volume and impact energy, maximum impact force, and maximum displacement measured for the cut specimens can be seen in Figure 4.43, Figure 4.44, and Figure 4.45, respectively. To directly compare the change in measured damage volume to the impact energy, maximum impact force, and maximum displacement, the sets of data from both the original and cut specimens were plotted in Figure 4.46, Figure 4.47, and Figure 4.48. The relative shape of the plots is similar to the full-sized specimens for specimens 3 through 8. The most significant change in measured damage occurred for specimen 9, as is reflected in these figures.

Table 4.3: Cut Specimen Damage Measurements

Specimen	Resolution [mm/px]	Max Damage Length [mm]	Depth of Max Damage Length (Adjusted) [mm]	Max Damage Area [mm <sup>2</sup> ]	Depth of Max Damage Area (Adjusted) [mm]	Total Damaged Volume [mm <sup>3</sup> ]	% Damaged Volume
3	0.0588	28.85	3.43	132.51	1.80	868.5	0.149
4	0.0588	28.28	3.54	174.96	2.29	533.8	0.087
5	0.0588	29.54	3.63	289.31	3.02	1057.3	0.206
6	0.0588	39.16	3.23	357.74	1.76	945.8	0.180
7	0.0588	37.06	2.85	494.52	3.01	1213.5	0.227
8	0.0588	32.65	3.49	419.42	3.57	1394.9	0.250
9	0.0588	N/A	N/A	94.81	3.59	521.2	0.079
10	0.0588	N/A	N/A	N/A	N/A	N/A	N/A
11	0.0588	N/A	N/A	89.85	3.36	411.0	0.064

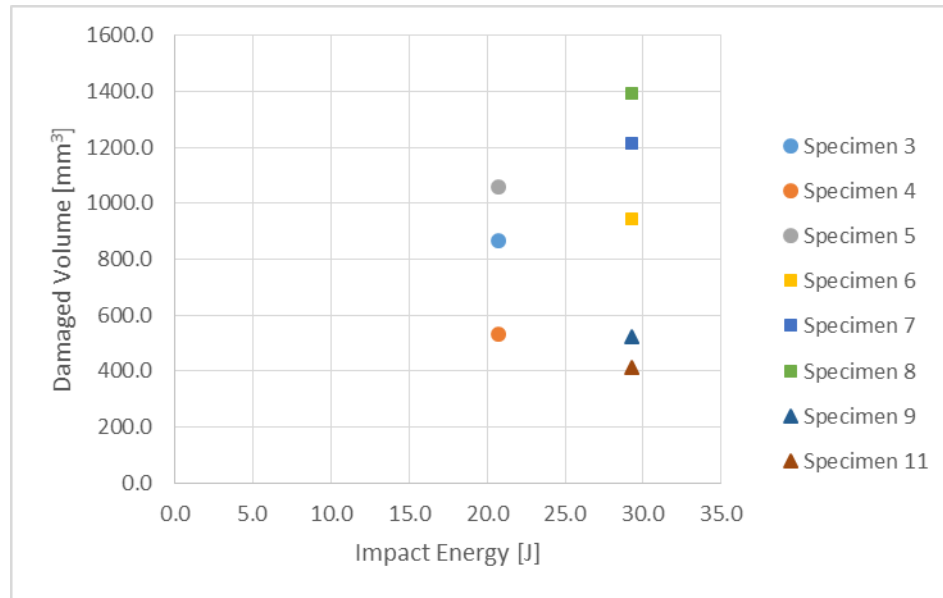


Figure 4.43: Damaged Volume versus Impact Energy for Cut Specimens

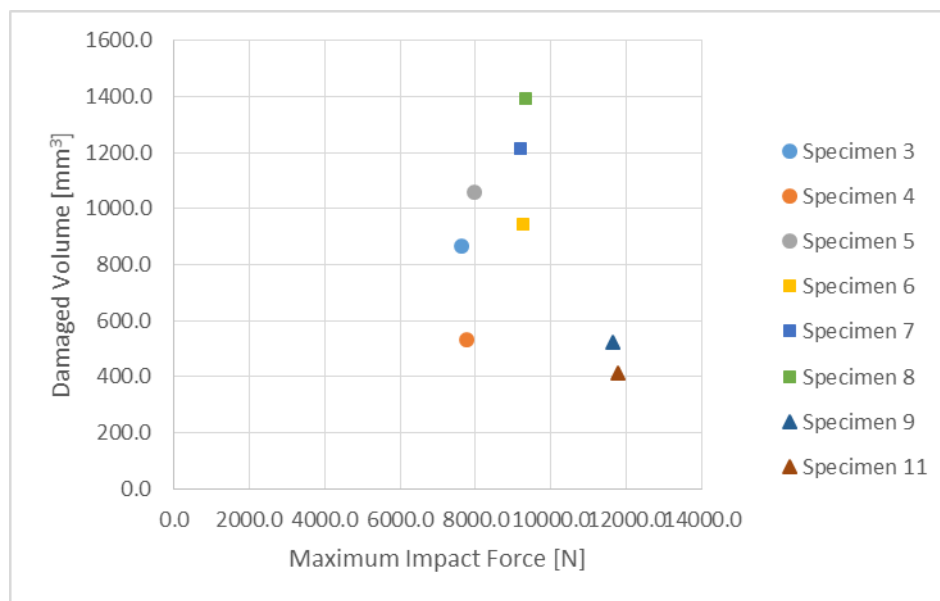


Figure 4.44: Damaged Volume versus Maximum Impact Force for Cut Specimens

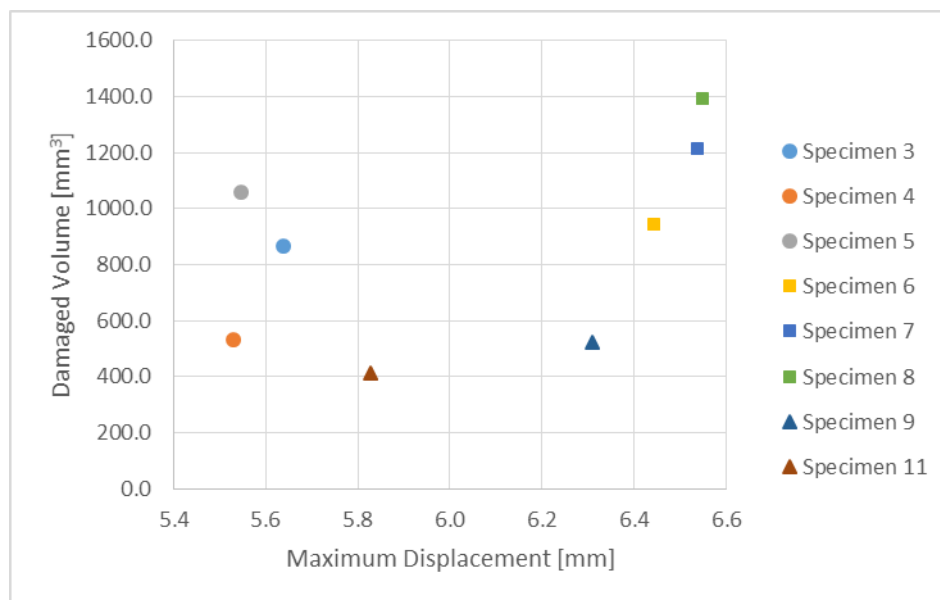


Figure 4.45: Damaged Volume versus Maximum Displacement for Cut Specimens

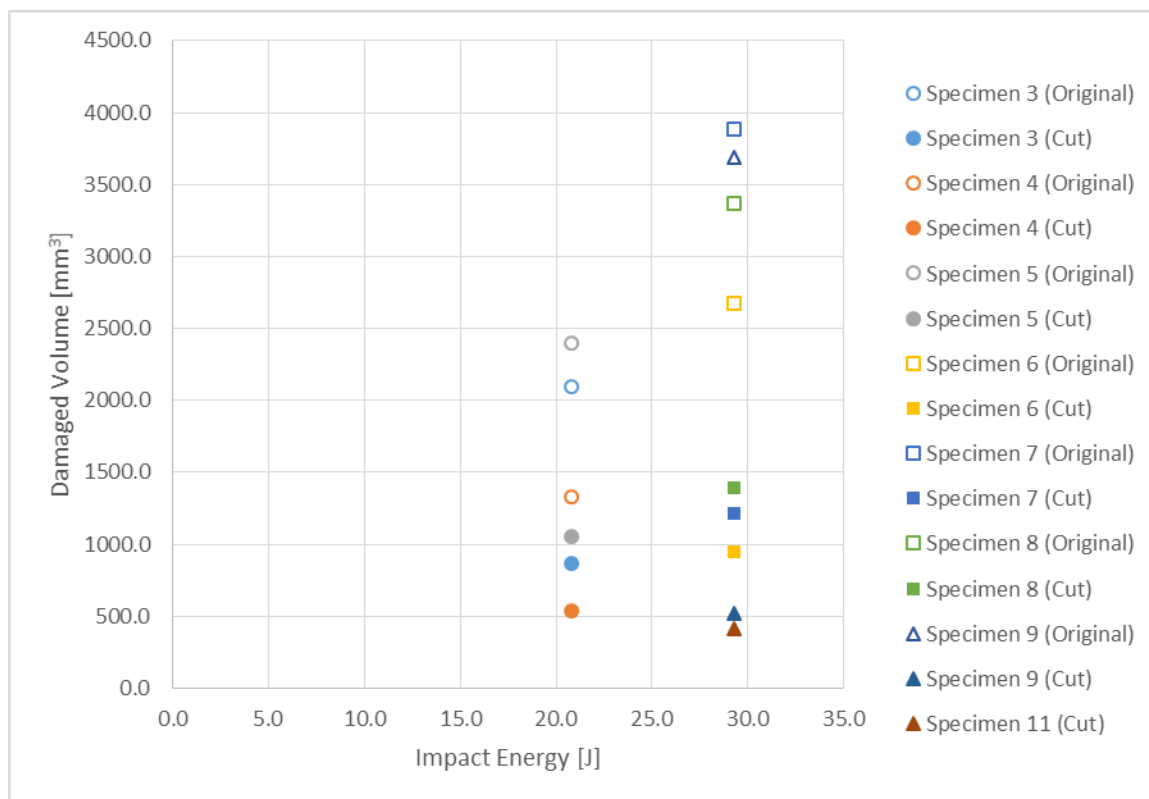


Figure 4.46: Damaged Volume versus Impact Energy for Both Sets of Specimens

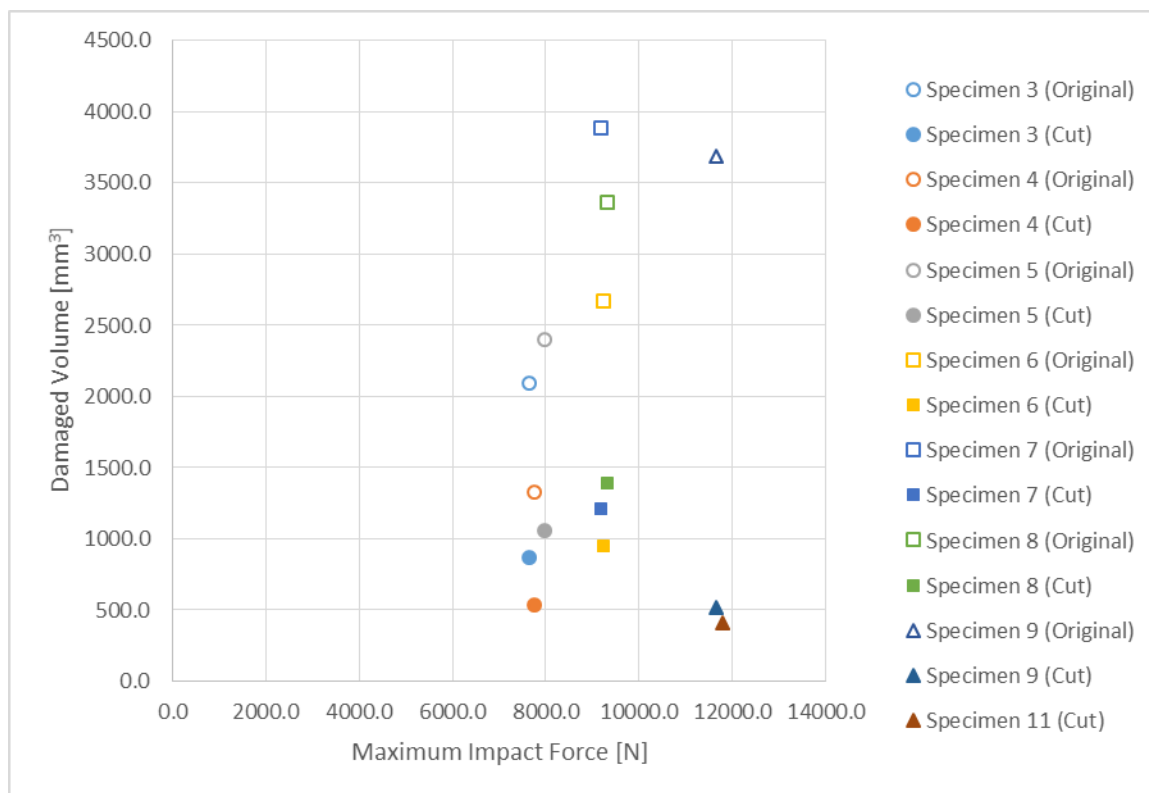


Figure 4.47: Damaged Volume versus Maximum Impact Force for Both Sets of Specimens

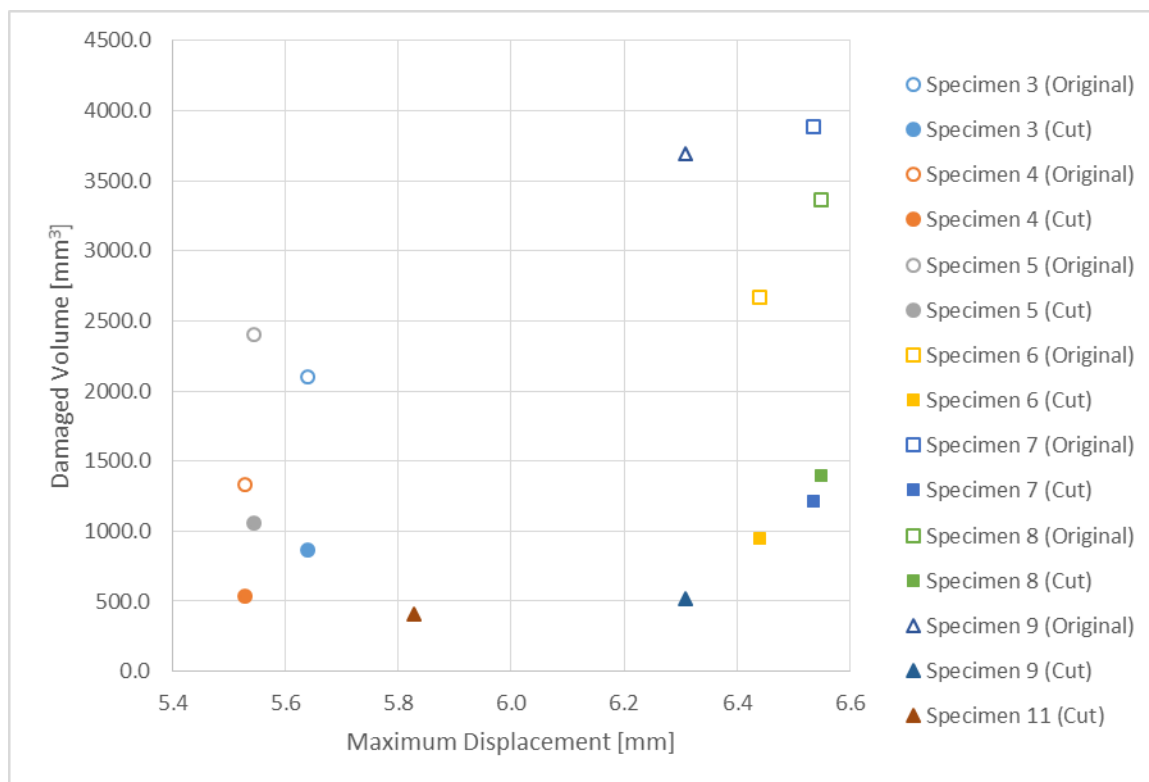


Figure 4.48: Damaged Volume versus Maximum Displacement for Both Sets of Specimens

The relative magnitude of internal damage remained unchanged for specimens 3, 4, and 5 despite changing in value between the original and cut plate analysis. In contrast, specimens 7 and 8 changed in rank of which had more damage, with specimen 7 having more measured damage from the original CT scan and specimen 8 indicating more damage on the cut specimen. Specimen 6 remained stable, with less indicated damage as compared to specimens 7 and 8. Specimen 9 significantly shifted in relative magnitude, whereas it originally had the second largest measured damage area but

reported the smallest damaged area from the higher-resolution scan. From the CT scans of the original specimens, the damage ranking (from greatest measured damage volume to least) was: 7, 9, 8, 6, 5, 3, 4. From the CT scans of the cut specimens, the damage ranking was: 8, 7, 5, 6, 3, 4, 9, 11. While the overall relative damage ranking did not significantly change, specimen 5 did report more damage than specimen 6, which had been impacted at a higher energy.

#### 4.4.2 Comparison to Visual Inspection

Comparing the internal measurements to a visual inspection of the specimens, no meaningful relationship is readily apparent. Table 4.4 lists measurements of damage on the front and back surface of each specimen as well as the internal damaged volume. From those measurements as well as the visual characteristics of the damage, the visual damage ranking was: 8, 7, 6, 3, 4, 5, (9, 10, 11). While the general ranking of some of the specimens remained consistent, such as specimens 7 and 8 ranking highest for visual and internal damage, the damage rank for the specimens impacted at lower energies (3, 4, and 5) were reversed. The visual inspection seemed to indicate that specimen 5 clearly had the least damage of the three, but both CT analyses agreed that specimen 5 had greater damage than either specimens 3 or 4. This supports the conclusion that visual inspection is not sufficient for determination of damage from impact in laminated composites, and that an internal damage assessment is necessary.

Table 4.4: Visual Damage and Internal Damage Measurements

Specimen	Maximum Front 0° Direction Damage [mm]	Maximum Front 90° Direction Damage [mm]	Maximum Back 0° Direction Damage [mm]	Maximum Back 90° Direction Damage [mm]	Damaged Volume (Original) [mm <sup>3</sup> ]	Damaged Volume (Cut) [mm <sup>3</sup> ]
3	25	26	27	6	2097.0	868.5
4	16	28	22	3	1331.5	539.2
5	8	24	19	4	2401.8	1141.1
6	34	35	46	4	2671.3	1002.7
7	31	33	47	3	3889.0	1282.7
8	35	44	47	4	3368.8	1515.5
9	N/A	N/A	N/A	N/A	3690.0	521.2
10	N/A	N/A	N/A	N/A	N/A	N/A
11	N/A	N/A	N/A	N/A	N/A	422.2

#### 4.4.3 Delamination from Specimen Cutting

For all of the cut specimens, the water-jet cutting process induced damage on one corner due to the cutting toolpath and stresses. This delamination can be seen at the right side of Figure 4.49, which shows cut specimen 3. The start of each cut occurred with a lead of approximately 1 mm from the corner of the cut central region, proceeded around the edge of the square, and ended approximately 2 mm away from the first/final corner. On the side opposite the start, a small tab (approximately 1 mm long and 1 mm wide) was cut so that the small plate segment would not fall into the water-jet reservoir. The water-jet did start and stop around the tab, but delamination on this region was significantly less than around the initial corner. This can likely be attributed to free-edge delamination.

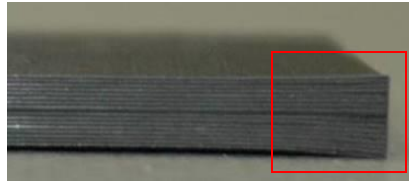


Figure 4.49: Side View of Corner Delamination for Cut Specimen 3

Free edge delamination is a failure mechanism characteristic to laminated composites and is a product of interlaminar normal and interlaminar shear stresses near free edges (Jones 1999). When loading a laminated composite plate near the edge, force and moment equilibrium effects generate large tensile stresses along the edge of the material. These tensile stresses, which are normal to the plane of the reinforcing fibers and act over a relatively small area, place loads on the matrix and can cause matrix cracks in the plane of the plate. As with an impact on the face of the plate, the matrix cracks tend to spread along interfaces between plies of different orientations. Along the free edge, this leads to visible edge delamination.

Thus, an explanation for the increased damage around the corner versus the tabs can be developed. On the start of the cut, some localized damage was induced from the water-jet piercing the plate. Then, as the water-jet moved to complete the cut and approached the newly-created free edge, the stresses caused by cutting led to the development of high tensile stresses along the free edge. These stresses caused matrix

cracking and edge delamination. Since there was only one cutting pass near the tabs, less delamination was developed on the newly-cut free edges in that region.

To analyze the effect that this cutting-induced damage had on the damaged volume results, the corner delamination was isolated for each CT image and measured. These measurements were then totaled and removed from the total damaged volume for each specimen, and these results can be seen in Table 4.5. From isolating the cutting damage, the total damaged volume was reduced by 10.8 to 20.0 % from the initial measurements on the cut specimens. As nearly one fifth of the damaged volume can be attributed to the cutting process, this indicates that processing damage cannot be neglected in damage measurements. Cutting-induced damage analysis was not performed for specimens 9, 10, and 11 as all measured damage on these cut specimens was nominally from corner delamination and noise, with no meaningful impact damage to isolate.

Table 4.5: Cutting-Induced Damage Measurement Results

Specimen	Damaged Volume (Original) [mm <sup>3</sup> ]	Damaged Volume (Cut) [mm <sup>3</sup> ]	% Damaged Volume (Cut)	Cutting-Induced Damage Volume [mm <sup>3</sup> ]	Adjusted Total Damage Volume [mm <sup>3</sup> ]	Adjusted % Damage Volume	% Reduction in Damaged Volume
3	2097.0	868.5	0.1489	93.4	775.2	0.1329	10.8
4	1331.5	539.2	0.0867	96.2	443.0	0.0712	17.8
5	2401.8	1141.1	0.2062	201.7	939.4	0.1697	17.7
6	2671.3	1002.7	0.1797	200.5	802.2	0.1438	20.0
7	3889.0	1282.7	0.2271	191.1	1091.6	0.1933	14.9
8	3368.8	1515.5	0.2500	218.9	1296.6	0.2139	14.4

From the tabulated results it can be seen that, while the percent reduction in damaged volume was up to 20.0 percent, the relative amount of damage for each specimen remained consistent. All of the specimens experienced a decrease in damaged volume, and the ranking of adjusted damaged volume is the same as for the cut specimen damaged volume (from high to low, specimens 8, 7, 5, 6, 3, 4). While the overall damage ranking did not change, ranking the specimens by cutting damage does yield different results. From high to low, the rank for cutting-induced damage is specimens 8, 5, 6, 7, 4, and 3. Of particular note is that specimens 5, 6, 7, and 8 all had similar corner damage volumes, while specimens 3 and 4 had less than half of that damage volume. This is generally consistent with the impact damage results, where specimens 3 and 4 developed less damage than specimens 5 through 8.

#### 4.5 Comparison to Previous Work

The current investigation sought to expand on the CT imaging methods initially developed by Song (2014). In his investigation, the carbon fiber composite specimens examined were 6 inch by 6 inch (152.4 mm by 152.4 mm) layered five harness satin textile composites, with a symmetric orientation of layers in  $0^\circ$ ,  $90^\circ$ ,  $45^\circ$ , and  $-45^\circ$  directions. These specimens were impacted at energies of approximately 16 J, 22.5 J, and 26 J using the hemispherical tool steel tup insert. These impacts produced barely visible to significant amounts of visible damage. As a representative from each energy level, specimen 2-1, shown in Figure 4.50, had been impacted at 16 J, specimen 1-6, shown in

Figure 4.51, had been impacted at 22.5 J, and specimen 2-4, shown in Figure 4.52, had been impacted at 26 J. These specimens were later cut to 35 mm by 35 mm square specimens to isolate the damaged region and allow for more detailed imaging.

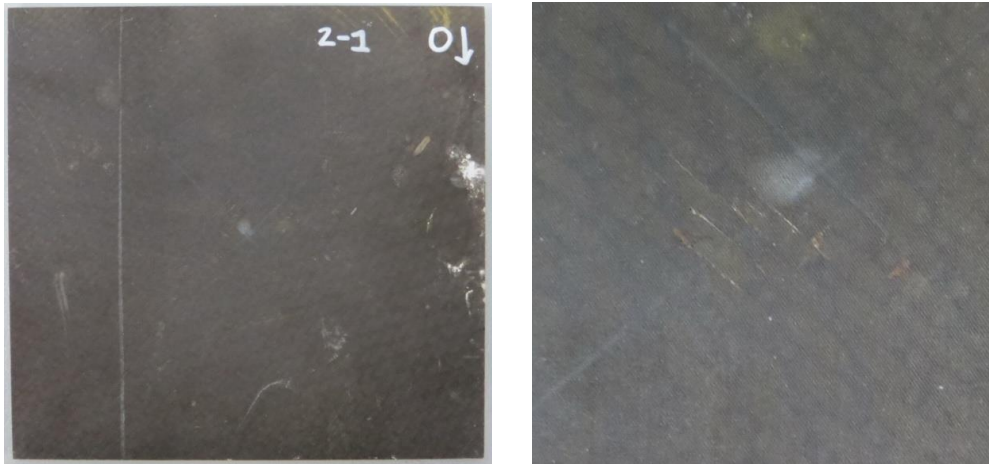


Figure 4.50: Front (Left) and Back (Right) Damage to Specimen 2-1, Impacted at 16 J (Song 2014)

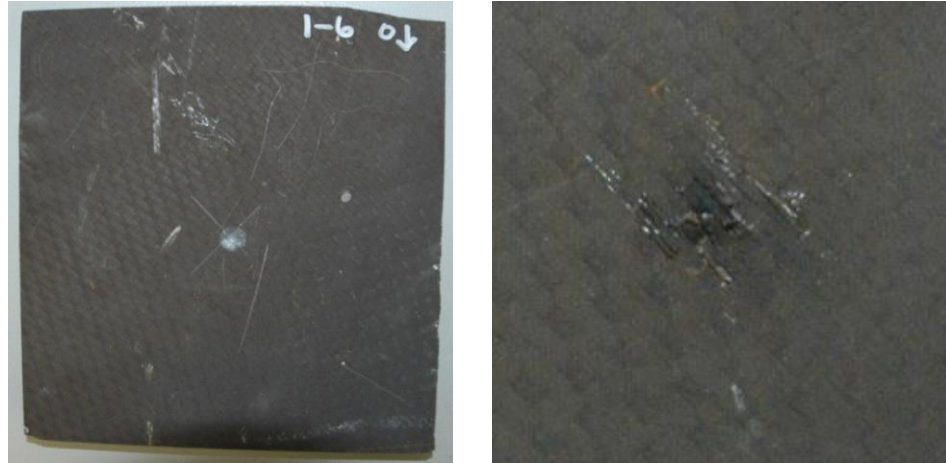


Figure 4.51: Front (Left) and Back (Right) Damage to Specimen 1-6, Impacted at 22.5 J (Song 2014)

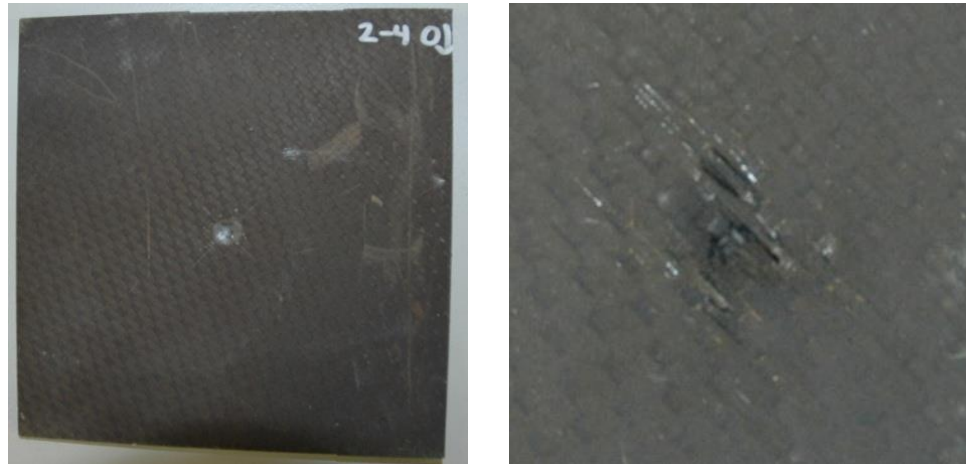


Figure 4.52: Front (Left) and Back (Right) Damage to Specimen 2-4, Impacted at 26 J (Song 2014)

After impact testing, Song performed CT image processing using the same Zeiss METROTOM 1500 CT scanner and MyVGL 2.2 CT imaging software used in the current investigation and described in previous sections. Only the full-sized plates were subjected to a detailed imaging analysis, as the cut specimens were imaged using a different CT system. The resolution for the CT scans of the full plates was 0.2132 mm/px, which was not fine enough to capture the individual layers. To isolate damage, Song used a thresholding method similar to the one used in the current investigation. However, instead of isolating and marking grey-values on both sides of the damaged band as undamaged, Song used a one-sided threshold. Essentially, this placed the “air/support material” region next to the region coded for damage. This produced blue and yellow colorized CT images similar to the ones produced in the current investigation. It is unclear how Song then proceeded to measure the damaged volume, as no suitable tool was found in MyVGL 2.2 and details of this procedure were not provided.

To compare the method used by Song to the current method, the results obtained by Song were investigated. From Song’s analysis of specimen 1-6, he concluded that the maximum damage length was 36.8 mm and occurred at a depth of 2.22 mm, and that the total damaged volume was 84.52 mm<sup>3</sup>. The largest damaged length measured by Song can be seen in Figure 4.53, where the black arrow indicates the direction of the 0° fiber orientation.

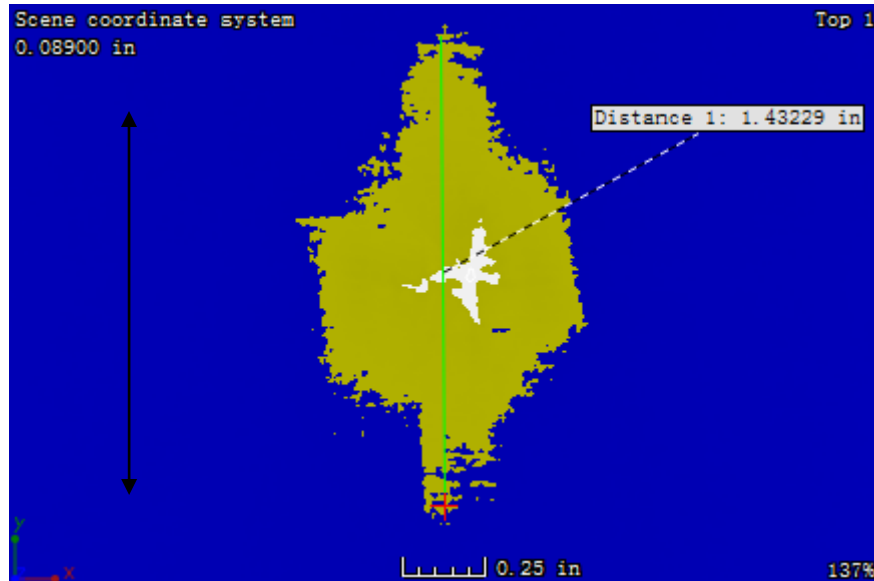


Figure 4.53: Length of Largest Internal Damage Measured by Song for Specimen 1-6 (Depth of 2.22 mm) (Song 2014)

To numerically compare the two methods, full-sized specimen 1-6 was re-processed using the current method. The resolution of the scan was 0.2132 mm/px, and processing produced a stack of 36 images through the thickness of the plate. The image stack had a relative thickness of 7.25 mm and the plate had a measured depth of 4.77 mm. The total damaged volume measured for specimen 1-6 was 5040.0 mm<sup>3</sup>. The maximum damaged length was found to be 39.88 mm at a depth of 2.64 mm (relative depth of 2.56 mm). This damage was oriented in the 0° direction, and is shown in Figure 4.54. Note that, due to the orientation of the CT scan, the 0° direction is in the vertical direction as indicated by the black arrow. The damaged region is boxed in the figure.

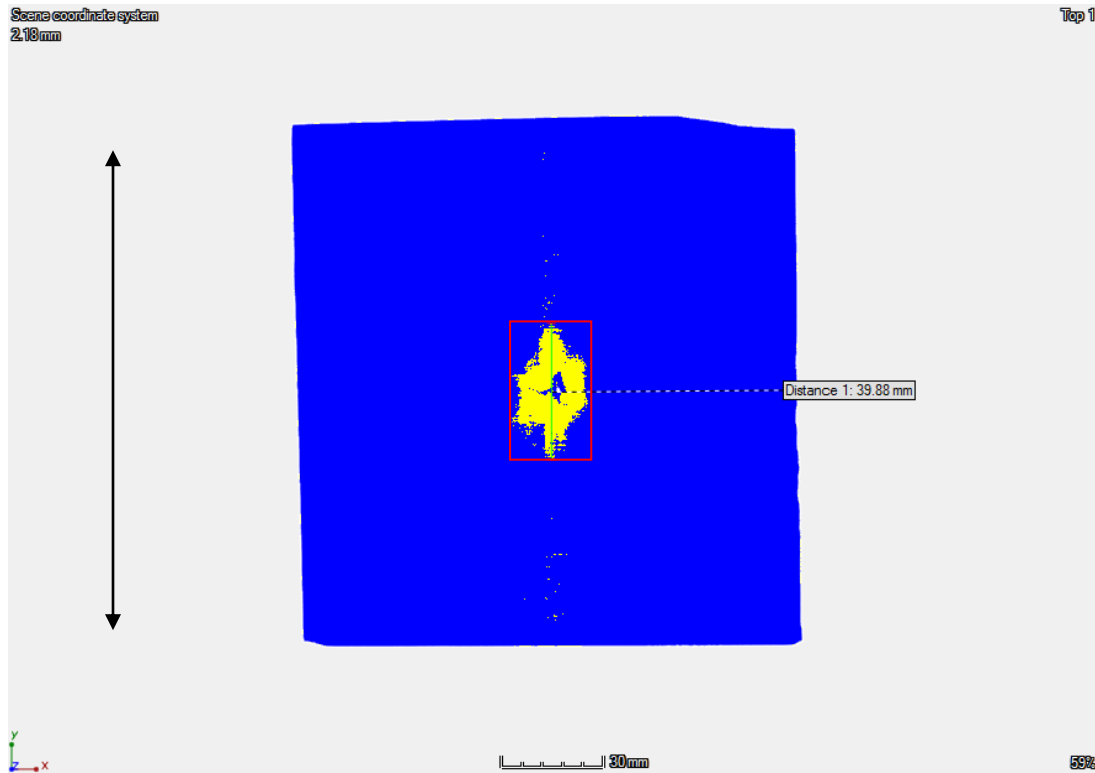


Figure 4.54: Length of Largest Internal Damage for Specimen 1-6 (Depth of 2.64 mm)

Song's measured damage length was slightly shorter than the one measured using the current method and at a shallower depth. The difference in length can be attributed to slight differences in grey-value thresholds, as the damaged area is sensitive to small changes in the threshold bounds. While the lengths were not the same, the general shape of the damaged area was. This would support the conclusion that the two methods are capturing the same damage, even if the exact size is different. The difference in depth

likely comes from the measurement points selected. All measurements of depth are relative to the top surface of the plate, and for this CT scan the plate had a small angle of inclination relative to the plane of the scan. Where the measurements of depth are made can alter the value of the measurement, depending on if the depth is measured near or far from the center. The current method measures depth from the top of the plate near the center but outside of the deformed zone. If Song used points in the deformed zone to measure depth, then that measurement would underestimate the true depth.

The analysis on full-sized specimen 1-6 resulted in a large difference in measured damaged volumes between the two methods used. Since the damaged volumes were orders of magnitude in difference (84.52 mm<sup>3</sup> from Song compared to 5040.0 mm<sup>3</sup> from the current method), a rough magnitude check was performed to determine how reasonable the measurements were. The back surface of specimen 1-6 has visible damage over a circular region with a diameter of approximately 10 mm. If the internal damaged region was limited to a cylinder of this diameter extending through the entire plate (thickness of 4.61 mm), the damaged volume would be 362.1 mm<sup>3</sup>. Since Song provided measurements of damaged length throughout the thickness of the plate, a more accurate estimate can be made. The damaged area can be modeled as an ellipse with the length of the major axis the maximum length of the damaged area and the length of the minor axis half of that length. Multiplying each image by the resolution to obtain damaged volumes, this estimate predicts a total damaged volume of 501.3 mm<sup>3</sup>. While details of Song's measurement techniques were not available, the colorized CT images used by Song were available. Processing the 16 images of the damaged region of specimen 1-6 using the MATLAB program from the current method resulted in a

damaged volume of 663.2 mm<sup>3</sup>. These estimates fall between the volumes measured by Song and the current method, and they provide a lower-end bound for the expected damaged volume. The estimates indicate that Song's measurements were far too low, and that the current method likely overestimates the damaged volume for the full-sized plates.

To obtain a more detailed analysis of the internal damage, cut specimens 2-1, 1-6, and 2-4 were processed using MyVGL and the current method. The resolution of the scans of the cut specimens was 0.0482 mm/px, and the results of image processing can be found in Table 4.6. Due to the large angle of inclination of the plates relative to the plane of the scan, no meaningful measurements of damage length could be obtained. Since no previous damaged volume analysis had been performed on the cut specimens, no quantitative comparison to Song's method can be made. However, the results of the cut specimens can be compared to Song's analysis of the full-sized plates. As can be seen from the table, there is a significant discrepancy between the results obtained by Song and the results from the current investigation. The damaged volumes are orders of magnitude different, and the measurements from the full plates are less than those of the cut plates. This result is the opposite of the trend seen in the current investigation. However, when considering the measurements taken with the current method on specimen 1-6, the expected trend was seen; the analysis of the full-sized plate produced a resulting damaged volume greater than that of the cut plate. This result can be attributed to noise from the thresholding process, which was reduced on the cut plate. While the results of cut specimen 1-6 were still significantly larger than Song's results, it was much closer in value to the rough estimates of the damaged volume (estimates of 362.1 to 663.2

mm<sup>3</sup> compared to the measurement of 1040.2 mm<sup>3</sup>). This supports the conclusion that the current method likely has improved measurement accuracy compared to the method used by Song.

Table 4.6: CT Imaging Results of Song's Specimen

Specimen	Damaged Volume for Full Plate [mm <sup>3</sup> ] (Song 2014)	Damaged Volume [mm <sup>3</sup> ] (Demerath 2015)	% Damaged Volume
1-6 (Original)	84.52	5040.0	1.0405
1-6 (Cut)	84.52	1040.2	0.9490
2-1 (Cut)	4.38	1084.9	N/A
2-4 (Cut)	101.09	1281.0	N/A

The discrepancy between the results of Song's work and the current investigation highlights the need for a consistent image processing method. Without the specific details of how key parameters were measured, results cannot be replicated or verified. Some of the difference in results can be attributed to the grey-value threshold used, as the one-sided threshold employed by Song could have discarded some of the damaged volume captured by the two-sided threshold of the current method. This does not account of the entire difference in damaged volume measurements, but it does indicate that these measurements are sensitive to the methods used.

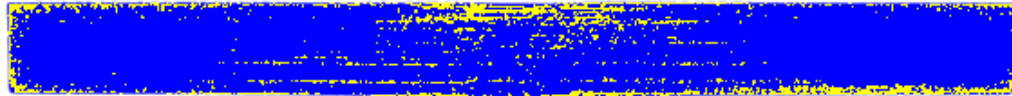
#### 4.6 Summary of Image Processing

Overall, CT imaging was found to be an effective method of measuring the internal damage in laminated carbon fiber reinforced polymer composite plates. A visual inspection only revealed external damage, and CT imaging of the full-sized plates provided a decent first estimate for the relative amount of internal damage. CT imaging of the cut specimens was also performed, providing a better measurement of the damaged volume.

When compared to the full-sized specimen, imaging on the small plates had certain advantages. Because the resolution was higher than the thickness of the individual plies, damage between plies could be more easily identified. The ply orientation for most images could be identified, and the orientation of ply delamination could be distinguished. That allowed for the overall shape of the internal damage to be identified, as seen in Figure 4.55. From the impacted surface (top of plate in this figure), a cone-shaped damage pattern can be seen, matching the expected damage pattern for thick laminates (Abrate 1998).

Scene coordinate system  
1.78mm

Front 1



5mm

73%

Figure 4.55: Side View of the Center of Cut Specimen 3

While the smaller specimens did provide some new insight into the internal damage, image processing on these CT scans did present some challenges. As can be seen in most all of the internal segments, one of the corners has significant damage. This delamination was a product of the water-jet cutting of the specimen, and the introduced damage required additional processing to be isolated from the damaged volume measurements. Another challenge was thresholding of the images. The grey-value band that would isolate damage without introducing significant noise was much more sensitive

on the small plates. While more damage was able to be identified appropriately, filtering noise on either side was much more difficult.

In addition to the challenges posed by the smaller specimen, it was shown that the CT imaging results were very dependent on the image processing methods used. Results from a previous investigation were compared to the results of the same CT scan using the current method. Even on reduced specimen sizes, the current method measured significantly more damage. While the discrepancies can be mainly attributed to thresholding techniques and area measurement procedures, this illustrates the need for consistency in CT image processing methods.

## CHAPTER 5

### SUMMARY AND RECOMMENDATIONS

#### 5.1 Summary

In this work, 32-ply symmetric cross-ply IM7/977-3 composite plates were subject to low-velocity impact, CT imaged, analyzed, cut, and reimaged. This initially involved determining the impact parameters to produce barely and slightly visible damage on the surfaces of the plates. As this investigation utilized a different tup insert than previous investigations, the differences in contact stresses were considered between a flat-ended DELRIN® cylinder and a tool steel hemispherical impactor. From that analysis, it was determined that the flat-ended cylinder would produce lower contact stresses, and therefore produce less damage for a given impact energy.

After performing low-velocity impact tests, the nine impacted specimen were CT imaged using a Ziess METROTOM 1500 industrial CT scanning system. Due to the relatively large size of the specimens, the resolution of the images was too low to identify damage at each individual ply interface. Despite this, the initial imaging allowed for identification of the general damaged area and provided some insight into the relation between impact energy and internal damaged volume.

To increase the accuracy and utility of the CT images, the specimens were cut to a smaller size. The reduced plates encapsulated the damaged area, but developed some damage from the cutting process. The small plates were scanned using the same process as the original plates, and the resolution was found to be fine enough to capture the

individual ply interfaces. Using the higher-resolution images, the damaged volume was again calculated. From these results, it was found that damaged volume generally increased with increasing impact energy, deflection, and maximum impact force. However, the relationship was not strong despite the difference in impact energies.

Overall, the present investigation successfully explored, analyzed, and developed improvements for laboratory procedures for conducting CT imaging analysis of impact damage in laminated composites. Specifically, the current method allowed for measurements on specimens of reduced size, which were not obtainable in previous cut-specimen imaging. Additionally, on smaller specimens damage along the ply interfaces was able to be isolated, providing key details of damage previously not available.

Throughout the present investigation several issues occurred, mostly relating to specimen imaging and cutting. These issues, and recommendations for improving the deficiencies, are discussed in the following section.

## 5.2 Recommendations

The first recommendation for improving the methods discussed in this investigation involves the imaging of specimens. In the previous work by Song (2014), the CT images produced from the Ziess MTEROTOM 1500 were at various orientations relative to each other. While the present investigation was able to ensure that the specimens were all scanned in the same orientation, there was an issue with plate inclination. When placed in the holding fixture within the CT scanning system, it was possible for the plates to be at a slight angle to the imaging plane. This resulted in a gradient forming across the surface of the specimens as well as ply interfaces not lying

along single images. While this may be difficult to improve, since the inclination resulted from a difference of a few millimeters across the plate, careful placement of the specimens is necessary to produce useful images. CT technicians should be made aware of the importance of specimen alignment, and researchers should work with them to ensure proper setup.

Along with the previous recommendation, researchers should work with the CT analyst to make sure that the output files are in a useful format. Progress was temporarily delayed in the current investigation because of files not being saved in the proper format. As discussed in a previous chapter, in order to use MyVGL 2.2 to view and analyze specimens it was necessary to first save the files as a project using VGStudio MAX.

Another recommendation for image processing is to develop a more consistent method for setting grey-values when thresholding the damaged regions. The current process involves manually identifying damage in the black and white images and then setting the grey-value bounds to isolate that damage. This was necessary because the grey-value distribution varied from specimen to specimen. If more consistent CT imaging was achieved, it might be possible to develop numeric grey-value criteria for isolating damage. This would ensure repeatable damage measurements across different specimens.

A final recommendation for image analysis is to improve area measurement automation. The MATLAB code developed for measuring damaged area is effective, but not very efficient. Specifically, due to the way colors are segment the regions do not always correspond to the same colors. While this is not a problem for processing individual images, it does require additional effort to process the output from multiple

images. A better method of segmentation or value sorting criteria would decrease the need to rerun images for color region verification.

Finally, specimen cutting could be improved. When cutting specimens using the water-jet, care must be taken to ensure that additional damage is not induced. While the water-jet produces excellent surfaces along all cut edges, the initial and final locations of the toolpath can have induced damage. Toolpaths should be set so that the water-jet starts and stops cuts far away from the region of interest. Ideally, the toolpath should start and stop on areas outside the plate. Sandwich-clamping of the plate might also be used to limit the delamination at the cut start/stop locations. Also, the water-jet should be checked to ensure proper “zeroing” of the cutting head before each cut. Because of issues locating the origin of the toolpath, specimen 10 was improperly cut. This issue could have been avoided by verifying the origin of the programmed toolpath. Researchers should be sure to work with the water-jet operators to ensure that the desired results are consistently obtained.

## APPENDIX

### IMAGE PROCESSING MATLAB CODE

In order to measure the damaged area from the colorized images, a MATLAB program was developed. This code was adapted from a standard example available from MathWorks (2014). The adapted code was developed in two forms: One form for processing multiple images at once, and one form for processing single images.

Both programs operated in the same way. Each image would be read in by MATLAB and converted into an array, with pixel colors converted into numbers in the array. The image would then be segmented according to color, with a total of three segmentation regions. The three segmentations corresponded to the three main colors present in the images. For this investigation, the colors were blue, yellow, and white. After thresholding, a new image array would contain simply black, grey, and light grey according to the threshold value. A “region” array would also be produced which contained the segment label number (1, 2, or 3), which corresponded to one of the three segmented colors. The values in this array were counted and then reported to the user. Since the images were at a 100 % scale, the pixels corresponded to the original voxels from the CT scan. This allowed the count of each segmented region to correspond to a measurement of area on the original scan.

Because of the number of images produced at higher resolutions, the automated multi-image script was initially employed. This scrip would read in all of the images stored in a specific folder (in this case, the folder was located at

\\engin.uiowa.edu\stuff\Home\bdemerath\Documents\MATLAB\Images\, but could be reassigned as necessary). The output would be an array with the pixel counts for the blue, yellow, and white regions from each image. This process was faster than running each image individually.

Despite the efficiency of the multi-image code, it did have a major drawback. Because all images were processed at the same time, no thresholding images were displayed to the user. Because of the thresholding method, the region labels 1, 2, and 3 were not consistently applied to specific colors in the images. For instance, in one image the labels might indicate yellow as 1, blue as 2, and white as 3 while in another image they might indicate white as 1, blue as 2, and yellow as 3. This meant that images needed to be checked to verify which count corresponded to which color. For images in the middle of the CT stack this was fairly obvious, since the number of blue, white, and yellow pixels were consistent in relative magnitude. For images near the front and back surfaces, however, individual processing was necessary to ensure accuracy in the color label count.

### A.1 Multi-Image Segmentation Code

```
close ALL
clear
clc

iStart=1;
iEnd=92; %CHANGE AS NEEDED; Total number of images to be processed

iFiles=iEnd-iStart+1;
pxData=zeros(iFiles,4);

for n=iStart:iEnd
```

```

n
% Step 1: Read Image

file_name=dir(strcat('\\engin.uiowa.edu\stuff\Home\bdemerath\Documents\
MATLAB\Images\')); % Filepath to folder with images
he=imread(strcat('\\engin.uiowa.edu\stuff\Home\bdemerath\Documents\MATL
AB\Images\'',file_name(n+2).name)); % Accounts for hidden files from
MatLab's folder structure
%he = imread(filename);
% figure, imshow(he), title('Original Image');
%%

% Step 2: Convert Image from RGB Color Space to L*a*b* Color Space

cform = makecform('srgb2lab');
lab_he = applycform(he,cform);

% Step 3: Classify the Colors in 'a*b*' Space Using K-Means Clustering

ab = double(lab_he(:,:,2:3));
nrows = size(ab,1);
ncols = size(ab,2);
ab = reshape(ab,nrows*ncols,2);

nColors = 3;
% repeat the clustering 3 times to avoid local minima
[cluster_idx, cluster_center] =
kmeans(ab,nColors,'distance','sqEuclidean',...
        'Replicates',3);

% Step 4: Label Every Pixel in the Image Using the Results from KMEANS

pixel_labels = reshape(cluster_idx,nrows,ncols);
% figure, imshow(pixel_labels,[]), title('image labeled by cluster
index');

% Step 5: Create Images that Segment the Image by Color.

segmented_images = cell(1,3);
rgb_label = repmat(pixel_labels,[1 1 3]);

for k = 1:nColors
    color = he;
    color(rgb_label ~= k) = 0;
    segmented_images{k} = color;
end

% figure, imshow(segmented_images{1}), title('objects in cluster 1');
% figure, imshow(segmented_images{2}), title('objects in cluster 2');

```

```

% figure, imshow(segmented_images{3}), title('objects in cluster 3');

Area1 = 0;
Area2 = 0;
Area3 = 0;
TotalCount = 0;

for i = 1:nrows
    for j = 1:ncols
        if pixel_labels(i,j) == 1
            Area1 = Area1 + 1;
        end
        if pixel_labels(i,j) == 2
            Area2 = Area2 + 1;
        end
        if pixel_labels(i,j) == 3
            Area3 = Area3 + 1;
        end
        TotalCount = TotalCount + 1;
    end
end
pxData(n,1) = n-1;
% Output the three regions as a percent of the figure and pixel count
% Percentage_total_area_Group_1 = (Area1/TotalCount)*100
pxData(n,2) = Area1;

% Percentage_total_area_Group_2 = (Area2/TotalCount)*100
pxData(n,3) = Area2;

% Percentage_total_area_Group_3 = (Area3/TotalCount)*100
pxData(n,4) = Area3;
end
pxData

```

## A.2 Single-Image Segmentation Code

```

close ALL
clear
clc

%% Step 1: Read Image

filename = uigetfile;
he = imread(filename);
figure, imshow(he), title('Original Image');

```

```

%% Step 2: Convert Image from RGB Color Space to L*a*b* Color Space
% Convert the image to L*a*b* color space using |makecform| and
|applycform|.

cform = makecform('srgb2lab');
lab_he = applycform(he,cform);

%% Step 3: Classify the Colors in 'a*b*' Space Using K-Means Clustering
% Since the color information exists in the 'a*b*' space, your objects
are
% pixels with 'a*' and 'b*' values. Use |kmeans| to cluster the
objects into
% three clusters using the Euclidean distance metric.

ab = double(lab_he(:,:,2:3));
nrows = size(ab,1);
ncols = size(ab,2);
ab = reshape(ab,nrows*ncols,2);

nColors = 3;
% repeat the clustering 3 times to avoid local minima
[cluster_idx, cluster_center] =
kmeans(ab,nColors,'distance','sqEuclidean',...
        'Replicates',3);

%% Step 4: Label Every Pixel in the Image Using the Results from KMEANS
% For every object in your input, |kmeans| returns an index
corresponding to a
% cluster. The |cluster_center| output from |kmeans| will be used later
in the
% example. Label every pixel in the image with its |cluster_index|.

pixel_labels = reshape(cluster_idx,nrows,ncols);
figure, imshow(pixel_labels,[]), title('image labeled by cluster
index');

%% Step 5: Create Images that Segment the H&E Image by Color.
% Using |pixel_labels|, you can separate objects in |image| by color,
% which will result in three images.

segmented_images = cell(1,3);
rgb_label = repmat(pixel_labels,[1 1 3]);

for k = 1:nColors
    color = he;
    color(rgb_label ~= k) = 0;
    segmented_images{k} = color;
end

```

```

figure, imshow(segmented_images{1}), title('objects in cluster 1');
%%
figure, imshow(segmented_images{2}), title('objects in cluster 2');
%%
figure, imshow(segmented_images{3}), title('objects in cluster 3');
%%

Area1 = 0;
Area2 = 0;
Area3 = 0;
TotalCount = 0;

for i = 1:nrows
    for j = 1:ncols
        if pixel_labels(i,j) == 1
            Area1 = Area1 + 1;
        end
        if pixel_labels(i,j) == 2
            Area2 = Area2 + 1;
        end
        if pixel_labels(i,j) == 3
            Area3 = Area3 + 1;
        end
        TotalCount = TotalCount + 1;
    end
end

% Output the three regions as a percent of the figure and pixel count
Percentage_total_area_Group_1 = (Area1/TotalCount)*100
Area1

Percentage_total_area_Group_2 = (Area2/TotalCount)*100
Area2

Percentage_total_area_Group_3 = (Area3/TotalCount)*100
Area3

```

## REFERENCES

- Abrate, Serge. 1998. *Impact on Composite Structures*. New York: Cambridge University Press.
- Boeing. 2014. "787 Program Fact Sheet." Boeing Accessed 9/4/14.  
<http://www.boeing.com/boeing/commercial/787family/programfacts.page>.
- Bull, D. J., S. M. Spearing, I. Sinclair, and L. Helfen. 2013. "Three-dimensional assessment of low velocity impact damage in particle toughened composite laminates using micro-focus X-ray computed tomography and synchrotron radiation laminography." *Composites Part a-Applied Science and Manufacturing* 52:62-69. doi: 10.1016/j.compositesa.2013.05.003.
- Daggumati, S., I. De Baere, W. Van Paepegem, J. Degrieck, J. Xu, S. V. Lomov, and I. Verpoest. 2010. "Local damage in a 5-harness satin weave composite under static tension: Part I - Experimental analysis." *Composites Science and Technology* 70 (13):1926-1933. doi: 10.1016/j.compscitech.2010.07.003.
- Deierling, Phillip E. 2010. "Electrical and Thermal Behavior of IM7/977-3 Carbon Fiber Polymer Matrix Composites Subjected to Time Varying and Steady Electric Currents." Master of Science, Dept. of Mechanical Engineering, University of Iowa.
- Desplentere, F., S. V. Lomov, D. L. Woerdeman, I. Verpoest, M. Wevers, and A. Bogdanovich. 2005. "Micro-CT characterization of variability in 3D textile architecture." *Composites Science and Technology* 65 (13):1920-1930. doi: 10.1016/j.compscitech.2005.04.008.
- Devivier, C., F. Pierron, and M. R. Wisnom. 2013. "Impact damage detection in composite plates using deflectometry and the Virtual Fields Method." *Composites Part a-Applied Science and Manufacturing* 48:201-218. doi: 10.1016/j.compositesa.2013.01.011.
- DuPont. DELRIN actel resins: Design Information.
- Gao, S. L., and J. K. Kim. 1998. Three-dimensional characterization of impact damage in CFRPs.
- Hart, Robert J. 2011. "Characterization of Carbon Fiber Polymer Matrix Composites Subjected to Simultaneous Application of Electric Current Pulse and Low Velocity Impact." Master of Science, Dept. of Mechanical Engineering, University of Iowa.

- Hertz, H. 1881. "Ueber die Berührung fester elastischer Körper." *Journal für die Reine und Angewandte Mathematik* 92:156-171.
- Hufenbach, W., R. Bohm, M. Gude, M. Berthel, A. Hornig, S. Rucevskis, and M. Andrich. 2012. "A test device for damage characterisation of composites based on in situ computed tomography." *Composites Science and Technology* 72 (12):1361-1367. doi: 10.1016/j.compscitech.2012.05.007.
- Icten, B. M., B. G. Kiral, and M. E. Deniz. 2013. "Impactor diameter effect on low velocity impact response of woven glass epoxy composite plates." *Composites Part B-Engineering* 50:325-332. doi: 10.1016/j.compositesb.2013.02.024.
- Instron Corporation. 2004. Instron Dynatup Model 8200 Drop Weight Impact Testing Instrument.
- Johnson, K.L. 1985. *Contact Mechanics*. Cambridge: Cambridge University Press.
- Jones, Robert M. 1999. *Mechanics of Composite Materials*. 2nd ed. New York: Taylor & Francis Group.
- Malhotra, A., and F. J. Guild. 2014. "Impact Damage to Composite Laminates: Effect of Impact Location." *Applied Composite Materials* 21 (1):165-177. doi: 10.1007/s10443-013-9382-z.
- MathWorks. 2014. Color-Based Segmentation Using K-Means Clustering.
- Pearson, J. D., M. A. Zikry, M. Prabhugoud, and K. Peters. 2007. "Global-local assessment of low-velocity impact damage in woven composites." *Journal of Composite Materials* 41 (23):2759-2783. doi: 10.1177/0021998307078734.
- Powell, D., T. Zohdi, and D. Johnson. 2008. Impact and Delamination Failure Characterization of BMS 8-212 composite aircraft material. U.S. Department of Transportation, Federal Aviation Administration.
- Sierakowski, R. L., and G. M. Newaz. 1995. *Damage Tolerance in Advanced Composites*. Lancaster, Pennsylvania: Technomic Publishing Company.
- Song, Changpeng. 2014. "Low Velocity Impact Testing and Computed Tomography Damage Evaluation of Layered Textile Composite." Master of Science, Dept. of Mechanical Engineering, University of Iowa.
- Tan, K. T., and N. Watanabe. 2012. "Impact Damage Resistance, Response, and Mechanisms of Laminated Composites Reinforced by Through-Thickness Stitching." *International Journal of Damage Mechanics* 21 (1):51-80. doi: 10.1177/1056789510397070.

- Tan, K. T., N. Watanabe, and Y. Iwahori. 2011. "X-ray radiography and micro-computed tomography examination of damage characteristics in stitched composites subjected to impact loading." *Composites Part B-Engineering* 42 (4):874-884. doi: 10.1016/j.compositesb.2011.01.011.
- Wright, S.C., N.A. Fleck, and W.J. Stronge. 1993. "Ballistic impact of polycarbonate - an experimental investigation." 13 (1):1-20.
- Zantout, Alan E. 2009. "Electrical and Impact Characterization of Carbon Fiber Polymer Matrix Composites." Master of Science, Dept. of Mechanical Engineering, University of Iowa.
- Zeiss. 2015. "METROTOM 1500." Accessed 3/4. [http://www.zeiss.com/industrial-metrology/en\\_us/products/systems/computed-tomography/metrotom-1500.html](http://www.zeiss.com/industrial-metrology/en_us/products/systems/computed-tomography/metrotom-1500.html).